Atmospheric Response to Arctic Sea Ice Loss in a Stratosphere–Troposphere Coupled System

Kazuhira Hoshi

Doctoral Program in Environmental Science and Technology
Graduate School of Science and Technology
Niigata University

Abstract

The northern continents have experienced severe weather and cold winters in the recent decades, and the influence of the Arctic sea ice loss on those has been extensively studied based on observational analyses and numerical simulations. In addition to tropospheric processes, recent studies have shown the important role of the stratosphere in this Arctic–midlatitude climate linkage, in which the upward propagation of planetary-scale waves, eddy–mean flow interaction, downward progression of the polar vortex anomaly, and negative phase shifts of the Arctic Oscillation/North Atlantic Oscillation in the troposphere, collectively referred to as the stratospheric pathway, provide a dynamical link. This thesis aims at better understanding the stratospheric responses to the sea ice loss and roles of the stratosphere on the surface Arctic–midlatitude climate linkage. Reanalysis data and results of atmospheric general circulation model experiments are examined.

First, the detailed features of the upward planetary wave propagation that drives the stratospheric pathway as mean state responses to the sea ice loss are examined with a focus on the poleward eddy heat fluxes. The recent Arctic sea ice loss results in increased poleward eddy heat fluxes in the eastern and central Eurasia regions at the lower stratospheric level. A linear decomposition scheme reveals that this modulation of

the heat fluxes arises from the coupling of the climatological planetary wave field with the temperature anomalies for the eastern Eurasia region and with the meridional wind anomalies for the central Eurasia region. The propagation of quasi-stationary Rossby waves results in a dynamical link between these temperature and meridional wind anomalies with the sea ice loss over the Barents–Kara Sea (BKS). The results provide a detailed three-dimensional picture of the way the recent sea ice loss in the BKS significantly modulates the stratospheric poleward eddy heat flux field and subsequently affects the stratospheric wave structure, which drive the stratosphere–troposphere coupling processes.

In addition to the mean state responses discussed above, we examine characteristics of weak polar vortex (WPV) events modulated by the Arctic sea ice loss. Note that during WPV events a rapid weakening of the polar vortex occurs in a matter of the several days and this event leads to tropospheric circulation anomalies and the midlatitude cooling. Prior to the onset of the WPV events in heavy-ice years, the upward wave propagation is dominated by the wavenumber 1 component. In contrast, the WPV events occurring in the light-ice years are characterized by the stronger wavenumber 2 propagation caused by the tropospheric wavenumber 2 response to the sea ice reduction in the BKS. Those results indicate that, under present climate

conditions, the Arctic sea ice loss is a possible factor modulating the wave propagation during the WPV events. Additionally, the WPV events in the light-ice years are characterized by a stronger stratosphere–troposphere coupling, followed by colder midlatitude surface conditions, particularly over Eurasia. This result suggests that the stronger vertical coupling of the WPV events modulated by the sea ice loss is the additional factor that induces the midlatitude cold anomalies.

The above results indicated the role of the stratospheric pathway on the tropospheric responses to the sea ice loss, with focuses on the mean state and WPV events. In the climate system there are many factors that modulate the stratospheric polar vortex strength, and those may modulate the stratospheric pathway and the tropospheric responses to the Arctic sea ice loss. Here we focus on the influence from the quasi-biennial oscillation (QBO) of the equatorial stratospheric zonal winds. In the easterly QBO, which has a weak polar vortex background condition, a strongly positive and highly significant relation exists between sea ice and Eurasian temperature variations. By contrast, no such relation is found in the westerly QBO with a strong polar vortex background condition. The stratospheric pathway and tropospheric circulation anomalies related to sea ice variability are also seen only in the easterly QBO. Although the mechanisms of the influences of the stratospheric QBO are still

unknown, this knowledge improves our understanding of the Arctic–midlatitude climate linkage.

From the three research topics, this study indicates spatial characteristics of the upward planetary wave propagation that drives the stratospheric pathway, with focuses on the mean state and WPV responses to the sea ice loss. This study also shows the roles of the WPV events modulated by the sea ice loss and the stratospheric QBO influence on the Arctic–midlatitude climate linkages. Thus, this thesis presents the important stratospheric processes that contribute to the Arctic–midlatitude climate linkages.

Abstract (in Japanese)

近年、冬季の地上気温は中緯度域において低下傾向となっており、極端な寒波も増加傾向にある事が報告されている。この一因として、北極域における海氷域面積の減少と、それに伴う北極域の高温化による寄与が議論されている（北極–中緯度リンク）。対流圏における様々なプロセスが議論される中で、成層圏を介したプロセスの存在も明らかになってきた。これは、少氷によって対流圏から成層圏への惑星波の上方伝播が強まる事で極渦の弱化を引き起こし、その弱化シグナルがさらに下方に伝播する事で対流圏では負の Arctic Oscillation (AO)/North Atlantic Oscillation (NAO) 傾向となり、その結果、極からの寒気流出が強まることで中緯度域では低温傾向となる、というプロセスである。本研究では、近年の北極–中緯度リンクにおける成層圏過程の役割とプロセスの詳細について明らかにする事を目的とし、以下 3 つの課題に取り組んだ。その際、再解析データと大気大循環モデルを用いた数値実験の結果を解析した。

第一に、近年の海氷域減少が惑星波上方伝播を強めるプロセスの詳細を調べた。その際、上方伝播の強さを表す物理量である、極向き渦熱フラックス v^*T^*（v：南北風速、T：気温、$(\ \ )^*$：東西平均からの差）に着目した。再解析データを用いてバレンツ・カラ海での海氷域減少に伴う偏差を調べた結果、成層圏過程を引き起こす渦熱フラックスの正偏差はユーラシアの中央部と東部に分布

する事がわかった。ユーラシア中央部では気候平均場の低温域に北風偏差が分布することで、ユーラシア東部においては気候平均場の南風領域に高温偏差が分布することで、渦熱フラックスが正偏差となっていた。またそれぞれの偏差成分は、バレンツ・カラ海での海氷域減少により励起された準定常ロスビー波が、成層圏に上方伝播する事に伴って形成されていた。このプロセスは、北半球全域の海氷分布に多寡を与えた数値実験の結果においても整合的であった。以上より、少氷に伴う成層圏過程を駆動する惑星波上方伝播について、その際の大気場の 3 次元構造と BKS の重要性を示した。

極端な惑星波の上方伝播によって発生し、数日の間に極渦が急激に減速する極渦弱化 (weak polar vortex; WPV) イベントも、下方影響を通して中緯度の気候に影響を与える事が知られている。そこで、海氷域減少が WPV イベントに及ぼす影響と、それを通して中緯度気温場に与える影響を調べた。まず、WPV イベントを引き起こす惑星波の上方伝播過程に着目した。多氷年に発生した WPV では東西波数 1 成分の寄与が支配的であったのに対して、少氷年の WPV では東西波数 2 成分の強まりが特徴であった。この強まりは、バレンツ・カラ海域を波源とする準定常ロスビー波が気候平均場の波数 2 構造を強めた事に起因していた。この結果は、多氷、少氷をそれぞれ与えた数値実験で再現された WPV イベントを比較する事からも支持された。以上より、WPV イベント時においても、

定常ロスビー波応答を通して海氷域減少の影響が有る事を示した。さらに、WPV イベント発生後の特徴に関しても調べた。少氷年 WPV では、イベント発生に伴う極渦弱化シグナルの鉛直結合が多氷年 WPV に比べて強く、対流圏中緯度での東風偏差が約一ヶ月継続していた。これに伴い、中緯度陸域ではイベント発生後から数週間に渡り低温偏差が継続していた。これは、海氷域の減少が引き起こす中緯度寒冷化において、WPV イベントの変調を通したプロセスがある事を示唆する結果である。

基本場、WPV イベント時における成層圏過程が、北極−中緯度リンクに寄与している事が示されたが、現実の気候システムにおいては、極渦の変動は様々な現象による影響を受ける。そこで、少氷に伴う成層圏過程と北極−中緯度リンクに対する外的要因の影響を調べた。ここでは、熱帯成層圏における東西風の準二年振動 (Quasi-Biennial Oscillation; QBO) に着目した。QBO の西風 (QBOW) 位相時は、東風位相時 (QBOE) に比べて、極渦が強い傾向にある事が知られている。再解析データを用いて、QBO 位相別に海氷と大気の関係を調べた結果、少氷に伴う中緯度低温偏差は QBOE 年において明瞭である一方、QBOW 年では高温偏差となる事が分かった。QBOE 年における低温偏差は、対流圏におけるバレンツ・カラ海からの準定常ロスビー波応答と成層圏過程に伴って形成されていた一方、このような対流圏、成層圏の循環偏差は QBOW 年では見られなか

った。海氷分布や QBO など、観測された外部強制を与えて実施したヒストリカル実験においても整合的な結果が得られた。QBO による影響メカニズムは未解明であり今後の課題であるが、本結果により、北極–中緯度リンクの発現に対する成層圏基本場の役割がはじめて示唆された。

本研究では、北極–中緯度リンクにおける成層圏の役割のさらなる理解のために、上記 3 つの課題に取り組んだ。その結果、海氷域の減少が引き起こす惑星波上方伝播の時空間構造を、平均場と WPV イベント時について示した。また、海氷域の減少が引き起こす中緯度寒冷化には WPV イベントの変調を通したプロセスがある事、中緯度低温応答と成層圏過程は成層圏の QBO により変調されうる事を示した。これらは、少氷に伴う成層圏過程の新たなプロセスとして、本研究で明らかにされたものである。また、数値モデルにおいてこれらの現象の再現性が北極–中緯度リンクの再現性に影響を及ぼすという示唆を与える。一方で、北極–中緯度リンクのメカニズムについては、陸面の積雪分布や海洋を通したフィードバック、大気の内部変動による影響も含め、様々な対流圏内プロセスがこれまで提唱されてきた。しかし、これらの対流圏過程に対する成層圏過程の影響とその力学過程は十分に調べられていない。また、本研究では QBO による影響に着目したが、成層圏におけるオゾン分布や太陽活動 11 年周期変動などが、少氷に伴う成層圏過程に影響を及ぼしている事も考えられる。北極–中

緯度リンクに関わるプロセスを成層圏–対流圏結合の視点で包括的に理解する事が今後の課題である。

Contents

Chapter 1.

Research Background and Introduction

1.1. Arctic–Midlatitude Climate Linkage

The Arctic has experienced significant warming in the recent decades at a rate more than twice as fast as the global average (Shindell and Faluvegi, 2009; Cohen et al., 2014). This phenomenon is referred to as Arctic Amplification. The significant loss of the Arctic sea ice has been observed (see Figure 1.1 for a time series of the annual minimum of the Arctic sea ice extent, and Figure 1.2 for the sea ice concentration anomaly patterns for the autumn and winter seasons), and is likely a factor that contributes to the Arctic warming through a large amount of heat released from the open ocean in a cold season (Screen and Simmonds, 2010; Lang et al., 2017). However, other processes, such as poleward heat and moisture transports and changes in Arctic clouds may also be important (Kay and L'Ecuyer, 2013; Zhang et al., 2013; Gong et al., 2017). In contrast to the warming Arctic condition, the northern continents have frequently experienced cold spells and heavy snowfall events in the recent winters (Overland et al.,

2011; Johnson et al., 2018). Winter averaged land-surface temperatures over the midlatitudes, especially over central Eurasia, have shown a negative trend in the period from the 1990s to early 2010s (Figure 1.3) (Cohen et al., 2014; Kug et al., 2015). These contrasting features in the winter Northern Hemisphere are referred to as the "warm Arctic cold continents," and studies have discussed if the Arctic warming causes a colder condition in the winter midlatitudes (Vihma, 2014; Walsh, 2014; Overland et al., 2016; Francis, 2017; Screen et al., 2018; Vavrus, 2018).

The influences of the Arctic sea ice loss on cold anomalies over the midlatitudes were first pointed out by Honda et al. (2009). They found that strong cold spells often occurred over the central-to-eastern Eurasia in the winters following summers with anomalously small Arctic sea ice extents (e.g., 2005/2006 and 2007/2008). They conducted a set of sea ice sensitivity experiments using an atmospheric general circulation model (AGCM) to understand the causality and processes. Their results indicated that the reduced sea ice condition in the Barents–Kara Seas (BKS) and anomalous diabatic heating from the open ocean during the late fall to early winter reinforce the quasi-stationary Rossby wave response at the middle to upper troposphere. This wave response composed of anticyclonic anomalies over the BKS and cyclonic anomalies over the central Eurasia results in a strengthened surface Siberian high with

cold air advection toward the eastern Eurasia. Other studies later reported similar results on the sea ice influences on temperatures over the eastern Eurasia based on observation (Hopsch et al., 2012; Inoue et al., 2012; Cohen et al., 2014) and numerical simulation (Petoukhov and Semenov, 2010; Rinke et al., 2013; Kim et al., 2014; Mori et al., 2014; 2019; Nakamura et al., 2015).

The colder conditions over the northern midlatitudes may also be related to the weakened/meandered westerlies. Based on an observational analysis, Francis et al. (2009) suggested that an increased heat release from the Arctic Ocean reduces the poleward thickness gradient that weakens the westerlies in the fall and winter seasons. Francis and Vavrus (2012) further discussed that the Arctic warming contributes to larger amplitudes and slower progressions of the Rossby waves in midlatitudes, thereby causing a more persistent and extreme weather.

Warmer Arctic conditions and weakened/meandered westerlies are partly associated with a negative phase of the Arctic Oscillation (AO; Thompson and Wallace, 1998; 2000)/North Atlantic Oscillation (NAO; Walker and Bliss, 1932; van Loon and Rogers, 1978). The AO/NAO is a dominant mode of atmospheric variability in the Northern Hemisphere, and affects a wide-range of weather patterns (Wallace and Gutzler, 1981; Thompson and Wallace, 1998). A negative phase of the AO/NAO

corresponds to high-pressure anomalies over the pole and low-pressure anomalies over the midlatitudes. Overland et al. (2011) discussed the impact of the sea ice loss on the negative NAO condition in the winter of 2009/10, in which heavy snow and low-temperature events were observed in midlatitudes. Based on statistical analyses, other studies obtained similar results; Arctic sea ice loss is related to the negative AO/NAO-like circulation anomaly and the midlatitude cold condition (Overland and Wang, 2010; Hopsch et al., 2012; Jaiser et al., 2012; Liu et al., 2012). Studies based on the AGCM simulations also found similar negative AO/NAO-like circulation anomalies in winter as response to the reduced sea ice condition (Alexander et al., 2004; Deser et al., 2004; Magnusdottir et al., 2004; Seierstad and Bader., 2009; Nakamura et al., 2015; Screen, 2017a).

One of the mechanisms formulating the negative AO/NAO-like circulation anomalies is the strong surface warming caused by sea ice loss and the increases in thickness of the lower atmosphere over the Arctic region (Alexander et al., 2004). The weakened synoptic-scale eddy activities over the northern North Atlantic caused by the high-latitude warming also amplifies and/or maintains the negative AO/NAO-like meridional dipole pattern through the eddy feedback forcing (Lau and Nath, 1991; Deser et al., 2007; Limpasuvan and Hartmann, 2000). Planetary-scale waves (hereafter,

referred to as planetary waves) that are reinforced by the sea ice loss forcing contribute to the negative shifts of the AO/NAO through the wave–mean flow interaction in the troposphere (Nakamura et al., 2015; 2016b; Smith et al., 2017). In addition to the processes within the troposphere, studies have discussed that processes in the stratosphere also play an important role in formulating negative AO/NAO anomalies in the troposphere. Kim et al. (2014) suggested that the weakened signals of the stratospheric polar vortex caused by the sea ice loss contribute to the formulation of the tropospheric negative AO/NAO anomaly. Furthermore, recent studies pointed out that this stratospheric process is necessary for the tropospheric responses to the sea ice loss (Nakamura et al., 2016a; Wu and Smith, 2016; Zhang et al., 2018b); thus, the stratospheric processes and their role on the tropospheric circulation anomalies need further understanding.

1.2. Stratospheric Pathway Caused by Arctic Sea Ice Loss

Tropospheric AO-like circulation anomalies tend to be accompanied by the preceded signals in the stratospheric polar vortex (Baldwin and Dunkerton, 1999), suggesting a contribution of the stratospheric signals to the tropospheric AO anomalies

through the downward influences. Anomalies in the polar vortex have been known to be caused by vertical planetary wave propagation and the interaction of these waves with the zonally averaged circulation. Significant upward wave propagation results in a rapid weakening of the polar vortex over a matter of several days, which is known as sudden stratospheric warming (SSW) (Matsuno, 1971; Schoeberl, 1978; Limpasuvan et al., 2004). After an occurrence of SSW events, a phase of the tropospheric AO/NAO also shifts toward the negative because of the descending weakened zonal wind signals from the stratosphere (Figure 1.4) and cold spells tend to occur in the midlatitudes for approximately 60 days (Baldwin and Dunkerton, 2001; Thompson et al., 2002). Considering the stratosphere–troposphere coupling process is important in understanding the tropospheric climate variations (Kidston et al., 2015) and the tropospheric sub-seasonal weather forecasts (Sigmond et al., 2013; Tripathi et al., 2015; Karpechko, 2018).

An influence of the Arctic sea ice loss on the stratospheric circulation was discussed by Jaiser et al. (2013), who found that the stratospheric polar vortex tends to weaken in association with the enhanced upward planetary wave propagation in the low-ice period (2001–2012) compared with the high-ice period (1980–2000). Kim et al. (2014) argued a role of the BKS sea ice loss on the enhanced upward wave propagation

by extending the results of Honda et al. (2009). Based on an AGCM simulation and an observation analysis, they identified that a deepening of the climatological Siberian trough due to the stationary Rossby wave response to the BKS sea ice reduction enhances the upward wave propagation toward the stratosphere and weakens the polar vortex in the early winter. They further pointed out that the downward influences of the weakened polar vortex signals led to tropospheric negative AO/NAO anomalies and colder midlatitude surface conditions in late winter. Although Kim et al. obtained those results based on a low-top model of approximately 3 hPa, other studies supported their results based on stratosphere-resolved high-top models (Nakamura et al., 2015; Sun et al., 2015; Zhang et al., 2018a) and reanalysis data (García-Serrano et al., 2015; Jaiser et al., 2016; King et al., 2016; Yang et al., 2016). Observations further indicated that late fall to early winter sea ice variations are strongly correlated with the mid-winter stratospheric polar vortex variations (García-Serrano et al., 2015; King et al., 2016), suggesting that the early winter sea ice variations are most critical for the following atmospheric circulation.

Contribution of the stratospheric process to the tropospheric negative AO/NAO responses was also examined based on AGCM experiments. One approach was to investigate the stratospheric contribution by nudging. The wave–mean flow interaction

in the stratosphere was suppressed in such a way that the zonal mean component of the stratospheric zonal winds were nudged toward the climatological state. This method allowed us to examine the stratospheric role in a single model. Nakamura et al. (2016a) conducted this type of experiment with a focus on the recent sea ice loss impacts and found that the stratospheric pathway and the tropospheric negative AO-like anomalies disappeared when the stratospheric wave–mean flow interaction was suppressed. Wu and Smith (2016) conducted a similar experiment and found that approximately one half of the magnitude of the tropospheric westerly response to the Arctic Amplification was induced by the stratospheric pathway. Zhang et al. (2018b) performed an experiment in which the weakened polar vortex condition obtained from the lower sea ice experiment was nudged. Comparing this result with that of the non-nudged experiment, they indicated that the downward influence of the stratospheric anomalies was crucial for the Eurasian cold response to the sea ice loss.

The other approach was to compare high-top model results with low-top model results, thereby addressing the role of the stratosphere. Note that high-top models simulating the whole stratospheric circulation tend to reproduce more realistic strength (Boville 1984; Boville and Cheng 1988; Shaw and Perlwitz 2010) and variability (Sassi et al. 2010; Charlton-Perez et al., 2013) of the polar vortex compared with low-top

models that do not simulate the whole stratospheric circulation. Sun et al. (2015) conducted sensitivity experiments of the future Arctic sea ice loss forcing using two AGCMs, a high-top model (Whole Atmosphere Community Climate Model; WACCM) and its low-top counterpart (Community Atmosphere Model version 4; CAM4). Their results indicated that only the high-top model reproduced the weakened polar vortex and tropospheric cold midlatitude anomalies as responses to the reduced sea ice condition. A comparison between the high- and low-top models from the Coupled Model Intercomparison Project phase 5 (CMIP5; Taylor et al., 2012) archive also indicated that the former captured stronger stratospheric responses with a prolonged impact on the midlatitude circulation in response to the Arctic sea ice loss (De and Wu, 2019).

The results strongly suggest the critical role of the stratospheric processes on the tropospheric response to the Arctic sea ice loss. Moreover, the stratospheric process links the early-winter sea ice loss with the mid to late winter tropospheric circulation, therefore could contribute to the prolonged tropospheric circulation responses. These notions are the strong motivation of this thesis in investigating the atmospheric responses to the Arctic sea ice loss in a stratosphere–troposphere coupled system.

1.3. Discrepancies of Atmospheric Response to Arctic Sea Ice Loss

Most of the previous studies focused on the mean state response of the stratospheric polar vortex to the sea ice loss, whereas only a few studies examined the SSW response to the sea ice loss. Thus, a question regarding the SSW responses to the sea ice loss has remained as a matter for further investigation. Two studies reported that no statistically significant change is observed in a frequency of the SSW events as a response to the future Arctic sea ice loss (Sun et al., 2015) and Arctic Amplification (Wu and Smith, 2016). However, the models used in these studies underestimated the climatological SSW frequency compared with the observation. This likely leads to a less sensitivity of the SSW frequency response. Therefore, concluding the influences on the SSW frequencies from those two studies seemed to be difficult.

Although the frequency of SSWs has been investigated in the previous studies, the sea ice variations may modulate the characteristics of the SSW events (e.g., a type of SSW event: displacement- or split-type SSWs shown in Figure 1.5). For example, the El Niño-Southern Oscillation (ENSO) is a potential factor modulating the SSW characteristics; the significant zonal wavenumber-1 (WN1) upward propagation and the displacement-type SSW are frequently observed during El Niño winters, whereas the zonal wavenumber-2 (WN2) upward propagation and split-type SSW are relatively

frequently observed during La Niña winters (Taguchi and Hartmann, 2006; Barriopedro and Calvo, 2014; Song and Son, 2018). A response of the SSWs to the Arctic sea ice loss has not yet been well studied; hence, further investigation would clarify the unknown SSW features modulated by the Arctic sea ice loss.

As reviewed in the previous section, an importance of the stratospheric pathway for the tropospheric responses to the sea ice loss has been reported. However, the mean state stratospheric responses could change by the different forcing locations and magnitudes of the sea ice anomalies. Sun et al. (2015) examined impacts from different forcing locations, and obtained opposite responses in the polar vortex from experiments in which the sea ice loss anomalies were prescribed over the Atlantic or Pacific sectors separately. Particularly, the upward wave propagation in the latter was suppressed by the weakened climatological Siberian trough because of the sea ice-induced surface warming. Peings and Magnusdottir (2014) discussed the impacts from different sea ice anomaly magnitudes, although their model was a low-top model. They showed that the present sea ice loss forcing induces weakened stratospheric polar vortex anomalies, whereas the future forcing results in an absence of stratospheric anomalies. These results suggest that the stratospheric responses are likely sensitive to forcing regions and magnitudes. Thus, details of the stratospheric circulation responses to the recent Arctic

sea ice loss and of the upward planetary wave propagation processes should be studied.

Peings and Magnusdottir (2014) also showed that the future sea ice loss resulted in significant surface warming and stronger anticyclonic anomalies over the Arctic at the mid-upper troposphere compared with the present sea ice loss results. Other studies also identified the stronger tropospheric anticyclonic anomalies with a lack of stratospheric responses as the responses to stronger surface forcings, such as ice-free conditions across the entire Arctic Ocean in winter (Nakamura et al., 2016b), and prescribed surface temperature anomalies that correspond to a late 21st century sea ice loss (McKenna et al., 2018). Their results suggest that tropospheric processes become relatively more important than the stratospheric processes when the surface forcing magnitude largely increases.

Different tropospheric responses to the Arctic sea ice loss have also been reported by modeling studies. For example, the simulated tropospheric AO/NAO responses ranged from the negative phase (Honda et al., 2009; Seierstad and Bader., 2009; Mori et al., 2014; Kim et al., 2014; Nakamura et al., 2015; Deser et al., 2016; Screen, 2017a), positive phase (Singarayer et al., 2006; Strey et al., 2010; Orsolini et al., 2012; Rinke et al., 2013; Cassano et al., 2014; Screen et al., 2014), to little response (Screen et al., 2013; Petrie et al., 2015; Blackport and Kushner, 2016). Other studies pointed out that

the AO/NAO response depended on the amount of sea ice reduction (Alexander et al., 2004; Petoukhov and Semenov, 2010; Peings and Magnusdottir, 2014; Nakamura et al., 2016b) and on the location of the sea ice reduction (Sun et al., 2015; Pedersen et al., 2016; McKenna et al., 2017; Screen, 2017b). The temperature responses in the midlatitudes to the Arctic sea ice loss are also different among modeling studies. Several studies simulated midlatitude cold anomalies caused by the sea ice loss (Honda et al., 2009; Mori et al., 2014; Nakamura et al., 2015; Koenigk et al., 2018), whereas some other studies found no evidence of the Arctic sea ice loss having an impact on the surface temperature over Eurasia (McCusker et al., 2016; Sun et al., 2016; Ogawa et al., 2018).

It can be suggested that the difference in the stratospheric processes is one of the reasons of the discrepancy of these tropospheric responses among the model results. Another possible cause that have discussed in recent years is the influence of the background states. Smith et al. (2017) found that a sign of the NAO response to the Arctic sea ice loss depends on the atmospheric background state related to the global climatological sea surface temperature (SST) conditions. They particularly suggested that the different atmospheric background condition controls the planetary wave propagation that induces the negative NAO response based on the refractive index

diagnostic (Andrews et al., 1987; Li et al., 2007). Li et al. (2018) also examined the role of the background conditions related to the Atlantic multi-decadal oscillation (AMO) based on the reanalysis data. Note that AMO is a multidecadal variability of SST over the North Atlantic (Schlesinger and Ramankutty, 1994). Li et al. also found that the early winter Eurasian cold anomalies and the late winter negative AO/NAO anomalies associated with the low sea ice condition were seen only in winters with the negative (cold) AMO phase. Air–sea coupling in a model is likely another potential factor that changes the midlatitude temperature responses to the sea ice loss (Decer et al., 2016; Blackport and Kushner, 2017).

In addition to different background states associated with SST states, we postulate that the stratospheric background condition is another possible factor that can change the stratospheric pathway and tropospheric responses to the sea ice loss. It has been reported that the stratospheric polar vortex is influenced by many factors, such as the Eurasian snow cover extent (Cohen et al., 2007; 2014; Fletcher et al., 2009; Peings et al., 2012), the ENSO (Manzini et al., 2006; Free and Seidel, 2009; Fletcher and Kushner, 2011), the quasi-biennial oscillation (QBO) (Holton and Tan, 1980; 1982; Baldwin et al., 2001; Anstey and Shepherd, 2014), the 11-year solar cycle (Kodera and Kuroda, 2002; Kuroda and Kodera, 2002), and their combinations (Kodera, 1991; Naito

and Hirota, 1997; Kryjov and Park, 2007; Wei et al., 2007; Calvo et al., 2009; Peings et al., 2017).

The ozone chemistry is another possible factor that changes the atmospheric responses to the sea ice loss. The ozone distribution is usually prescribed as an external forcing in the AGCM experiments, but it can respond to the sea ice loss (Sun et al., 2014) and then provide feedbacks on the stratospheric circulation (Randel et al., 2009; Previdi and Polvani, 2014). Romanowsky et al. (2019) found that the stratospheric pathway and a negative NAO response were strengthened in an AGCM simulation that included interactive stratospheric ozone chemistry compared with a simulation without interactive chemistry. Although its mechanism was not made clear, their results suggested the importance of the realistic stratospheric background process for both stratospheric and tropospheric responses to the sea ice loss. Very few attempts have been made to investigate the roles of the stratospheric background state, but we postulate that the stratospheric background condition is a possible factor in modulating the atmospheric responses to sea ice variations.

1.4. Research Aim

The northern continents have experienced severe weather and cold winters in the recent decades, and the influence of the Arctic sea ice loss on those has been discussed. We here aim at better understanding the role of the stratospheric processes in the influences of the Arctic sea ice loss. Several science questions were addressed in the review above. These questions were investigated by dividing them into three topics, which are described in the paragraphs below. This study mainly analyzes the reanalysis data to examine the observed climate variations. The AGCM simulation results, which are a useful tool in understanding the causalities and underlying dynamics of the phenomena that occur in a short observation period, are also analyzed. Chapter 2 describes the details of these data.

The first topic is detailes in the upward planetary wave propagation associated with the recent Arctic sea ice reduction (Chapter 3). The poleward eddy heat flux v^*T^*, which is a product of the eddy components (deviations from the zonal mean) of meridional wind and temperature, is an indicator of the strength of the vertical wave propagation (Polvani and Waugh, 2004). We investigate the detailed atmospheric three-dimensional (3D) structure that induces the heat flux anomalies, and a source sea ice loss region that reinforces the planetary wave propagation.

The second topic is influences of the sea ice loss on the stratospheric extreme events, such as SSWs (Chapter 4). Note that SSW events involve a rapid weakening of the polar vortex and tend to cause significant tropospheric circulation anomalies and the midlatitude cooling. In addition to the mean state stratospheric responses discussed above, we postulate that the SSW would also be modulated by the Arctic sea-ice anomalies. This thesis particularly examines if and how the sea-ice loss modulates the zonal wavenumber components in a planetary scale and the spatial structures of the significant upward wave propagation. This thesis also examines the characteristics of the stratosphere–troposphere vertical coupling that influences on the surface weather.

The third topic is a role of the stratospheric background state for the Arctic sea ice impacts (Chapter 5). We hypothesize that the different background condition of the stratospheric polar vortex is a potential factor that can modify the stratospheric pathway and tropospheric circulation responses to the sea ice variations. We approach this speculation using the QBO-phase. Note that the QBO is a phenomenon that consists of alternating westerly and easterly zonal winds in the equatorial stratosphere, and strongly modulates the interannual variation of the stratospheric polar vortex. The polar vortex is weaker during the easterly phase of the QBO and stronger during the westerly phase of the QBO, known as the Holton–Tan relationship (Holton and Tan, 1980; Anstey and

Shepherd, 2014). We examine whether or not a different stratospheric background state related to the QBO can modulate the Arctic–midlatitude climate linkage.

All materials in this thesis are either already published or are being prepared for submission. The results in Chapter 3 have been published in Geophysical Research Letters as Hoshi et al. (2017). Chapter 4 is composed of the results of Hoshi et al. (2019a) and Hoshi et al. (2019b) published in the Journal of Geophysical Research: Atmosphere and Kaiyo Monthly (in Japanese), respectively. The results in Chapter 5 are being prepared for submission to an international journal as a research article.

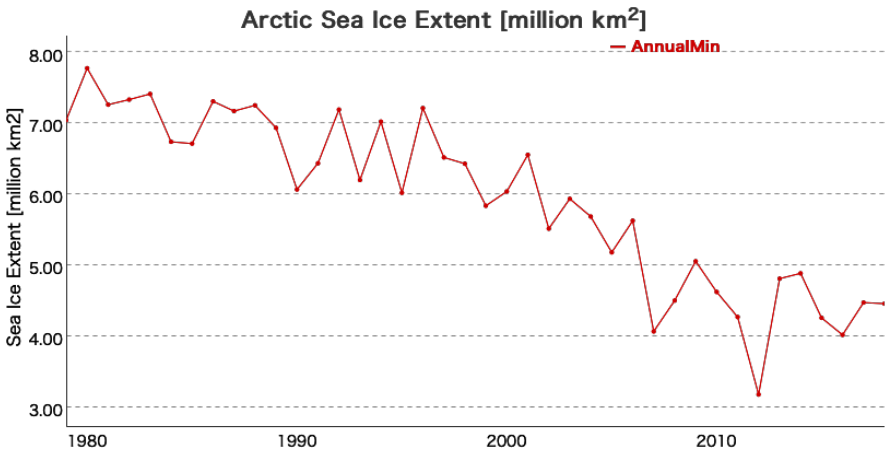

Figure 1.1 A time series of annual minimum Arctic sea ice extent (10^6 km) from 1979 to 2018. The figure is provided by VISHOP (https://ads.nipr.ac.jp/vishop/#/monitor).

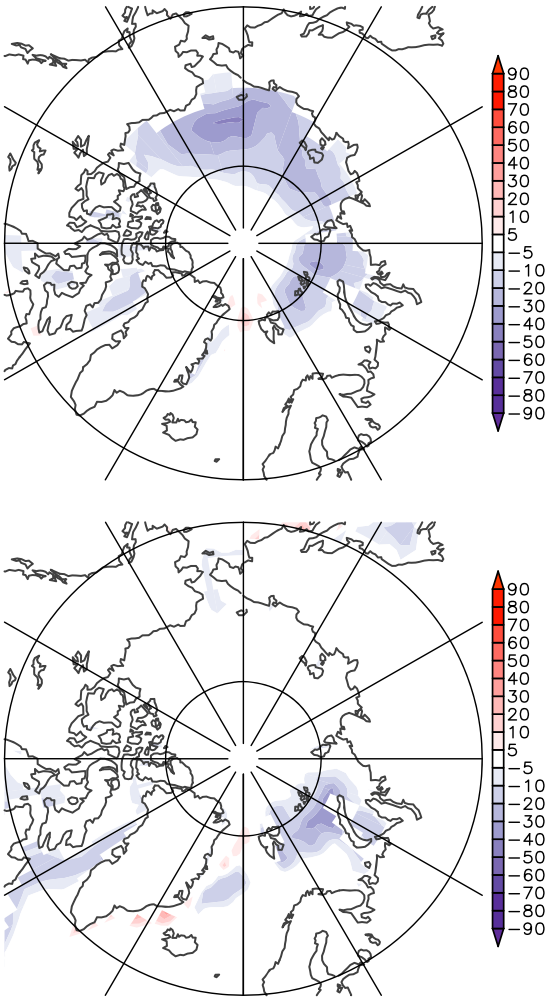

Figure 1.2 Sea ice concentration anomalies (%) between low-ice period (2000/2001–2013/2014) and high-ice period (1979/1980–1999/2000) for autumn season (September to October; above) and winter season (December to February; below), from ERA-Interim. (From Jaiser et al., 2016)

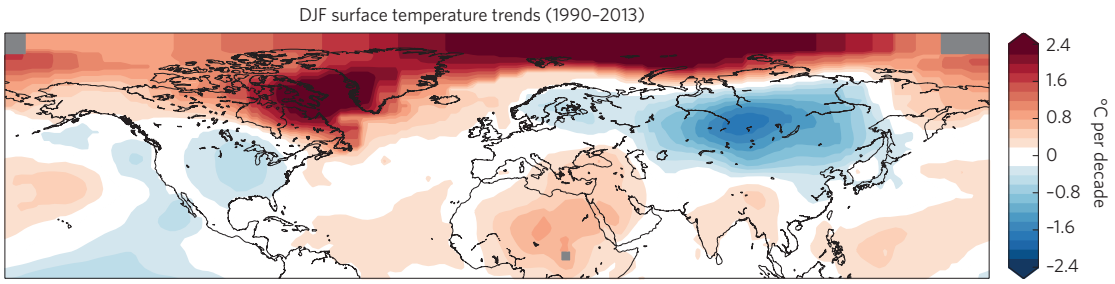

Figure 1.3 Linear trend (°C per 10 years) in December–February (DJF) mean surface air temperatures from 1990/1991 to 2013/2014. Data from the National Aeronautics and Space Administration Goddard Institute for Space Studies temperature analysis (http://data.giss.nasa.gov/gistemp). (From Cohen et al., 2014)

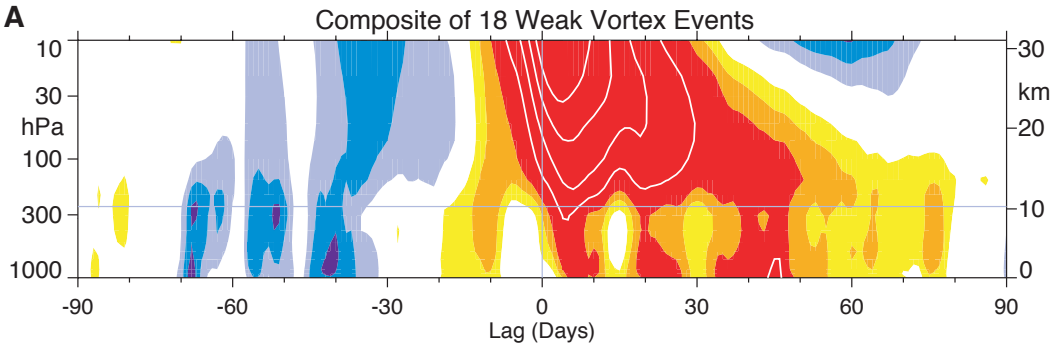

Figure 1.4 Composite of time–height development of the Northern Annular Mode (NAM) for 18 weak vortex events. The events are determined by the dates on which the 10 hPa annular mode values cross −3.0. The indices are non-dimensional; the interval is 0.25 for the color shading, and 0.5 for the white contours. Values between −0.25 and 0.25 are unshaded. The thin horizontal lines indicate the approximate boundary between the troposphere and the stratosphere. (From Baldwin and Dunkerton, 2001)

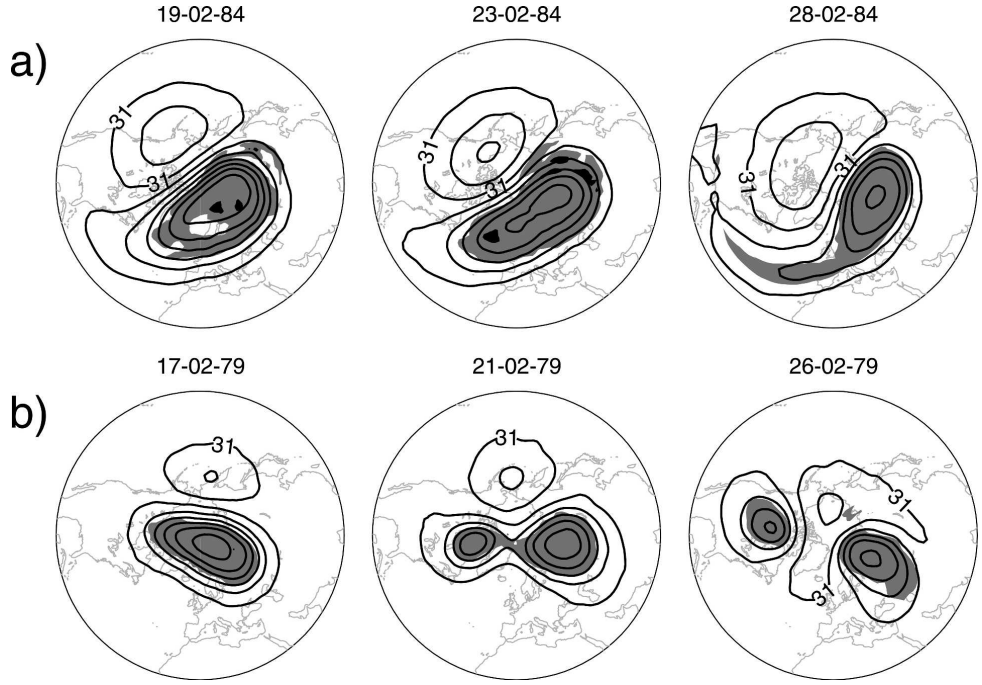

Figure 1.5 Polar stereographic plot of geopotential height (contours; km) on the 10 hPa pressure surface. The contour interval is 0.4 km, and the shading shows potential vorticity greater than 4.0 (10^{-6} K kg^{-1} m^2 s^{-1}). (a) A displacement-type SSW event that occurred in February 1984. (b) A split-type SSW event that occurred in February 1979. (From Charlton and Polvani, 2007)

Chapter 2.

Data and Methods

2.1. Observation-based Datasets

We used the Japanese 55-year Reanalysis (JRA-55) (Kobayashi et al., 2015; Harada et al., 2016) with a 1.25° horizontal resolution and 37 vertical levels (1000–1 hPa) for the atmospheric data. The monthly mean and 6 hourly temporal resolutions are available from 1958 up to the present. The Hadley Centre Sea Ice and Sea Surface Temperature dataset version 1 (HadISST1; Rayner et al., 2003) was used for the sea ice concentration (SIC) and SST with a 1° spatial and monthly temporal resolutions. The Hadley Centre Sea Ice and Sea Surface Temperature dataset version 2.2.0.0 (HadISST2; Titchner and Rayner, 2014) was also used. This provides the SIC data that were updated from the previous version, HadISST1. The HadISST1 and HadISST2 datasets cover the period from 1870 and 1850, respectively. This study analyzed the period from 1979/1980, in which high-quality sea ice data were available from satellite measurements. Table 2.1 summarizes the datasets and periods analyzed in the chapters

that follow. This study also used the monthly Niño 3.4 anomaly provided by the National Oceanic and Atmospheric Administration-Climate Prediction Center (NOAA-CPC).

In the observation analyses, we basically examined the relationship between sea ice and atmospheric variations. A sea ice time-series was used as the measure of sea ice variation. Previous studies discussed that the sea ice conditions from late fall to early winter in the BKS were the most relevant to the tropospheric and stratospheric responses (García-Serrano et al., 2015; Nakamura et al., 2015; King et al., 2016). Thus, this thesis computed the time-series as an area-averaged SIC over the BKS in early winter. Slightly different region and month were used in the chapters that follows (Table 2.2).

2.2. Numerical Simulations

Two results of AGCM experiments, namely a time-slice experiment and a historical experiment, were analyzed. The simulations were conducted in the Green Network of Excellence (GRENE) Arctic Climate Change Research Project and the Arctic Challenge for Sustainability (ArCS) Project. The AGCM for the Earth Simulator

(AFES) (Ohfuchi et al., 2004; Enomoto et al., 2008; Kuwano-Yoshida et al., 2010) version 4.1 was used with triangular truncation at the horizontal wavenumber 79 (T79; approximately 1.5° horizontal resolution) and 56 vertical levels. The model top was at approximately 60 km, thereby simulating the whole stratospheric circulation as well as the SSWs. The values of the turbulent heat flux over the Arctic were carefully tuned to examine the sea ice loss impacts on the atmospheric circulation (Nakamura et al., 2015). Note that this model does not treat SIC directly; instead, each model grid cell is either treated as being ice-covered or ice-free. To allow the model to represent a reasonable amount of the turbulent heat flux associated with variable SIC, SIC data were converted into SIT. A maximum ice thickness in the Arctic was assumed to be 50 cm so that SIC from 0% to 100% was linearly converted into SIT from 0 to 50 cm. Then, grid cells where converted SIT was less than 5 cm were set to have no ice (i.e., 0 cm). Although 50 cm is much thinner than a typical Arctic SIT value, the turbulent heat flux over sea ice is simulated reasonably well due to the large reduction in the conductive heat flux through sea ice thicker than 30–50 cm (Maykut, 1982). Observation-based estimates of the turbulent heat flux in the Arctic are about −10 W m^{-2} over the fully sea ice-covered region and about 300–320 W m^{-2} over the open-water region (Maykut, 1982; Renfrew et al., 2002). Figure 2.1 shows the simulated turbulent heat flux over the Arctic, which

was comparable with the observations.

One type of experiments used herein was the time-slice experiment, which was also analyzed in Nakamura et al. (2015), Jaiser et al. (2016), and Crasemann et al. (2017). The integrations of two runs were conducted for 60 years after an 11 year spin-up under the same settings, except for the Northern Hemisphere sea ice conditions. One run used the average annual cycle of the heavy-ice period (1979 to 1983; HICE run), while the other used the average annual cycle of the light-ice period (2005 to 2009; LICE run). The same average annual cycle of 1979 to 1983 was used for the global SST and Southern Hemisphere sea ice condition. The boundary condition data were assembled from the merged Hadley-National Oceanic and Atmospheric Administration/Optimum Interpolation Sea Surface Temperature and Sea-Ice Concentration datasets (Hurrell et al., 2008). The other external forcings were fixed as follows: 380 ppmv for CO_2, 1.8 ppmv for CH_4, and the monthly climatological mean ozone for 1979–2011 obtained from the Japanese 25-year Reanalysis (JRA-25)/Japan Meteorological Agency Climate Data Assimilation System (JCDAS) reanalysis data (Onogi et al., 2007). The default values of aerosol and incident solar radiation were used. The same initial condition was used (the January 1979 monthly mean from JRA-25/JCDAS). By this experimental design, only the sea ice difference is responsible

for the atmospheric differences. The daily mean outputs are available.

The other type of experiments is a historical experiment. The integration was conducted during the period of 1979 to 2014 after a 1 year spin-up with 30 ensemble members. The following historical climate forcings were prescribed: annual mean greenhouse gases (CO_2 and CH_4) and monthly mean sea ice, SST, ozone, and QBO. The sea ice and SST data were obtained from Hurrell et al. (2008). The European Centre for Medium-range Weather Forecasts (ECMWF) ERA-Interim reanalysis data (Dee et al., 2011) were used for the ozone and the QBO forcings. A zonal mean component of the zonal winds in the equatorial stratosphere was nudged toward the observed values to prescribe the QBO. Figure 2.2 shows the nudging region and its intensity. The equatorial zonal mean zonal winds were quite similar between the reanalysis data (JRA-55) and the simulated results (Figure 2.3). The default values of aerosol and incident solar radiation were used, providing no historical volcanic and solar effects in this simulation. Accordingly, 6 hourly outputs were available.

The time-slice experiment is analyzed in Chapters 3 and 4, and the historical experiment is presented in Chapter 5 (Table 2.1).

2.3. Diagnostic Methods of Wave Propagation in the Atmosphere

This section introduces the diagnostic methods of wave propagation, including the wave-activity fluxes. The Transformed Eulerian Mean (TEM) formulation is a useful tool for diagnosing wave propagation and the impacts on the zonal mean circulation in the two-dimensional (2D) meridional plane (Andrews and McIntyre, 1976; Andrews et al., 1987; Holton and Hakim, 2013). The TEM formulation for the quasi-geostrophic β-plane case in the log-pressure coordinate system is written as

$$\frac{\partial \bar{u}}{\partial t} - f_o \overline{v_r} = \frac{1}{\rho_0} \nabla \cdot \boldsymbol{F} + \bar{X} ,$$

$$\frac{\partial \bar{T}}{\partial t} + \frac{N^2 H}{R} \overline{w_r} = \frac{\bar{J}}{C_p} ,$$

$$\frac{\partial \overline{v_r}}{\partial y} + \frac{1}{\rho_0} \frac{\partial (\rho_0 \overline{w_r})}{\partial z} = 0 ,$$

where, $(\overline{v_r}, \overline{w_r})$ are the meridional and vertical components of the residual meridional circulation, respectively.

$$\overline{v_r} = \bar{v} - \frac{1}{\rho_0} \frac{R}{H} \frac{\partial}{\partial z} \left(\frac{\rho_0 \overline{v^* T^*}}{N^2} \right),$$

$$\overline{w_r} = \bar{w} + \frac{R}{H} \frac{\partial}{\partial y} \left(\frac{\overline{v^* T^*}}{N^2} \right).$$

$\boldsymbol{F} = \left(F_y, F_z\right)$ is a wave-activity flux, referred to as the Eliassen–Palm (E–P) flux:

$$F_y = -\rho_0 \overline{u^* v^*} , F_z = \rho_0 \frac{f_0 R}{N^2 H} \overline{v^* T^*} ,$$

where, $\overline{(\ \ )}$, and $(\ \ )^*$ denote the zonal mean and the eddies (deviation from zonal mean), respectively, and z designates the log-pressure variable. u, v, w, and T are the zonal wind, meridional wind, vertical wind, and temperature, respectively. $\bar{X}$ designates the zonal component of drag caused by the small-scale eddies. ρ_0, N, R, and f_0 are the basic state density, Brunt–Väisälä frequency, gas constant for dry air, and Coriolis parameter, respectively. The meridional and vertical components of the E–P flux are proportional to the poleward eddy momentum and heat fluxes, respectively.

The TEM formulation clearly shows that the eddy momentum and the heat fluxes do not act separately to drive the changes in the zonal mean circulation, but wave forcing can be estimated by the combination given by the divergence of the E–P flux. It further represents that those wave forcings are used to drive the zonal wind acceleration and residual meridional circulation. On the seasonal time-scale ($\frac{\partial \bar{u}}{\partial t} \approx 0$), the wave forcing is nearly balanced by the eastward Coriolis force of the residual meridional circulation. In a case of a SSW event, the wave forcing leads to a deceleration of the zonal mean zonal wind partially offset by the Coriolis force. The TEM formulation further shows that the net temperature change can be estimated by the residual vertical motion under an adiabatic condition, as shown in the second equation.

The alternative form of the TEM formulation derived from the primitive equation

in the spherical coordinate (Andrews et al., 1987) is written as follows

$$\frac{\partial \bar{u}}{\partial t} + \overline{v_r}\left[\frac{1}{a\cos\emptyset}\frac{\partial}{\partial \emptyset}(\bar{u}\cos\emptyset) - f\right] + \overline{w_r}\frac{\partial \bar{u}}{\partial z} - \bar{X} = \frac{1}{\rho_0 a\cos\emptyset}\nabla\cdot\boldsymbol{F},$$

where $(\overline{v_r}, \overline{w_r})$ is a residual meridional circulation defined as

$$\overline{v_r} = \bar{v} - \frac{1}{\rho_0}\frac{\partial}{\partial z}\left(\rho_0 \frac{\overline{v^*\theta^*}}{\frac{\partial \bar{\theta}}{\partial z}}\right),$$

$$\overline{w_r} = \bar{w} + \frac{1}{a\cos\emptyset}\frac{\partial}{\partial \emptyset}\left(\cos\emptyset \frac{\overline{v^*\theta^*}}{\frac{\partial \bar{\theta}}{\partial z}}\right).$$

The meridional and vertical components of the E–P flux are written as follows

$$F_\emptyset = \rho_0 a\cos\emptyset\left(\frac{\partial \bar{u}}{\partial \bar{z}}\frac{\overline{v^*\theta^*}}{\frac{\partial \bar{\theta}}{\partial z}} - \overline{u^*v^*}\right),$$

$$F_z = \rho_0 a\cos\emptyset\left(\left[f - \frac{\frac{\partial \bar{u}\cos\emptyset}{\partial \emptyset}}{a\cos\emptyset}\right]\frac{\overline{v^*\theta^*}}{\frac{\partial \bar{\theta}}{\partial z}} - \overline{u^*w^*}\right),$$

where $\emptyset$ and z are latitude and logarithmic pressure height, respectively; θ, a, and f are potential temperature, Earth's radius, and Coriolis parameter, respectively. A divergence of the E–P flux is written as follows,

$$\nabla\cdot\boldsymbol{F} = \frac{1}{a\cos\emptyset}\frac{\partial(\cos\emptyset F_\emptyset)}{\partial \emptyset} + \frac{\partial F_z}{\partial z}.$$

This form of the TEM formulation is used in the analyses in the following chapters for a more accurate estimation of the E–P flux and wave forcing.

Although the TEM formulation is a useful tool to understand the role of waves on zonally averaged circulation changes, the flux does not represent a zonal wave propagation. Plumb (1985) derived the 3D wave-activity flux for quasi-geostrophic stationary waves on the zonally homogeneous flow. This was quite useful in analyzing the passages where the planetary waves propagate to the stratosphere in a 3D space. The wave-activity flux in the spherical, log-pressure coordinate is written as

$$\boldsymbol{F_s} = p\cos\emptyset \begin{pmatrix} \frac{1}{2a^2\cos^2\emptyset}\left[\left(\frac{\partial\psi^*}{\partial\lambda}\right)^2 - \psi^*\frac{\partial^2\psi^*}{\partial\lambda^2}\right] \\ \frac{1}{2a^2\cos\emptyset}\left[\frac{\partial\psi^*}{\partial\lambda}\frac{\partial\psi^*}{\partial\emptyset} - \psi^*\frac{\partial^2\psi^*}{\partial\lambda\partial\emptyset}\right] \\ \frac{2\Omega^2\sin^2\emptyset}{N^2a\cos\emptyset}\left[\frac{\partial\psi^*}{\partial\lambda}\frac{\partial\psi^*}{\partial z} - \psi^*\frac{\partial^2\psi^*}{\partial\lambda\partial z}\right] \end{pmatrix},$$

where, ψ, a, p, $\emptyset$, and λ are the geopotential stream-function, the mean radius of the earth, pressure (hPa)/1000 hPa, longitude, and latitude, respectively.

A strong meandering of the background westerlies exists in the boreal winter troposphere. We used the wave-activity flux formulated by Takaya and Nakamura (1997; 2001) to represent the 3D propagation of the quasi-stationary Rossby waves on the zonally inhomogeneous flow:

$$\boldsymbol{W} = \frac{p\cos\emptyset}{2|\boldsymbol{U}|}\begin{pmatrix} \frac{U}{a^2\cos^2\emptyset}\left[\left(\frac{\partial\psi'}{\partial\lambda}\right)^2 - \psi'\frac{\partial^2\psi'}{\partial\lambda^2}\right] + \frac{V}{a^2\cos\emptyset}\left[\frac{\partial\psi'}{\partial\lambda}\frac{\partial\psi'}{\partial\emptyset} - \psi'\frac{\partial^2\psi'}{\partial\lambda\partial\emptyset}\right] \\ \frac{U}{a^2\cos\emptyset}\left[\frac{\partial\psi'}{\partial\lambda}\frac{\partial\psi'}{\partial\emptyset} - \psi'\frac{\partial^2\psi'}{\partial\lambda\partial\emptyset}\right] + \frac{V}{a^2}\left[\left(\frac{\partial\psi'}{\partial\emptyset}\right)^2 - \psi'\frac{\partial^2\psi'}{\partial\emptyset^2}\right] \\ \frac{{f_0}^2}{N^2}\left\{\frac{U}{a\cos\emptyset}\left[\frac{\partial\psi'}{\partial\lambda}\frac{\partial\psi'}{\partial z} - \psi'\frac{\partial^2\psi'}{\partial\lambda\partial z}\right] + \frac{V}{a}\left[\frac{\partial\psi'}{\partial\emptyset}\frac{\partial\psi'}{\partial z} - \psi'\frac{\partial^2\psi'}{\partial\emptyset\partial z}\right]\right\} \end{pmatrix}.$$

This flux is represented in a spherical, log-pressure coordinate. Prime denotes the deviation from the climatological mean basic state in which the quasi-stationary Rossby waves are embedded. $\boldsymbol{U} = (U, V)$ represents the basic state horizontal wind vector. The wave-activity fluxes are, in theory, independent of the wave phase and parallel to the local 3D group velocity. Other 3D wave-activity fluxes were also formulated by other studies (e.g., Hoskins et al., 1983; Plumb, 1986; Trenberth, 1986; Kinoshita and Sato, 2013a; 2013b).

The weakening of the stratospheric polar vortex is mainly a result of the enhanced upward planetary wave propagation from the troposphere (e.g., Polvani and Waugh, 2004). The enhancement of the upward wave propagation is induced by the anomalous wave itself and/or by an amplification of the climatological planetary waves caused by anomalous waves. Such a consideration is important in understanding the properties of the upward planetary wave propagation. Those roles can be diagnosed by the linear interference framework of the poleward eddy heat flux formulated by Nishii

et al. (2009) and other studies (Garfinkel et al., 2010; Smith and Kushner, 2012). The poleward eddy heat flux v^*T^* is a proxy for the vertical component of the E–P flux and often used as an indicator of the vertical wave propagation (Polvani and Waugh, 2004). The asterisks signify the deviations from the zonal mean (i.e., eddies). Using the expansion of the meridional wind and the temperature eddies into their climatological (denoted with a subscript "c") and anomalous (denoted with a subscript "a") components, $v^* = {v_c}^* + {v_a}^*$ and $T^* = {T_c}^* + {T_a}^*$, the observed poleward eddy heat flux can be decomposed as

$$\{v^*T^*\} = \{{v_c}^*{T_c}^*\} + \{{v_c}^*{T_a}^*\} + \{{v_a}^*{T_c}^*\} + \{{v_a}^*{T_a}^*\}.$$

The first and fourth terms on the right-hand side represent the heat fluxes due solely to the background climatological waves and anomalous waves (e.g., Rossby waves), respectively. The second and third terms represent the heat fluxes caused by the interaction between the climatological and anomalous waves. The contributions from these two terms can also be interpreted as the modulating effect of the climatological waves by anomalous waves.

The climatological heat flux can be obtained to take a climatological mean on the above equation:

$$\{v^*T^*\}_c = \{v_c{}^*T_c{}^*\} + \{v_a{}^*T_a{}^*\}_c \,.$$

Note that the term $\{v_a{}^*T_a{}^*\}_c$ represent the climatological value of the upward wave-activity associated with the anomalous waves $\{v_a{}^*T_a{}^*\}$ which tends to be spontaneously observed. An anomaly of the heat flux $\{v^*T^*\}_a$ can then be computed as a subtraction of the observed value from the climatological value:

$$\{v^*T^*\}_a = \{v_c{}^*T_a{}^*\} + \{v_a{}^*T_c{}^*\} + \{v_a{}^*T_a{}^*\}_a \,,$$

where,

$$\{v_a{}^*T_a{}^*\}_a = \{v_a{}^*T_a{}^*\} - \{v_a{}^*T_a{}^*\}_c \,.$$

The first and second terms in the right-hand side of the above equation refer to the linear terms, and the third term is a nonlinear term. The nonlinear term represents a contribution from the anomalous waves compared with its climatological value.

Following the scheme from Nishii et al. (2009) described above, we here decomposed the poleward eddy heat flux anomalies in the AFES time-slice experiments. The daily value of poleward eddy heat flux in the HICE experiment can be expressed as

$$\{v^*T^*\}_{HICE} = \{v_c{}^*T_c{}^*\} + \{v_c{}^*T^{*\prime}\} + \{v^{*\prime}T_c{}^*\} + \{v^{*\prime}T^{*\prime}\} \,,$$

where the subscript c denotes the climatological value, which is defined as the 60 year

mean of the HICE experiment for a given day, and the prime denotes the deviation from the 60 year climatology of the HICE experiment. Taking the 60 year mean, which is denoted by square brackets, gives

$$[v^*T^*]_{HICE} = [v_c{}^*T_c{}^*] + [v^{*\prime}T^{*\prime}] .$$

The observed value of the poleward eddy heat flux in the LICE experiment can be expressed as

$$\{v^*T^*\}_{LICE} = \{v_c{}^*T_c{}^*\} + \{v_c{}^*T_a{}^*\} + \{v_a{}^*T_c{}^*\} + \{v_a{}^*T_a{}^*\} ,$$

where the subscript a denotes the anomaly of the LICE value with respect to the HICE climatology. Taking the 60 year mean of the LICE value gives

$$[v^*T^*]_{LICE} = [v_c{}^*T_c{}^*] + [v_c{}^*T_a{}^*] + [v_a{}^*T_c{}^*] + [v_a{}^*T_a{}^*] .$$

Then, the poleward eddy heat flux anomaly, defined by the difference between HICE and LICE experiments, is given by

$$[v^*T^*]_a = [v_c{}^*T_a{}^*] + [v_a{}^*T_c{}^*] + [v_a{}^*T_a{}^*]_a ,$$

where

$$[v_a{}^*T_a{}^*]_a = [v_a{}^*T_a{}^*] - \left[v^{*\prime}T^{*\prime}\right] .$$

The nonlinear term represents the quadratic term arising from anomalies in eddy

components of temperature and meridional velocity in the LICE experiment as adjusted by the poleward eddy heat flux due to internal variability in the HICE experiment. Note that the results do not change much if we define the climatology “c” as an average between the HICE and LICE runs.

In the analyses of the following chapters, the 2D E–P flux (Andrews and McIntyre, 1976) and the 3D wave-activity flux by Plumb (1985) were computed from the 6 hourly atmospheric variables. The WN1 and WN2 components of the E–P flux were also computed from the respective components of the 6 hourly atmospheric variables. Note that the wavenumber decomposition was based on a Fourier transform. All these 6 hourly fluxes were converted to daily mean values for the analysis. In the case of the time-slice experiment, the daily mean atmospheric variables were used to compute the fluxes because of a limitation of the output time-interval available. The wave-activity flux formulated by Takaya and Nakamura (2001) and the poleward eddy heat flux decomposition by Nishii et al. (2009) were used only in Chapter 3; thus, the details of the computation will be described in that chapter.

	Observation			Simulation
	Analysis period	Atmospheric data	SIC data	
Chapter 3	1979/80–2014/15	JRA-55	HadISST1	Time-slice exp.
Chapter 4	1979/80–2014/15	JRA-55	HadISST2	Time-slice exp.
Chapter 5	1979/80–2016/17	JRA-55	HadISST2	Historical exp.

Table 2.1 Summary of datasets and experiments analyzed in each chapter.

	Month	Region	trend
Chapter 3	December	15°E–90°E, 70°N–85°N	Detrended
Chapter 4	November–December	15°E–90°E, 70°N–85°N	Non-detrended
Chapter 5	December	30°E–90°E, 65°N–85°N	Detrended

Table 2.2 Summary of the BKS sea ice time series used in each chapter.

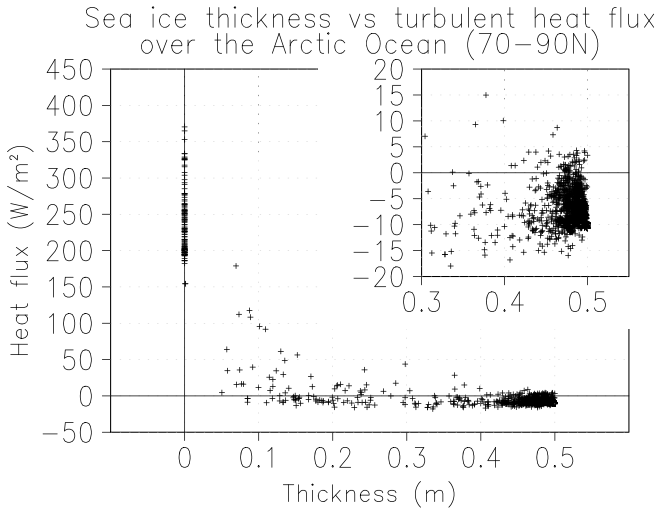

Figure 2.1 Scatter diagram showing the sea ice thickness (m) in each grid over the Arctic Ocean (northward of 70°N, excluding land) and the climatology of turbulent heat flux (W m^{-2}) (i.e., sensible and latent heat fluxes) in January. The inset in the top-right corner is an enlarged area of the plot for sea ice thickness greater than 0.3 m. The HICE run from the AFES time-slice experiment is used. (From Nakamura et al., 2015)

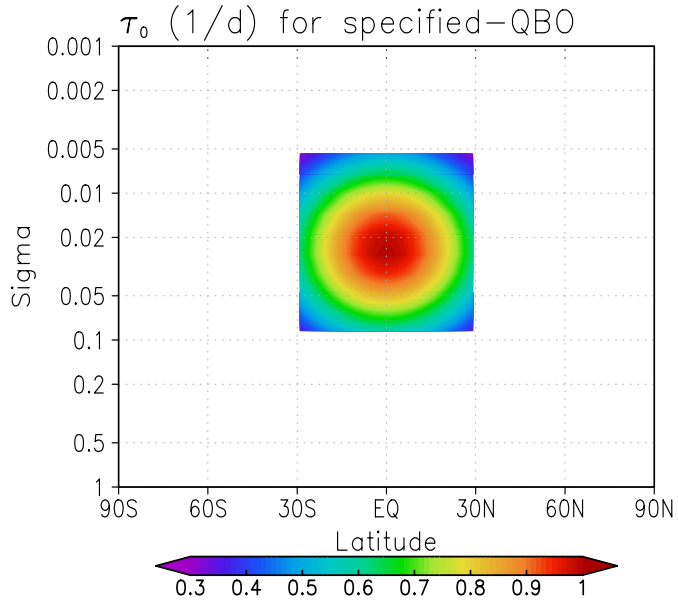

Figure 2.2 A region and intensity of nudging of zonal mean zonal winds in the AFES historical simulation. The maximum relaxation time of nudging is one day at the equator, 0.03 sigma level.

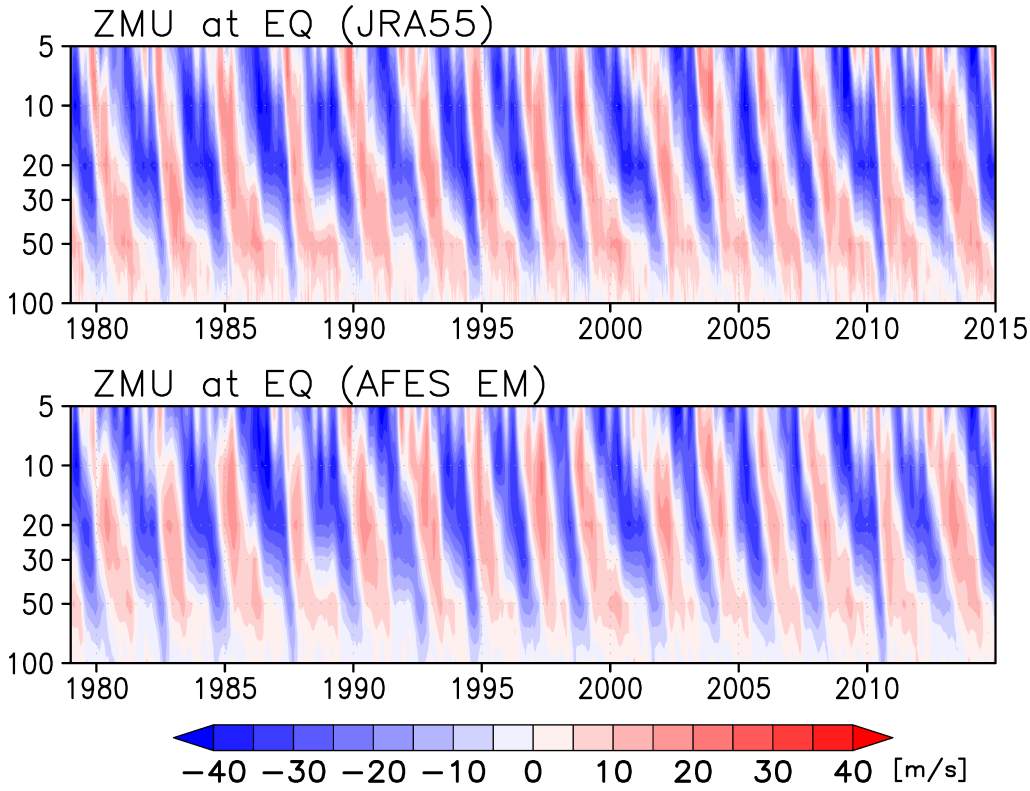

Figure 2.3 Height–time cross-section of daily zonal mean zonal wind (m s^{-1}) at the equator from (a) the JRA-55 data and (b) the 30 ensemble averaged AFES historical simulation.

Chapter 3.

Poleward Eddy Heat Flux Anomalies Associated with Recent Arctic Sea Ice Loss

3.1. Introduction

The possible relationships between rapid Arctic changes and extreme weather events in midlatitudes have also been actively studied (Cohen et al., 2014; Kug et al., 2015). Earlier work focused on the regional aspects of the Arctic–midlatitude climate linkages, such as the relationship between the fall sea ice anomalies in the Arctic and the surface winter temperature anomalies in eastern Eurasia (Honda et al., 2009). Other studies also addressed the relationships between the Arctic sea ice reduction with the meandering jet (Francis and Vavrus, 2012), as well as with the negative phases of the AO/NAO and consequent weather impacts in the Euro-Atlantic region (Overland and Wang, 2010; Hopsch et al., 2012; Jaiser et al., 2012), although the debate continues (Barnes, 2013; Screen et al., 2013; Barnes and Screen, 2015).

Lately, more attention has been given to the stratosphere–troposphere coupling

that potentially links the Arctic climate change with the midlatitude climate (Sun et al., 2015; Nakamura et al., 2016a; Wu and Smith, 2016). The key question is whether or not the Arctic sea ice anomalies sufficiently modulate the atmospheric circulation aloft so as to enhance the upward propagation of planetary waves, which is known to affect the tropospheric circulation and the surface weather (Baldwin and Dunkerton, 2001). Observational evidence that the reduction in the Arctic sea ice, especially late fall to early winter sea ice anomalies in the BKS, results in increased poleward eddy heat flux, weakening of the stratospheric polar vortex, and consequent surface impacts is emerging (Jaiser et al., 2013; García-Serrano et al., 2015; King et al., 2016; Yang et al., 2016). Numerical studies based on the AGCM have also shown evidence of the active role of the stratosphere in the Arctic–midlatitude climate linkage (Kim et al., 2014; Nakamura et al., 2015; Jaiser et al., 2016). However, there remain some questions regarding the strength of the signals relative to natural variability (Mori et al., 2014), nonlinear atmospheric circulation responses to the different forcing regions in projected climate conditions (Sun et al., 2015), and the combined influence of sea ice, snow cover, and SST forcings (Cohen et al., 2014). Moreover, previous studies have not examined detailed characteristics of upward planetary wave propagation that drives the stratosphere–troposphere coupling and relationships between the increased poleward

eddy heat fluxes and the 3D atmospheric structure.

This chapter aims to better understand the processes of the upward planetary wave propagation associated with the reduction in the Arctic sea ice. We investigate the detailed atmospheric 3D structures that induce the heat flux anomalies by employing the linear decomposition scheme of Nishii et al. (2009) for the poleward eddy heat flux anomalies and examining the individual temperature and meridional velocity fields separately. Combining this linear decomposition scheme with the 3D wave-activity flux diagnosis, we also clarify a 3D structure of the upward propagating planetary waves and a source region that reinforces the anomalous wave propagation under the recent sea ice loss condition.

3.2. Data and Methodology

HadISST1 and JRA-55 were used for the 1979/1980–2014/2015 period (Table 2.1). For JRA-55, we first computed the daily average from the 6 hourly data. The atmospheric variables were then linearly regressed on a time series of the normalized December SIC averaged over the BKS (15°E–90°E, 70°N–85°N; Table 2.2) after both the reanalysis data and the SIC index were detrended. The sign of the regression

coefficients was reversed to focus on the atmospheric response to a reduced state of the Arctic sea ice. Figure 3.1 shows the SIC time series and an associated SIC anomaly pattern.

We also used the AFES time-slice experiment (see Section 2.2 for further details of the experiment). The anomalies were defined by subtracting HCIE from the LICE runs, thereby representing the anomalous atmospheric conditions associated solely with the reduction in the Northern Hemisphere sea ice. Figure 3.2 shows the differences of the SIC between the HICE (1979–1983) and LICE (2004–2009) periods from the HadISST1 data. The companion paper (Jaiser et al., 2016) showed a high degree of consistency between the AFES simulation results and the ERA-Interim reanalysis data in terms of the general characteristics of the stratosphere–troposphere coupling. We specifically focus on the changes in the poleward eddy heat flux by a more detailed approach applied to the JRA-55 reanalysis data and the simulation result.

The poleward eddy heat flux is a key indicator of the upward propagation of the planetary waves because it is proportional to the vertical component of the E–P flux. We calculated the daily poleward eddy heat flux for both the reanalysis data and the simulation results after an 11-day running mean was applied to the daily temperature and meridional wind data. Daily anomalies were computed using daily climatological

values, which are the 36-year mean of the reanalysis data in the observation and the 60-year mean of the HICE run in the simulations. Then, we decomposed the poleward eddy heat flux anomalies as described in Section 2.3. In the analysis of the reanalysis data, the decomposed heat flux anomalies were regressed on the sea ice time series. For the AGCM time-slice experiments, the decomposed values of the 60 year averaged heat flux anomaly were analyzed. The linear terms in temperature anomaly and in meridional wind anomaly were here referred to as LTa and LVa, respectively, and the nonlinear term was referred to as NL.

In the evaluation of the wave-activity flux formulated by Takaya and Nakamura (2001) (see details for Section 2.3), the perturbation quantities were taken from the differences between the LICE and HICE runs for the simulation and from the linear regression coefficients of the JRA-55 on the SIC time series for the observation. The mean flow was taken from the 60-year averaged HICE value for the simulation and from the 36-year climatological mean for the observation. The statistical significance was evaluated using the two-sided Student's t test.

3.3. Results and Discussion

3.3.1. Intra-seasonal Tropospheric Responses

We first examined an intra-seasonal progression of the tropospheric anomalies associated with the sea ice loss in the BKS (Figure 3.3). Significant cold temperature anomalies existed over the central Eurasia in December. The wave-activity fluxes formulated by Takaya and Nakamura (2001) indicated that the quasi-stationary Rossby waves propagated from the anticyclonic anomalies over the BKS toward the cyclonic anomalies over eastern Eurasia at the upper tropospheric level. The corresponding surface anticyclonic anomalies shifted downstream-ward by about a quarter wave length relative to the upper tropospheric wave pattern, and the associated anomalous north-westerly winds caused cold air advection toward central Eurasia. These features were consistent with the quasi-stationary Rossby wave responses to the sea ice loss in the BKS, as discussed in the previous studies (Honda et al., 1999; 2009; Nakamura et al., 2015). There are no significant anomalies in the temperature and tropospheric circulation fields in January. In February, the circulation anomalies were characterized by the negative phase of the AO/NAO-like pattern for both the sea level pressure (SLP) and the upper tropospheric geopotential height fields, although related cold anomalies over northern Europe and North America are less statistically significant. From those

analyses, different features were identified between early and late winters.

Those features were supported by the simulation results (Figure 3.4). In the early winter (i.e., in January), the quasi-stationary Rossby wave-like signals over Eurasia were found at 250 hPa, and surface anticyclonic and negative temperature anomalies were observed over central-to-eastern Eurasia. In the late winter (i.e., February), the negative phase of the AO/NAO-like anomalies appeared in both the upper and lower troposphere with the significant cold anomalies over Europe and eastern North America. The consistency between the reanalysis and AGCM results strongly supported the notion that the tropospheric responses to the sea ice loss are different between early and late winters. Additionally, we can speculate that the negative AO/NAO-like anomalies in the late winter are related to the stratospheric pathway, as pointed out by the previous studies (Kim et al., 2014; Sun et al., 2015; King et al., 2016).

3.3.2. Wave–Mean Flow Interaction

Figures 3.5a and b show the time evolution of the JRA-55 daily mean anomalies of the zonal mean zonal wind at 60°N and the poleward eddy heat flux averaged over 50–80°N at 100 hPa, respectively. Note that the 100 hPa level was used to represent the

strength of the upward planetary wave propagation (Polvani and Waugh, 2004). The negative zonal wind anomalies first appeared in the upper stratosphere in early January, and signals subsequently propagate downward to the surface level in February. An increase in the poleward eddy heat flux in December and January preceded the polar vortex weakening. When we compare these results with the AGCM results, there is a striking resemblance in features, such as the increased poleward eddy heat flux in late December and January (Figure 3.5e) and the weakened stratospheric polar vortex and subsequent downward propagating signal (Figure 3.5d). Those results strongly suggest the role of the stratospheric pathway on the formulation of the tropospheric negative AO/NAO anomalies in the late winter (Figures 3.3 and 3.4). Quantitatively, the increase in the simulated poleward eddy heat flux averaged over January was approximately 19% of its climatological (HICE) value.

We then examined the horizontal distributions of the poleward eddy heat fluxes and discussed whether or not there are any preferred locations for the enhanced poleward eddy heat flux. There are indeed two centers of action in the poleward eddy heat flux climatology at the 100 hPa level (purple contours in Figures 3.5c and f). One was situated near the BKS, while the other was over the Bering region, appearing consistently in both JRA-55 and simulation results. Note that we used slightly different

periods for the time averaging in each case (December for JRA-55 and January for the simulations), which reflected the difference in their respective peak periods of the poleward eddy heat flux anomalies. January was chosen straightforwardly for the simulations. The result of the reanalysis data had two peaks, December and January. We chose December as the analysis period because no statistically significant region of the heat flux anomaly appeared in the January horizontal map (black contour, Figure 3.6a). Moreover, no significant circulation anomaly was found in the troposphere (Figure 3.3). The results did not change much when we chose the December–January mean for the analysis period (see Figure 3.6b for the horizontal map of the poleward eddy heat flux anomalies).

The poleward eddy heat flux anomalies at 100 hPa from the reanalysis (Figure 3.5c) and from the simulations (Figure 3.5f) are also shown (indicated by shading). For both results, the positive poleward eddy heat flux anomalies appeared in eastern Eurasia and its vicinity (herein referred to as the eastern Eurasia (EE) region), representing an enhancement of the climatological heat fluxes. In addition, another area was located approximately south of the BKS (herein referred to as the central Eurasia (CE) region) with significant positive poleward eddy heat flux anomalies. This is part of a dipole pattern with an area of negative flux anomalies situated to the west. Comparing the

location of this dipole pattern with respect to the climatological center, the reduction in the Arctic sea ice leads to a shift and strengthening of the region of the positive poleward eddy heat flux in CE at the lower stratospheric level.

3.3.3. Term-wise Decomposition

Next, we analyzed the poleward eddy heat flux anomalies in CE and EE by applying the decomposition scheme proposed by Nishii et al. (2009). Figures 3.7 show the maps of the linear and nonlinear terms that contributed to the poleward eddy heat flux anomalies at 100 hPa in December from the reanalysis and January from the model simulations. For the EE region (50–80°N, 140°E–160°W; marked in Figure 3.7a), the dominant contributor was LTa for both the reanalysis and simulation results (Figures 3.7a and d). The LTa term made up 60% and 57% of the poleward eddy heat flux anomalies over the EE region for the December mean reanalysis results and January mean simulation results, respectively (Table 3.1). The LVa term results (Figures 3.7b and e) also show a dipole pattern with a positive anomaly over the CE region with a paired negative anomaly to the west, as discussed earlier. The major contribution to the

poleward eddy heat flux anomaly over the CE region (50–80°N, 50–90°E; marked in Figure 3.7b) was by the LVa term. The contributions from the LTa term were 61% and 66%, for the reanalysis and simulation results, respectively (Table 3.1). The percentage-wise contributions of the LTa and LVa terms showed highly consistent results between the reanalysis and simulations.

3.3.4. Coupling Between Temperature and Wind Fields

Recognizing the importance of the LTa and LVa terms to the 100 hPa poleward eddy heat flux anomalies in the EE and CE regions, respectively, we took a step further to examine how the temperature and the meridional wind fields are coupled to produce the resulting LTa and LVa patterns. We first considered the reanalysis results. Note that the climatological temperature field had a clear WN1 pattern (Figure 3.8b, shading). The climatological meridional wind field had a negative anomaly over central Eurasia and a positive anomaly over eastern Siberia (Figure 3.8a, contours). They together constitute a climatological trough over Siberia at this level. The positive anomalies in the poleward eddy heat flux in the EE region were seen as a result of the coupling of the climatological southerly wind (Figure 3.8a, contours) with the positive temperature

anomalies (red shading in Figure 3.8a). In the CE region, the eddy heat flux anomalies in Figure 3.5c were part of a dipole pattern over around the BKS. Similar dipole patterns were found both in LVa (Figure 3.7b, shading) and in the meridional wind anomalies (Figure 3.8b, contours). These consistently present dipole patterns revealed that the increase in the poleward eddy heat flux in the CE region arose from coupling between the negative meridional (northerly) wind anomalies and the negative temperatures that are part of the climatological WN1 pattern (Figure 3.8b, shading).

The corresponding results from the simulation were generally in good agreement with those from the reanalysis. For example, the WN1 pattern in the climatological temperature field was clearly visible (Figure 3.8d, shading). The climatological meridional wind field was consistent between the JRA-55 and AGCM results, although the latter showed a weaker negative anomaly centered over Siberia (Figure 3.8c, contours). In the EE region, a positive temperature anomaly (Figure 3.8c, shading) coupled to the climatological southerly wind (Figure 3.8c, contours) induced an increase in the poleward eddy heat flux. In the CE region, similar to the reanalysis, the dipole in the meridional wind anomalies (positive over Scandinavia and negative over CE in Figure 3.8d, contours) was superimposed on the negative temperature region that is part of the climatological WN1 temperature field (Figure 3.8d, shading). However,

differences were found between the JRA-55 data and model results, especially in the anomalous temperatures and meridional winds over northeastern Canada and the North Atlantic, respectively, which require further examination. Nonetheless, the spatial characteristics of the meridional wind and temperature fields over the CE and EE regions were remarkably consistent between JRA-55 and the model results.

3.3.5. Synthesis

The abovementioned analysis revealed in a systematic way how the coupling of temperature and meridional wind leads to increases in the poleward eddy heat fluxes at the 100 hPa level in the CE and EE regions, as represented by the linear terms. Whether or not the meridional wind and temperature anomalies in these two regions at the lower stratospheric level are dynamically linked with the surface sea ice variability must be established, and the processes responsible must be identified. Figure 3.9a captures the basic features of the atmospheric teleconnection associated with the sea ice reduction. Over the BKS sector (approximately 30°E–90°E), the positive anomalies of temperature (shading, marked by A) and those of the geopotential height (contour, marked by B) appeared in the troposphere as a result of the increased surface turbulent heating

associated with the sea ice loss (Figure 3.1). At the 250 hPa level (Figure 3.3), the quasi-stationary Rossby waves propagated from the anticyclonic anomalies over the BKS toward the cyclonic anomalies over Eurasia. Figure 3.9a further indicates the upward propagation of the Rossby waves into a region of positive height anomaly in the stratosphere (contour, marked by E). Along this path, a wave train appeared to be composed of two positive geopotential height anomalies: one over the BKS sector in the troposphere that extends to the lower stratosphere, and the other over the longitudinal sector that includes the EE region in the stratosphere with a negative geopotential height anomaly in between (marked by C).

The positive geopotential height anomalies marked by B were consistent with the dipole in the anomalous meridional wind field in the CE region at 100 hPa (Figure 3.8b). The stratospheric positive temperature anomaly (marked by D) with a westward tilting structure and a quarter wavelength shift with respect to the positive height anomaly (marked by E) was also consistent with the horizontal pattern of the temperature anomalies in the EE region at 100 hPa (Figure 3.8a). The simulation results showed a good agreement with the JRA-55 results in terms of the spatial characteristics of the temperature and the geopotential height anomalies, although the details were somewhat different (e.g., negative temperature anomalies in the upper stratosphere and positive

geopotential height anomalies in the Western Hemisphere) (Figure 3.9b). In the model experiments, the upward component of the wave-activity flux was nearly absent in the troposphere, except over the BKS region (Figure 3.9b), even if we prescribe the sea ice anomalies over the entire Northern Hemisphere. The results strongly suggest that the stationary Rossby wave propagation from the BKS region is a major driver of the meridional wind and temperature anomalies and associated increases in the poleward eddy heat fluxes in the CE and EE regions at the lower stratospheric level.

Figures 3.9c and d clearly show that the deviations from the respective zonal mean averages of the geopotential height anomalies at 100 hPa and 60°N both in observed atmospheric variability that was linearly related to the December BKS SIC and the simulation results modulate the wave structure in the lower stratosphere in such a way that a climatological trough over Siberia (around 120°E) was deepened through the quasi-stationary Rossby wave propagation. Thus, the results showed a constructive linear wave interference on the planetary wavefield (e.g., Fletcher and Kushner, 2011; Smith and Kushner, 2012), which arose from the Arctic sea ice loss under the present climate conditions (see the discussion in Sun et al. (2015) in the context of future sea ice loss). Note that the surface disturbance from a rather small region of the BKS resulted in a planetary-scale modulation of the stratospheric wave structure.

3.4. Summary

Similar intra-seasonal progression of the atmospheric responses to the sea ice loss was identified from the analyses of the reanalysis and AGCM simulation results. Early winter was characterized by the Eurasian cold anomalies with the quasi-stationary Rossby wave responses to the BKS sea ice loss, whereas the negative phase of the AO/NAO-like circulation anomalies was seen in late winter (Figures 3.3–3.4). The tropospheric AO/NAO anomalies were formulated in association with the downward influences of the weakened stratospheric zonal winds (Figures 3.5a and d). These features were consistent with the results of recent studies (Kim et al., 2014; King et al., 2016).

Toward a better understanding of the processes regarding the upward planetary wave propagation that weakens stratospheric zonal winds, we investigated herein how the spatial and temporal characteristics of the poleward eddy heat flux were modulated in response to the reduction in the Arctic sea ice. The poleward eddy heat fluxes at the lower stratospheric level increased in the CE and EE regions (Figures 3.5c and f). These increases were caused by the constructive coupling of the climatological planetary wave

structure with the anomalous meridional wind and temperature fields, respectively (Figures 3.7–3.8), which were dynamically linked through the propagation of the stationary Rossby waves emanating from the BKS region (Figure 3.9).

Previous studies examined and characterized anomalous poleward eddy heat fluxes in the northern high latitudes in conjunction with different stratospheric conditions, e.g., with AO and the vortex strength (Polvani and Waugh, 2004; Garfinkel et al., 2010) or with stratospheric sudden warming events (Nishii et al., 2009). In comparison, this study provided a detailed 3D picture of the way the recent BKS sea ice loss modified the poleward eddy heat flux field in the lower stratosphere and subsequently affected the stratospheric wave structure, which likely plays a key role in the Arctic–midlatitude climate linkages under the present climate conditions.

	$[v_c^* T_a^*]$	$[v_a^* T_c^*]$	$[v_a^* T_a^*]_a$
EE	60.4/56.6	32.4/28.3	7.2/15.1
CE	22.2/5.6	60.9/66.2	16.9/28.2

Table 3.1 Contributions (%) from the three decomposed terms (LVa, LTa, and NL) to the total poleward eddy heat flux anomalies over the CE and EE regions, for the December mean reanalysis results (right) and the January mean simulation results (right).

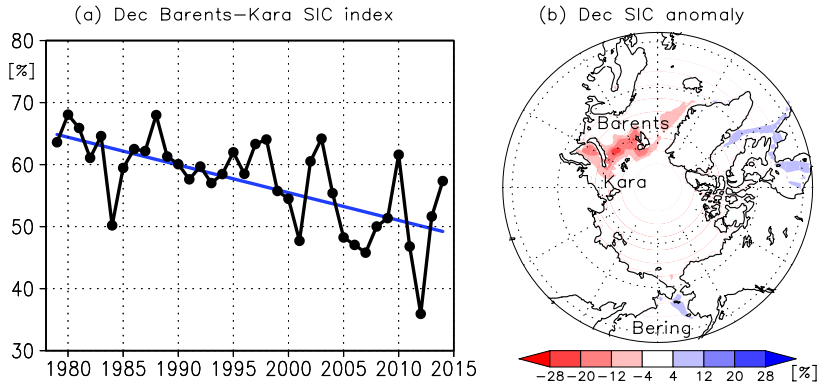

Figure 3.1 (a) Time series of the December SIC (%) averaged over the BKS (15°E–90°E, 70°N–85°N). Blue line indicates the linear trend. (b) December SIC anomalies (shading) regressed on the normalized December BKS SIC index. Both data are detrended, and all data are from HadISST1.

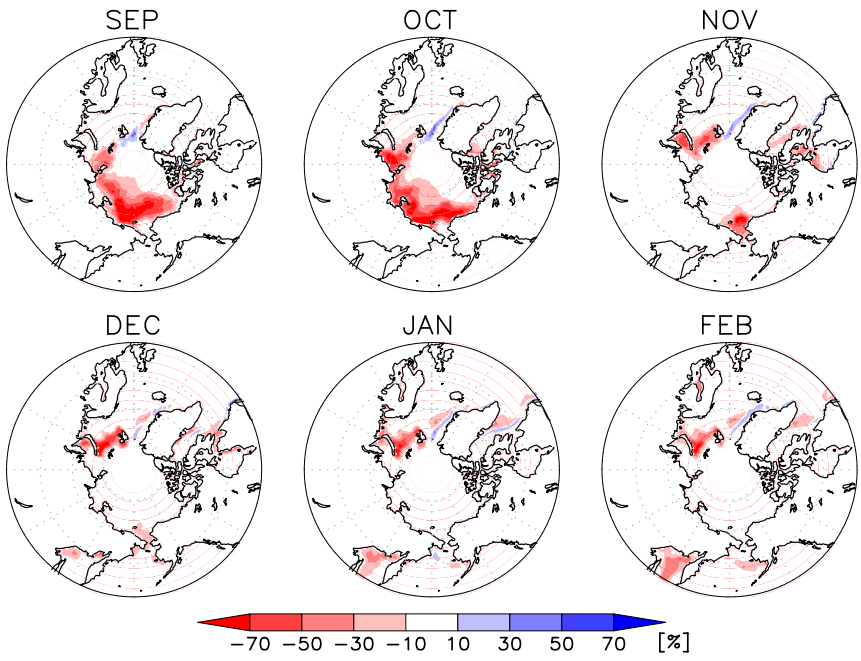

Figure 3.2 Observed monthly averaged SIC (%) differences between the LICE (2005–2009) and HICE (1979–1983) periods from HadISST1.

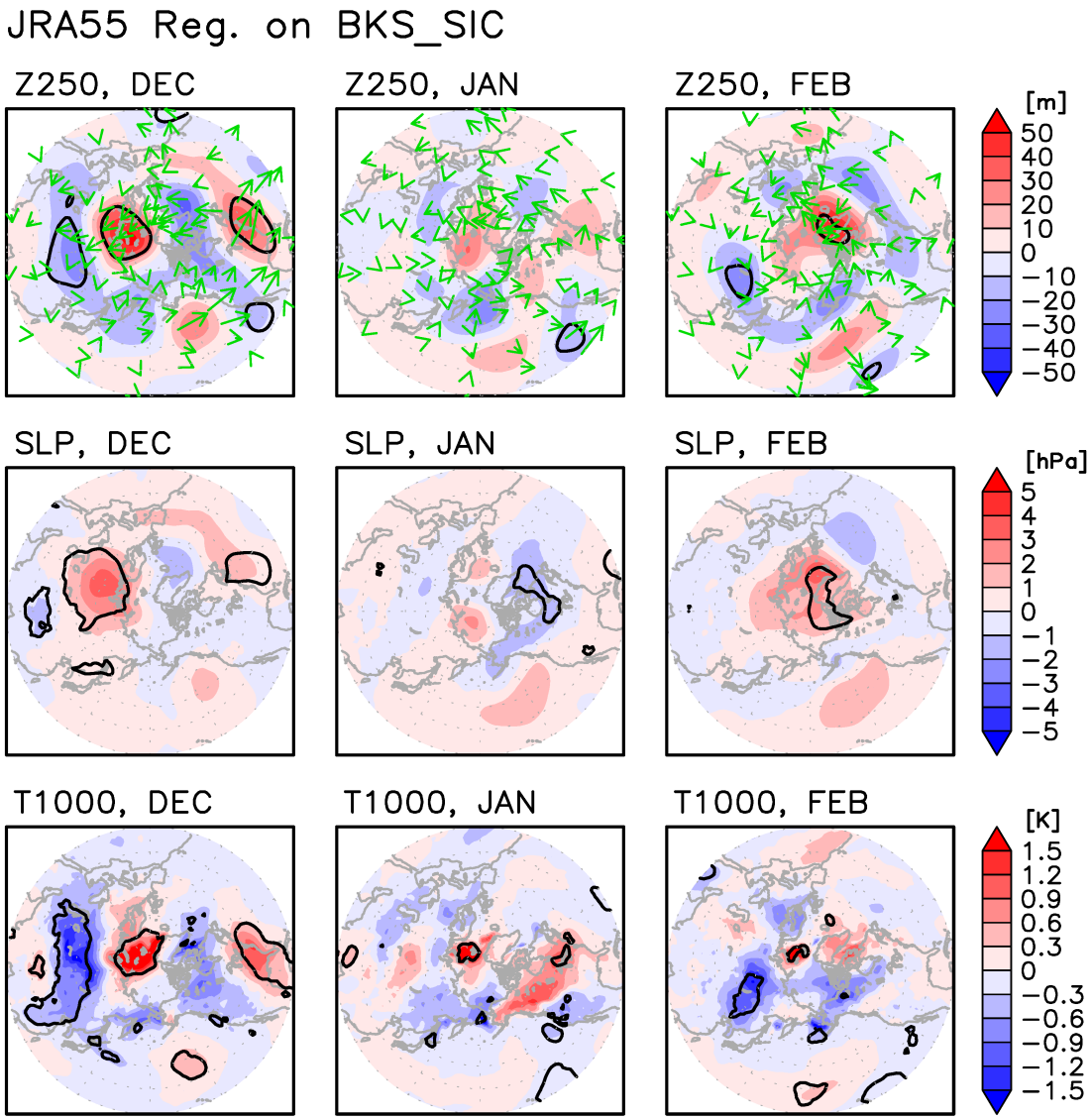

Figure 3.3 The JRA-55 anomalies of detrended (upper) geopotential height at 250 hPa, (middle) SLP, and (lower) temperature at 1000 hPa for (left) December, (middle) January, and (right) February for 1979/1980–2014/2015; these regressed on the normalized December BKS SIC index are also shown. Note that the sign of the coefficients is reversed. The solid

line indicates regions with statistical significance at the 95% level. The arrows in the upper panels indicate the horizontal components of wave-activity flux ($m^2\ s^{-2}$) formulated by Takaya and Nakamura (2001).

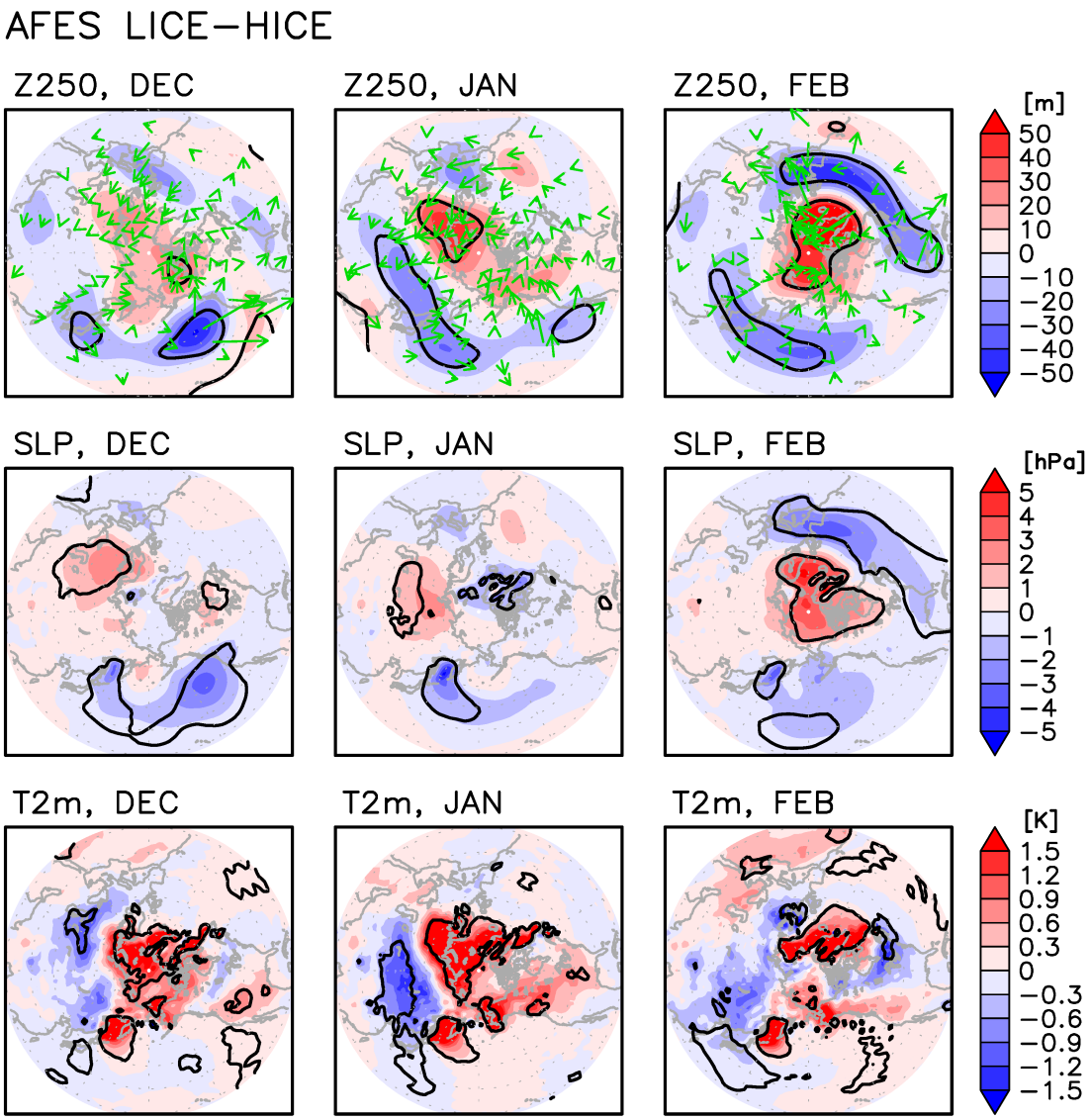

Figure 3.4 Model differences (LICE–HICE) in (upper) geopotential height at 250 hPa (Z250; m), (middle) sea level pressure (SLP; hPa), and (lower) 2 m temperature (T2m; K) for (left) December, (middle) January, and (right) February. The solid line indicates 95% statistical significance. The arrows in the upper panels indicate the horizontal components of wave-activity

flux (m^2 s^{-2}) formulated by Takaya and Nakamura (2001).

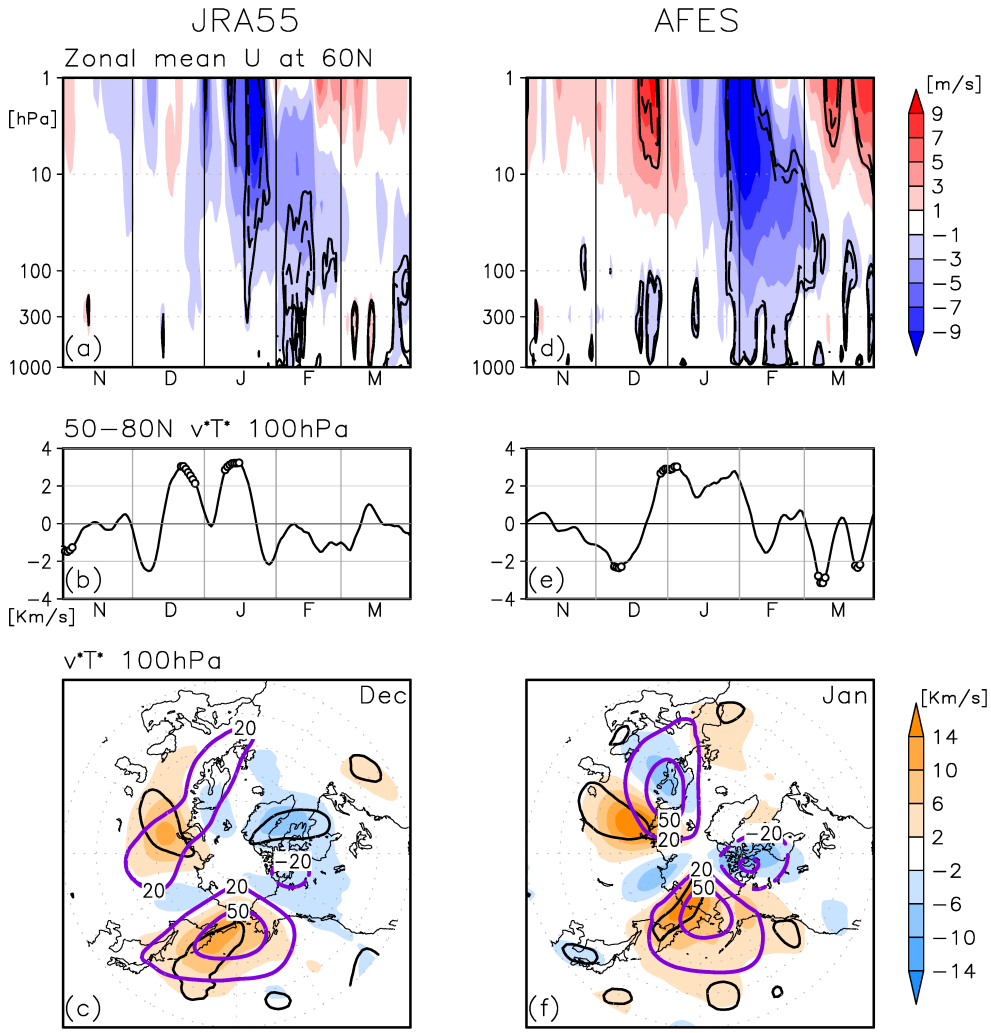

Figure 3.5 Anomalies in (a, d) a time–height cross-section of zonal mean zonal wind at 60°N (shading; m s^{-1}) and (b, e) a time series of 50°N–80°N mean poleward eddy heat flux at 100 hPa (K m s^{-1}), for the model (left) and the reanalysis data (right). Anomalies (shading) and climatology (purple contours) of poleward eddy heat flux at 100 hPa for the (c) December

mean value in the reanalysis data and (f) January mean value in the model. The solid (dashed) black lines in Figures 3.5a and 3.5d indicate statistical significance at the 90% (95%) level. The circles in Figures 3.5b and 3.5e and black lines in Figures 3.5c and 3.5f indicate statistical significance at the 95% level.

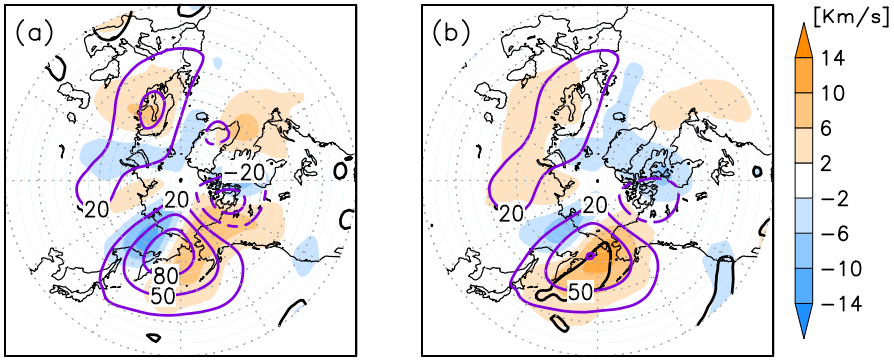

Figure 3.6 Same as Figure 3.5c, except for (a) the January period and (b) the December–January period over which the poleward eddy heat flux is averaged.

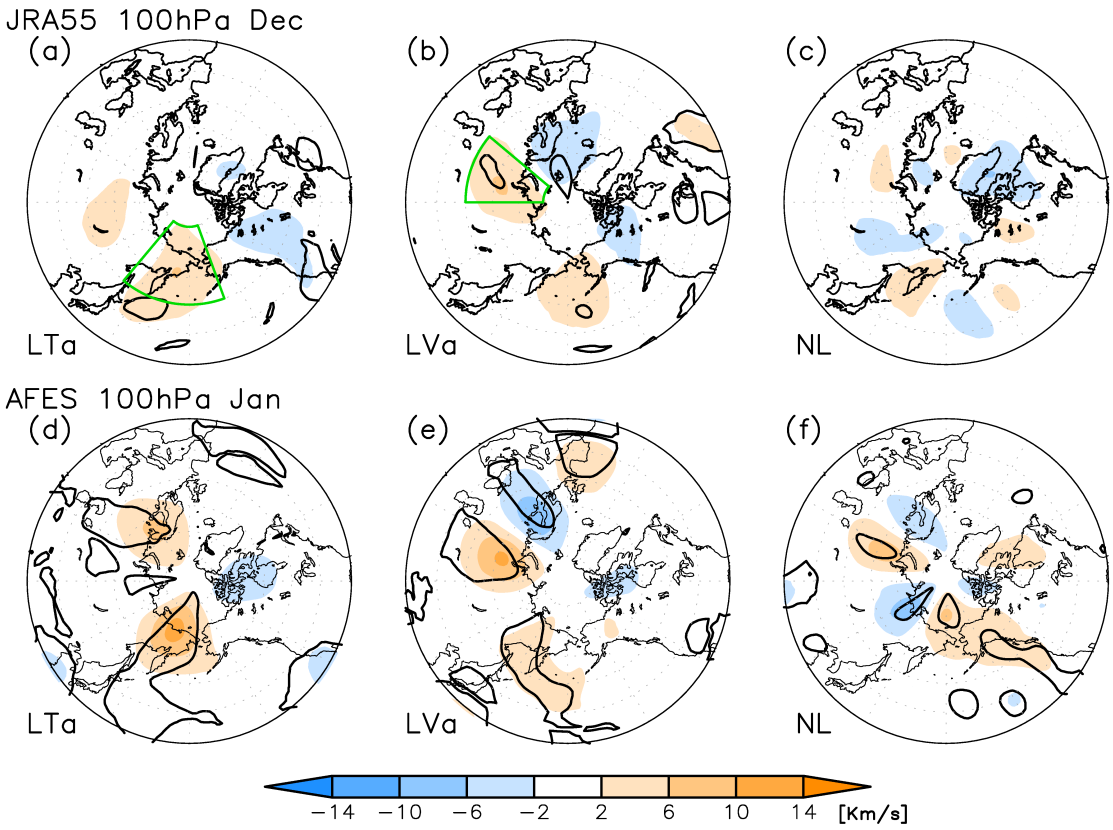

Figure 3.7 Decomposed poleward eddy heat flux anomalies (K m s^{-1}), (a, d) LTa, (b, e) LVa, and (c, f) NL terms at 100 hPa, for (upper) the December mean reanalysis results and (lower) the January mean simulation results. The green boxes in Figures 3.7a and 3.7b indicate eastern Eurasia (140°E–160°W, 50°N–80°N) and central Eurasia (50°E–90°E, 50°N–80°N) regions, respectively. The black contours indicate 95% statistical significance.

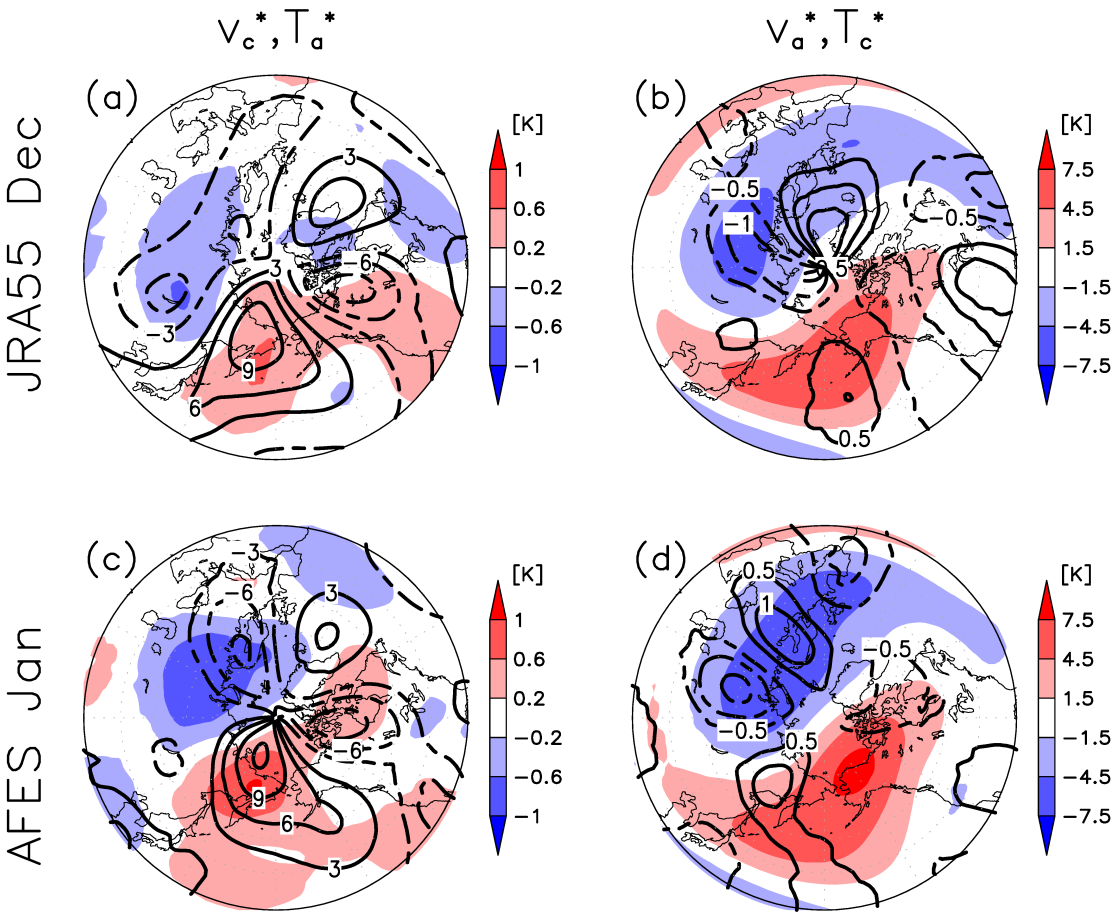

Figure 3.8 (a and c) Climatological meridional wind (contours; m s^{-1}) and anomalous temperature (shading; K) and (b and d) anomalous meridional wind (contours; m s^{-1}) and climatological temperature (shading; K) at 100 hPa from (a and b) December averaged reanalysis data and (c and d) January averaged model results.

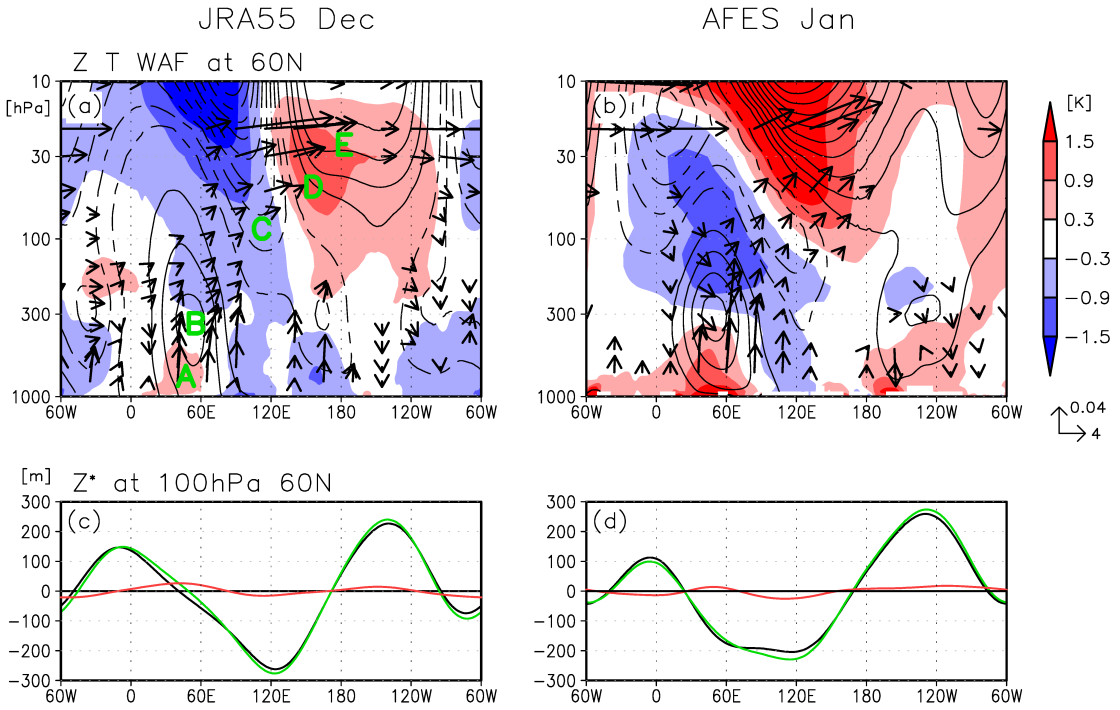

Figure 3.9 Longitude–height cross-section at 60°N of temperature anomaly (shading; K) and geopotential height anomaly (contours; m), from (a) reanalysis data and (b) simulation results. The black lines are drawn for every 10 m, and the dashed lines indicate negative values. The 0 lines are omitted. The arrows indicate the zonal and vertical components of wave-activity flux (m^2 s^{-2}), as defined by Takaya and Nakamura (2001). The vectors are scaled by the reciprocal square root of the density, and the small vectors are not plotted. Geopotential height anomalies at 60°N from the respective zonal means (d) of climatology (black), with regression coefficients

associated with 1 standard deviation of the December averaged BKS SIC index (red) and their sum (green), and (c) of HICE (black), LICE (green), and LICE–HICE (red).

Chapter 4.

Weak Stratospheric Polar Vortex Events Modulated by the Arctic Sea Ice Loss

4.1. Introduction

A rapid weakening of the polar vortex over a matter of several days can occur in the boreal winter stratosphere in association with the raise in the stratospheric polar cap temperature (Schoeberl, 1978; Limpasuvan et al., 2004). This event is known as an SSW, which results from a significantly enhanced upward propagation of the planetary waves from the troposphere and the interaction of these planetary waves with the zonally averaged circulation (Charney and Drazin, 1961; Matsuno, 1971). Stratospheric signals may descend and lead to significant circulation anomalies in the troposphere and associated weather and climate variations (Baldwin and Dunkerton, 2001; Polvani and Waugh, 2004); hence, SSWs may be one of the factors contributing to midlatitude cold trends in recent years. Additionally, considering the significant influences of the Arctic sea ice loss on the mean state polar vortex variations, we postulate that the Arctic sea ice

anomalies in the recent years were a factor that modulates SSW events.

Previous studies have investigated factors that control the upward propagation of the planetary waves during SSW events and processes that anomalous stratospheric signals descend to the troposphere. A significant upward planetary wave propagation is composed mostly of WN1 and WN2 components, and the wave propagation tends to occur in association with an emergence of tropospheric blocking highs (Quiroz, 1986; Woollings et al., 2010). Blocking highs over the Atlantic sector precede the upward planetary wave propagation from the WN1 component; thus, displacement-type SSWs tend to occur. On the contrary, blocking highs over eastern Europe or the eastern Pacific precede the WN2 upward propagation and split-type SSWs (Martius et al., 2009; Castanheira and Barripedro, 2010; Nishii et al., 2011). The upward planetary wave propagation is also modulated by ENSO. The significant WN1 upward propagation and displacement-type SSW are frequently observed during El Niño winters, whereas the WN2 upward propagation and split-type SSW are relatively frequently observed during La Niña winters (Taguchi and Hartmann, 2006; Barriopedro and Calvo, 2014; Song and Son, 2018). The QBO is likely another factor controlling the direction and strength of the planetary wave propagation leading to a more frequent SSW occurrence during the easterly phase compared to the westerly phase (Labitzke, 1982). The combined

influences of ENSO and QBO on SSWs were also discussed based on the reanalysis data (Taguchi, 2015) and numerical simulation (Richter et al., 2011).

We postulated herein that the Arctic sea ice anomalies in the recent years were another forcing factor for the SSW events. However, directly testing such a conjecture based on the reanalysis data is rather difficult because of the small number of SSW events and the presence of its decadal variability (e.g., Palmeiro et al., 2015). As a first step toward understanding the potential relationship between the sea ice variability and the SSWs, we assessed whether or not the sea ice loss in the BKS modulates the characteristics of the weak polar vortex (WPV) events defined as those including not only SSWs, but also those with less intense polar vortex disturbances. We particularly examined how the BKS sea ice loss contributes to the modulation of each zonal wavenumber component in the planetary scale and the spatial structures of significant upward wave propagation. We also examined the characteristics of the stratosphere–troposphere vertical coupling that influences the surface weather.

4.2. Data and Methods

We analyzed JRA-55 and HadISST2 in the period from 1979/1980 to 2014/2015,

thereby covering 36 boreal winter seasons (Table 2.1). We sampled WPV events occurring during the winter season (December to February; DJF) because this was the season during which the sea ice anomalies enhance the upward planetary wave propagation the most. We sampled the WPV events using the daily Northern Annular Mode (NAM; Thompson and Wallace, 2000) index, which is the leading principal component time series of the 10 hPa geopotential height northward 20°N during mid-winter (DJF) using the empirical orthogonal function (see Butler et al. (2015) for a more detailed discussion on various criteria for SSW). Our criterion for choosing the WPV events was that the NAM index becomes less than −1σ. This date is referred to as Day 0. After the polar vortex is stabilized (the NAM index rose above −1.0σ), we skipped 3 weeks to search for the next WPV event. This criterion allowed us to sample 33 WPV events, including 21 SSW events. Note that the SSWs were defined by a 10 hPa zonal mean zonal wind reversal at 60°N based on Charlton and Polvani (2007). The SSW events that occurred within a 15-day difference from an onset date of the WPV events were here counted. The gray bar graph in Figure 4.1a shows the number of WPVs that occurred in each winter from 1979/1980 to 2014/2015, while the black bars indicate the number of SSWs.

Next, we categorized the WPV events into heavy- or light-ice WPVs based on

the November–December mean SIC averaged over the BKS (15°E–90°E, 70°N–85°N, indicated by the green box in Figure 4.2a) (Table 2.2). We categorized the following winters into the heavy- and light-ice winters when the SIC value exceeded plus or minus 0.5 standard deviation during the 36-year period. The time series and the blue and red marks in Figure 4.1b indicate the SIC index and the heavy- and light-ice winters, respectively. Figures 4.2a and b show the DJF mean SIC anomalies (differences from the climatology) averaged over the heavy- and light-ice winters that have WPVs, respectively. After applying this sea ice criterion to 33 initially sampled WPV events, we obtained 17 heavy- and 9 light-ice WPV events, of which 9 and 7 were SSW events. We then performed a composite analysis for both the heavy- and light-ice WPV events centered at Day 0. The following sections will show the composite averages of the anomalous fields. We calculated the daily climatological atmospheric values by applying a 31-day running average to the 36-year averaged daily values, from which the daily anomalies were calculated as deviations. The statistical significance of the composite anomalies was estimated using the two-sided Student's t test with the null hypothesis of no anomalies.

Because of an accelerated downward trend of the SIC starting at approximately 2000–2005 (Figure 4.1b), the results of our composite analysis may not only reflect the

variability of the WPVs/SSWs related to the sea ice changes, but also contain additional compounded influences from, for example, increases in greenhouse gases. We conducted two additional analyses to reduce these possible influences. One approach used linearly detrended data for both the SIC index and atmospheric variables. Another one repeated the whole composite analysis based on a shorter time period (1979/1980 to 2004/2005), during which a linear trend in the BKS sea ice time series was very weak or almost absent. When we linearly detrended the BKS sea ice time series, the heavy-ice composite consisted of winters in the middle period (i.e., the 1990s in which only a few SSWs occurred), whereas the light-ice composite consisted of winters mostly in the early and recent periods (i.e., 1980s and years after 2005 in which the SSWs frequently occurred). Consequently, the simple detrending approach for the full period may emphasize the decadal behavior of the SSW events (Palmeiro et al., 2015). The shorter period did not suffer from such a strong decadal behavior (Figure 4.1c); therefore, we added our analysis on the shorter period to check the robustness of the results and only briefly discussed the alternative linearly detrending approach. We also analyzed a result of the AFES time-slice experiment to support the observation results (HICE and LICE runs; see Section 2.2 for details).

4.3. Results

4.3.1. Wave–Mean Flow Interaction

Figure 4.3 shows the time evolutions of the zonal mean zonal wind anomaly at 60°N (top), the vertical E–P flux anomaly averaged over 40°N–80°N at 100 hPa (middle), and the 2 m temperature anomaly averaged over the midlatitude (50°N–70°N) land region (bottom) for the heavy- and light-ice WPV composites. Both composites showed weakened zonal mean zonal winds in the upper stratosphere from around Day −5 and descending weakened zonal wind signals (Figures 4.3a and b) in association with the increased total E–P fluxes from days −10 to +10 (indicated by black lines in Figures 4.3c and d). These results were consistent with the general features of the WPV/SSW events described in the previous studies (Polvani and Waugh, 2004; Limpasuvan et al., 2004).

However, marked differences were found between the two composites. The stratospheric negative zonal wind anomaly and the positive total E–P flux anomaly in the light-ice composite were both larger than those in the heavy-ice composite. In the wavenumber structure of the E–P flux anomalies, the WN1 component was dominated in the heavy-ice composite from days −10 to +5 (Figures 4.3c), whereas the light-ice

composite showed larger positive WN2 anomalies than the WN1 anomalies before Day 0 (Figure 4.3d). Marked differences were also found in the stratosphere–troposphere vertical coupling. The negative wind anomalies in the light-ice composites appeared at almost the same timing in both the stratosphere and the troposphere (just before Day 0). The tropospheric wind signals were prolonged for more than 30 days, and the surface temperature over the midlatitude land region decreased by 1–2 K (black line in Figure 4.3f) after the onset of the WPV events. This temperature decrease stood out in the Eurasian continent (0°E–180°E, indicated by the blue line).

Two factors may account for this stronger stratosphere–troposphere coupling in the light-ice WPV events. One is the strength of the sampled WPV events. The light-ice composite had a higher rate of SSW events (7 out of 9) than the heavy-ice composite (9 out of 17); thus, the stratospheric influence was stronger. However, from the observations, it is difficult to see if the higher rate results from the lower sea ice conditions or from the decadal variability of the SSW events (e.g., winters in the 1980s and after 2000 had more frequent SSW events than those in the 1990s; Palmeiro et al., 2015). Furthermore, the rates of the SSW to the WPV depended on the SSW definitions. If we define the SSWs as a reversal of the 10 hPa zonal wind averaged northward of 60°N (Butler et al., 2015), the difference in the rates between the heavy- (14 out of 17)

and light-ice (7 out of 9) winters becomes smaller.

Another explanation for the stronger coupling is the modification of the characteristics of the polar vortex related to the WN2-type features. Previous studies pointed out that the split-type SSW events related to the WN2 flux anomalies tended to have a stronger downward influence than the displacement-type SSW events (Nakagawa and Yamazaki, 2006; Mitchell et al., 2013). This was a potential explanation for the stronger coupling because the light-ice composite had a markedly stronger WN2 E-P flux anomaly. Although the causes of the different vertical coupling intensity were unclear, the obtained results suggested that the WPV events occurring in the light-ice years over the BKS tended to strongly affect the tropospheric circulation and the midlatitude surface temperature. This finding was consistent with the results of Garfinkel et al. (2017) and Kretschmer et al. (2018), showing that a recent low-temperature anomaly over Eurasia in winter was preceded by stratospheric polar vortex weakening.

4.3.2. Characteristics of Upward Planetary-Scale Wave Propagation

We next examined the mechanisms of the upward planetary wave propagation

and the 3D geopotential height structure. Figure 4.4 shows the 10-day (days −10 to −1) averaged composite anomalies of the 250 hPa geopotential height and the vertical structure of the eddy component (i.e., departure from the zonal mean) of the geopotential height and the 3D wave-activity flux formulated by Plumb (1985) at 60°N for the heavy- and light-ice WPV composites. Note that the upward wave-activity flux anomalies revealed an enhanced upward wave propagation compared to the climatological condition.

In the heavy-ice results, anticyclonic anomalies appeared over Europe and Siberia, while cyclonic anomalies appeared over the Arctic and the Kamchatka Peninsula at a 250 hPa level (Figure 4.4a). The longitude-height cross-section (Figure 4.4c) showed that the upward wave-activity flux anomalies emanated from the two tropospheric origins: anticyclonic anomalies over Europe and the cyclonic anomalies over the Kamchatka Peninsula. The position of the European anticyclonic anomaly is a precursory feature of the displacement-type SSW events reported by the previous studies (Martius et al., 2009; Castanheira and Barripedro, 2010; Nishii et al., 2011).

The 250 hPa geopotential height field of the light-ice WPV composite (Figure 4.4b) was characterized by the anticyclonic anomalies over the BKS and in a region extending southward and by the cyclonic anomalies from Siberia toward the North

Pacific. These anomalies showed a wave pattern over Eurasia with a westward tilting geopotential height structure (Figure 4.4d). Tilting was the strongest in the lower troposphere over the BKS. In addition, positive turbulent heat flux anomalies were found in the BKS, especially in the previous 10 days (days −20 to Day −11; not shown). All these features were regarded as a manifestation of a vertically propagating stationary Rossby wave caused by the sea ice reduction in the BKS, as previously discussed (e.g., Honda et al., 2009; Hoshi et al., 2017; Chapter 3 of this thesis). Along with this upward propagating anomalous wave, upward and eastward wave-activity flux anomalies appeared from the lower troposphere to the upper stratosphere. Another area of upward wave-activity fluxes was found around the International Date Line, but these fluxes were not seen in the middle to upper stratosphere. Thus, the WPVs in the light-ice winters tended to occur because of the intensified upward planetary wave propagation by the stationary Rossby wave partly related to the sea ice reduction in the BKS.

In the troposphere, the anticyclonic anomalies over the BKS seemed to result from a frequent occurrence of blocking highs, which preceded the split-type SSW events (e.g., Nishii et al., 2011). The eddy geopotential height field in the middle to the upper stratosphere had a more complicated structure in the light-ice conditions (e.g., a

mixed signature from the WN1 and WN2 geopotential height components) (Figures 4.4c and d). These results strongly supported that the WPV events in the light-ice years had WN2-type features.

We next decomposed the geopotential height field at 250 hPa into the WN1 and WN2 components. Figure 4.5a shows the DJF winter-mean climatology (i.e., the 36-year average). Figures 4.5b and c show the composite anomalies (deviation from the climatology) of the heavy- and light-ice WPV events averaged from days −10 to −1, respectively. The anomalous and climatological wave patterns in the heavy-ice composite appeared to be zonally in-phase only for the WN1 component. The maximum amplitude of the anomalous WN1 pattern was 65 m at 59°N, which is much larger than that of the anomalous WN2 field (37 m at 69°N). Note that the positive and negative regions of the anomalous WN1 pattern around 60°N corresponded to the two tropospheric precursors identified in Figure 4.4 c. From these facts, the heavy-ice composite was characterized by the WN1 intensifications in the 250 hPa geopotential height field and in the 100 hPa E–P flux result (Figure 4.3c).

A contrasting picture emerged in the light-ice composite (Figure 4.5c). Both anomalous WN1 and WN2 components of the 250 hPa geopotential fields were almost zonally in-phase with the respective climatological wave fields. Moreover, both WN1

and WN2 components of the anomalous wave field were constructively superposed over the Eastern Hemisphere. This is highly consistent with the wavy pattern in the Eurasian side in Figure 4.4b. We deduced the following interpretation: the anomalous stationary Rossby wave over Eurasia intensified both the WN1 and WN2 components of the climatological geopotential height field in the upper troposphere, and consequently, both the WN1 and WN2 components of the vertical E–P flux were increased in the lower stratosphere (Figure 4.3d). In contrast to the heavy-ice composite, the maximum amplitude of the anomalous WN2 component (66 m at 64°N) in the 250 hPa geopotential height field was larger than that of the WN1 component (51 m at 78°N) with a larger value of the WN2 E-P flux over the period of days −10 to −1 (Figure 4.3d). This demonstrates the strengthened role of the WN2 anomalies in the light-ice composites.

4.3.3. Discussions

The results of our composite analysis may contain the decadal time-scale variability of WPVs/SSWs and possible compounded influences from the increases in the greenhouse gases adding to our suggested influence from the sea ice. We showed the

results of the shorter period analysis to reduce those influences. The analyzed period was from 1979/1980 to 2004/2005, and the composites were based on nine heavy-ice and six light-ice events (Figure 4.1c). Although the sample size of these composites was smaller than that of our original composites, this analysis possibly provided further information. We calculated the anomalies in this additional analysis as the differences from the 31-day running averaged daily climatological mean of the shorter period.

The results of the E–P flux component-wise analysis showed similar characteristics to those in the original composite: the larger WN2 component in the light-ice composite (Figure 4.6d) and the dominant WN1 component in the heavy-ice composite (Figure 4.6c) just before Day 0. A similar pattern to the original result was also found in the 250 hPa geopotential height anomalies averaged from days −10 to −1 (e.g., an amplified WN2 geopotential height field and the anomalous wave pattern over Eurasia (not shown)). Furthermore, a stronger stratosphere–troposphere coupling in the zonal mean zonal wind field (Figure 4.6b) and negative surface air temperature anomalies in the midlatitude Eurasian regions (blue line in Figure 4.6f) were consistently found after around Day 0. The horizontal patterns of the surface air temperature averaged from days 1 to 30 were also consistent between the original and shorter-period results (Figure 4.7). The results for the linear detrended analysis over the

full 1979/1980–2014/2015 period were consistent (not shown). All these results implied that the characteristics obtained in our original analysis (Figures 4.3−4.5) did not substantially depend on the long-term climate change signals. But they represent features associated with the BKS sea ice loss. The midlatitude cold anomalies were also seen before Day 0 in the shorter-period light-ice composite (Figure 4.6f). We suggest this to be caused by the sea ice influences via the tropospheric pathway (e.g., anticyclonic anomalies around the BKS region) (Honda et al., 2009; Mori et al., 2014) (Figure 4.8a), and this process seems to be the different to that after Day 0, which was characterized by the negative AO/NAO-like circulation anomalies (Figure 4.8b).

We further evaluated the statistical significance for the WN2 contribution of the original light-ice composite using the Monte Carlo method and examined the following variables: the 100 hPa vertical E-P flux anomaly and the amplitude of the raw (not the anomaly) wave field in the 250 hPa geopotential height both averaged 40°N–80°N and from days −10 to −1. The WN2 component of these two variables in the light-ice composite was compared to 10,000 random subsamples of nine events taken from all 33 WPV events. The null hypothesis is that the composite averaged value is not different from the typical value of the WPVs. The p values for the WN2 E-P flux anomaly and the WN2 geopotential amplitude in the light-ice composite were 0.13 and 0.04,

respectively. These values provide supporting evidence for the notion that the light-ice composite has a significantly different WN2 contribution, especially in the geopotential height field just before the onset of the WPV events compared with the average WPV condition.

The problem of the small sample size in the observations still remained. We also analyzed the result of a long-term integration using AFES (HICE and LICE time-slice runs). Note that the boundary condition of this experiment had the largest SIC differences in the BKS in winter (Figure 3.2), and the simulated stratospheric circulation differences mostly resulted from the BKS sea ice reduction (Chapter 3 and Hoshi et al., 2017). Thus, this AFES experiment is suitable for a comparison with the reanalysis results. Using the AFES hindcast simulation results or the CMIP5 results may be another option. Although the analysis method is comparable to the reanalysis methods, the composite results contained other effects in addition to the sea ice. In the time-slice experiments, the simulated atmospheric differences come only from the sea ice changes. Thus, we adopted this time-slice experiment. We followed the detection scheme of the WPV events used in the reanalysis data, except that the NAM index was computed in the individual runs, and 62 and 56 WPV events were sampled in the HICE and LICE runs, respectively (approximately one event per model year). The anomalies

were calculated as the differences from a 31-day running averaged climatology of the HICE experiment.

We plotted the histograms of E–P flux based on a larger number of WPV events from the AFES experiments (Figure 4.9). The WN1 and WN2 components of the vertical 100 hPa E–P flux were averaged over 40 to 80°N and over the period of days –10 to 4 (15 days). We adopted the 15-day mean because in the LICE experiment, the daily composite values of the E–P fluxes peaked at around Day 0. However, the features were similar if we used 10-day average (days –10 to −1). Focusing on the peaks of the histograms of the WN1 component, a negative shift was found in the LICE experiment compared to the HICE experiment. The LICE experiment in the WN2 component showed a positive shift, and the WPVs with a large WN2 contribution (e.g., larger than 35,000 m^2/s^2) were more frequent in the LICE experiment than in the HICE experiment.

Computing the composite average of the WN2 E-P fluxes, the value for the light-ice experiment was 10,055 (m^2/s^2), which is 2.3 times larger than that for the heavy-ice experiment (4337 m^2/s^2), although these values were smaller than those in the reanalysis. The statistical test showed that the composite anomalies (i.e., differences from the climatology) of the WN2 component in both HICE and LICE experiments were statistically significant at the 99% confidence level, and the difference of the WN2

component between the composites was also statistically significant at the 95% confidence level. The WPV composite of the geopotential height anomalies over a 10-day period (days –10 to –1) from the AGCM results had a spatial pattern resembling that of the reanalysis, particularly a wave pattern from the BKS region in the light-ice WPVs (Figure 4.10b). The abovementioned results provide supporting evidence for an active role of the Arctic sea ice loss in modulating the WPV events, which was highly consistent when comparing the reanalysis data and the AGCM results.

A number of studies have discussed the factors which modulate wave propagation during the SSWs, for example, ENSO and QBO (Section 4.1). Using the reanalysis data, we investigated whether or not the vertical WN2 E-P flux values of individual WPV events in the original composites tend to be associated with specific ENSO or QBO phases. Figure 4.11 shows a scatter diagram of the WN1 (X-axis) and WN2 (Y-axis) components of the vertical E–P flux at the 100 hPa level averaged over 40°N–80°N and the period of days –10 to –1 for the heavy- and light-ice WPVs. The heavy-ice composite (Figure 4.11a) had nearly no WN2 contribution. In contrast, the light-ice composite (Figure 4.11b) had a long tail in the positive WN2 contribution. Then we see the presence/absence of ENSO and QBO influences particularly on the WN2 strength of the light-ice WPVs. Note that ENSO winters have been defined herein

as the DJF mean value of the monthly Niño 3.4 anomaly exceeding plus/minus 0.5 K. The easterly and westerly phases of the QBO were classified using a threshold of 0 m/s of the DJF mean zonal wind averaged from 5°S to 5°N at 50 hPa. The three largest WN2 events occurred in the La Niña winters (blue dots) along with the two weakest WN2 events, suggesting that La Niña does not control the WN2 strength in the light-ice WPVs. Similarly, no relationship was found between the WN2 strength and respective phases of the QBO (indicated by filled or open dots). Thus, the light-ice WPV feature (e.g., increase in the WN2 E–P flux) seemed not controlled by ENSO or QBO. However, testing this strictly from a smaller number of subsamples for a short reanalysis time period is difficult.

Our AFES simulation results can justify this issue. Our model did not internally generate the QBO (persistent weak easterlies in the equatorial zonal wind in the stratosphere, and the DJF mean climatology at 50 hPa is −7.1 m/s), and the same annual cycle of SST was prescribed as a boundary condition for every model year in both experiments (DJF mean monthly Niño 3.4 anomaly of 0.47 K from NOAA-CPC data). Although the experiment was not perfect with regard to the QBO and ENSO settings, the simulated differences came only from the sea ice difference. This suggests that the light-ice WPV features, such as the WN2 E–P flux increase and the tropospheric

precursory wave pattern, were modulated by the Arctic sea ice reduction.

We note that an amplitude of the vertical WN2 E-P flux anomalies in the AFES simulation was smaller than that in the reanalysis. One possible reason is that the reanalysis results indirectly contained effects from the QBO or ENSO. Additionally, the results would contain internal variability (e.g., blocking highs around the BKS and Ural regions, which are the precursors of the upward WN2 propagation). However, our analysis cannot answer this issue because the separation of these effects was difficult due to the short observation record and small subsamples. Another possible reason for the smaller WN2 amplitude is the model biases. The climatological values of the vertical WN2 E–P flux at 100 hPa were smaller in our model than those in the reanalysis; thus, the sensitivity of the WN2 would also be lower. This could be tested by analyzing the simulation results using other AGCMs. However, this is not the main focus of this study. We emphasized herein that the light-ice WPV features were qualitatively highly similar between the reanalysis and the AGCM simulation.

4.4. Summary

On the basis of the composite analysis applied to the WPV events, we found

distinct characteristics in the upward propagation of the planetary waves prior to the onset of the WPVs depending on the heavy- or light-sea ice conditions in the BKS. The heavy-ice composite was characterized by a dominant WN1 contribution to the E–P flux increase (Figure 4.3c), whereas the light-ice composite had a stronger WN2 contribution (Figure 4.3d). The increased WN2 E–P flux was related to the amplified WN2 geopotential height field in the upper troposphere (Figure 4.5c), which was caused by the stationary Rossby wave propagation over Eurasia (Figures 4.4b and d). The anomalous planetary wave field had the characteristics of an atmospheric response pattern arising from the sea ice reduction in the BKS (e.g., Honda et al., 2009; Hoshi et al., 2017). These results were supported by the shorter-period analysis (Figure 4.6) and the AGCM experiments (Figures 4.9–4.10). Thus, we conclude that under the present climate conditions, the Arctic sea ice reduction also acts as an important factor in modulating the WPV properties in addition to ENSO and QBO. Although our focus was on the WPV events, a significant portion of the WPV events also included SSWs (9 and 7 out of 17 and 9 heavy- and light-ice WPV events, respectively). The obtained results can be partly extended to the SSW events.

Our results indicate that the light-ice WPV events featured a stronger stratosphere–troposphere coupling in the zonal mean zonal wind field (Figures 4.3b and

4.6b) and an appearance of negative surface air temperature anomalies in the midlatitude land regions, particularly over Eurasia (Figures 4.3f and 4.6f and Figures 4.7b and d) following the onset of the WPV events. These results suggest that the recent Eurasian cold conditions (Cohen et al., 2014; Garfinkel et al., 2017) were partly related to the stronger vertical coupling of the WPV events modulated by the sea ice loss. A question remains about the mechanisms of the stronger vertical coupling. We pointed out two possible causes in Section 4.3.1, namely, the stronger WPV events and the WN2-type feature. Further examination is needed to clarify the mechanisms of the different vertical coupling strengths. Additionally, the mechanisms of the downward influences of the SSW events and the different vertical coupling intensities between the two SSW types have not yet been understood (e.g., Charlton and Polvani, 2007; Maycock and Hitchcock, 2015). A further investigation of the downward influences will contribute to understanding the coupling strength of light-ice WPV events.

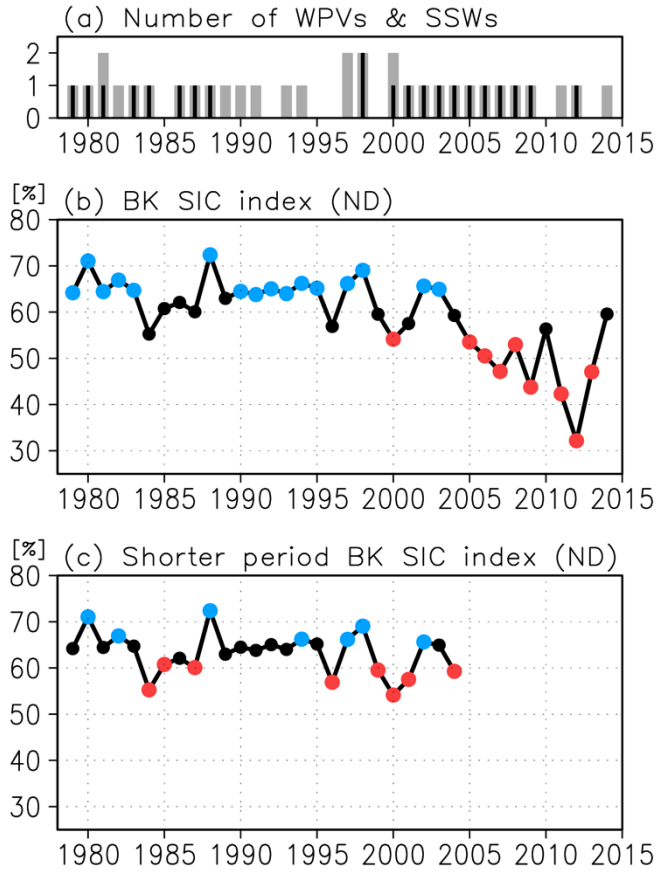

Figure 4.1 (a) The number of WPV events that occurred in each winter from 1979/1980 to 2014/2015 (gray bars) based on the JRA-55 data. The black bars indicate the number of SSW events. Time series of November–December mean SIC (%) averaged over the BKS (15°E–90°E, 70°N–85°N) in the period of (b) 1979/1980–2014/2015 and (c) 1979/1980–2004/2005, all based on the HadISST2 data. The SIC values that exceed plus (minus) 0.5 standard deviation during the respective periods are marked by blue (red) circles.

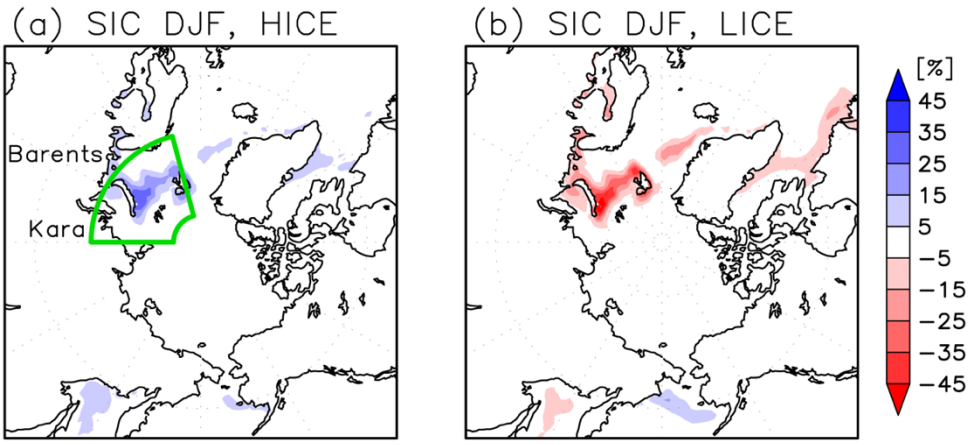

Figure 4.2 Composite anomalies of the DJF mean SIC (%) for the (a) heavy-ice (HICE) and (b) light-ice (LICE) winters. The anomaly is a deviation from the DJF climatological mean. The green box in Figure 4.2a represents the BKS region used for the SIC index. The HadISST2 data is used.

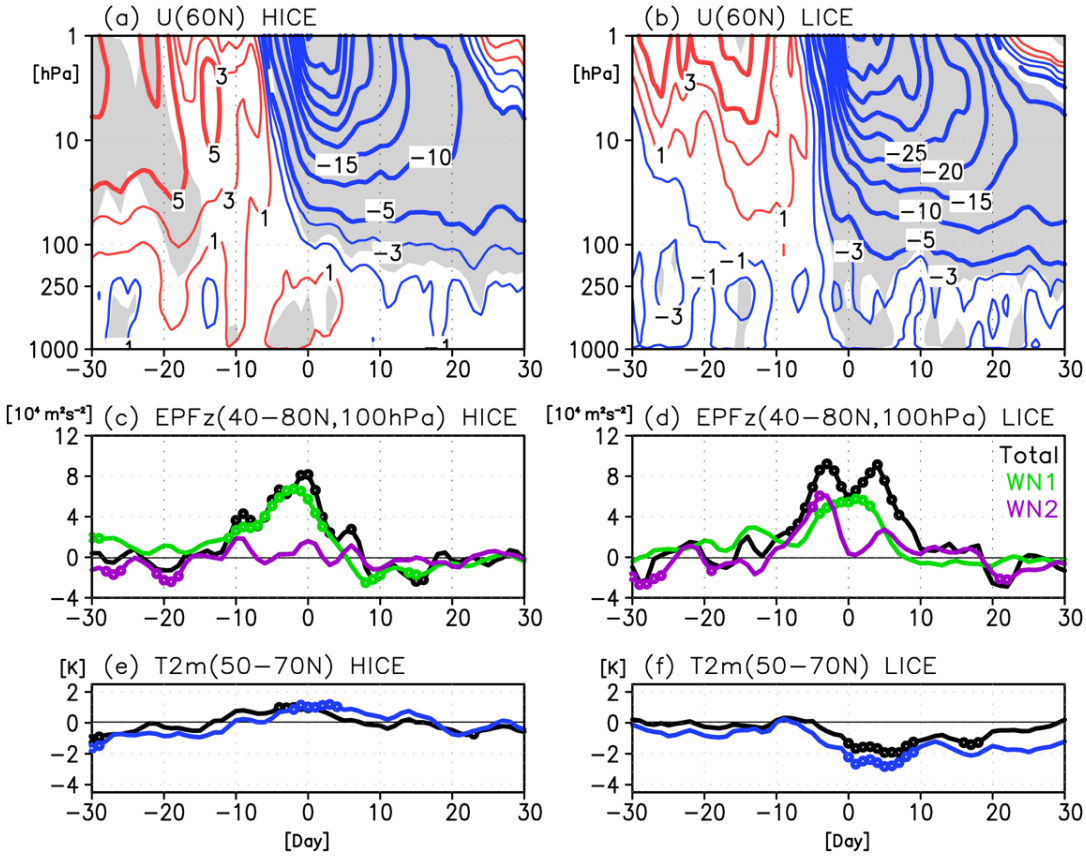

Figure 4.3 Composite anomalies of (top panels) the time–height cross-section of zonal mean zonal wind at 60°N (contour; m/s), (middle panels) 40°N–80°N averaged vertical E–P flux anomalies at 100 hPa (10^4 m^2 s^{-2}), and (bottom panels) 50°N–70°N land averaged 2 m temperature anomaly (K) for (left) heavy-ice and (right) light-ice WPV events as based on the JRA-55 data. The black, green, and purple lines in the middle panels indicate the total, WN1, and WN2 components of the E–P flux anomalies, respectively. The black and blue lines in the bottom panels indicate the

zonal (0°E–360°E) and Eurasian continent (0°E–180°E) averaged values, respectively. The shading in the top panels and the circle in the middle and bottom panels indicates 90% statistical significance.

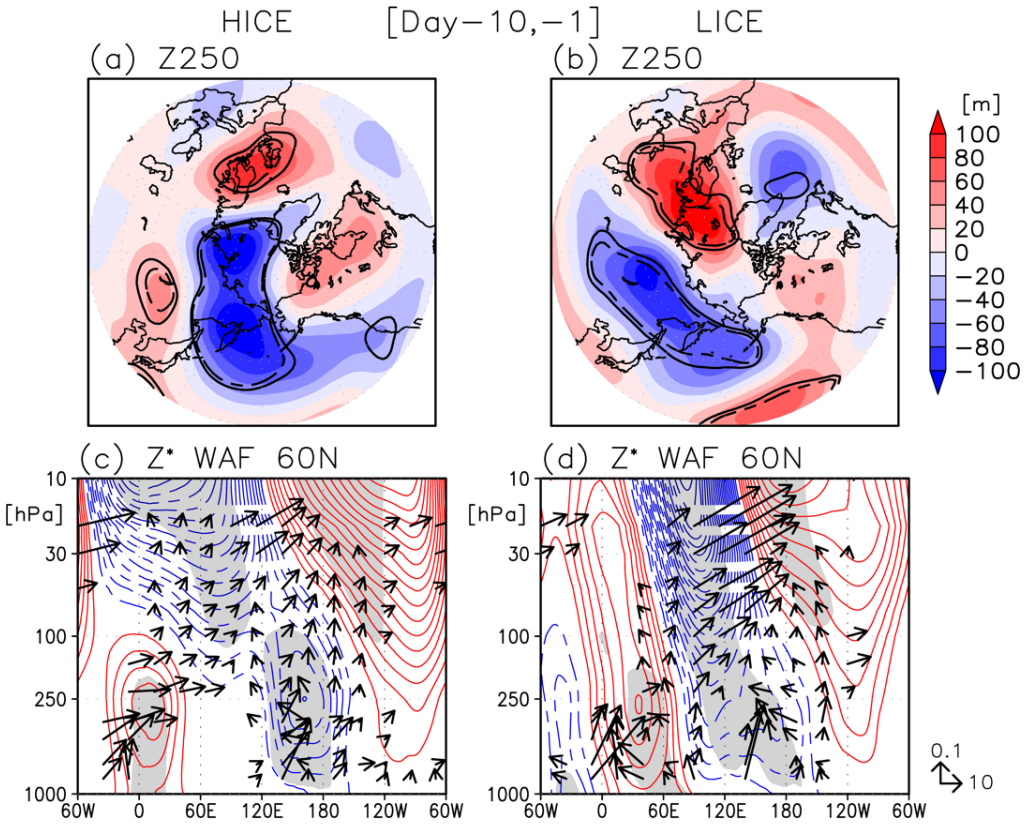

Figure 4.4 Composite anomalies in geopotential height at 250 hPa (shade; m) averaged from Day −10 to Day −1 for (a) heavy-ice and (b) light-ice WPV events based on the JRA-55 data. Solid and dashed lines indicate statistical significance at the 90% and 95% levels, respectively. The longitude–height cross-section of the eddy component of geopotential height anomalies (contours) at 60°N averaged from Day −10 to Day −1 for (c) heavy-ice and (d) light-ice WPV composites. The contour interval is 20 m, and 0 m is omitted. Shading indicates 95% statistical significance. Arrows

indicate the anomalies of the zonal and vertical components of the wave-activity flux (WAF; m^2 s^{-2}) defined by Plumb (1985). Anomalous vectors with small positive or negative vertical values (smaller than 0.005) are not plotted, and the vectors are scaled by the reciprocal square root of the density.

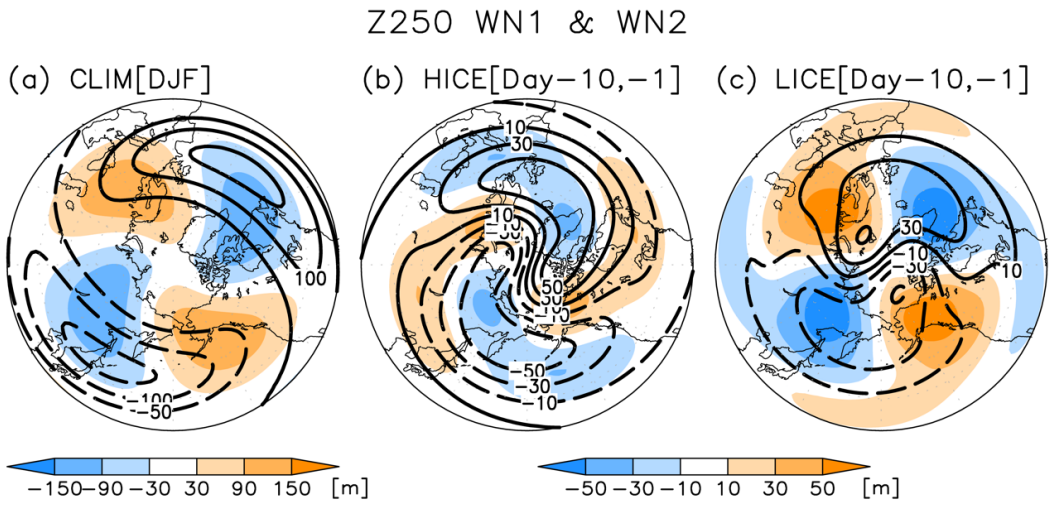

Figure 4.5 WN1 (contours) and WN2 (shade) components of the 250 hPa geopotential height (m) for (a) DJF mean climatology (CLIM; 1979/1980 to 2014/2015) and composite anomalies averaged from Day −10 to Day −1 for (b) heavy-ice and (c) light-ice WPV events. The JRA-55 data are used.

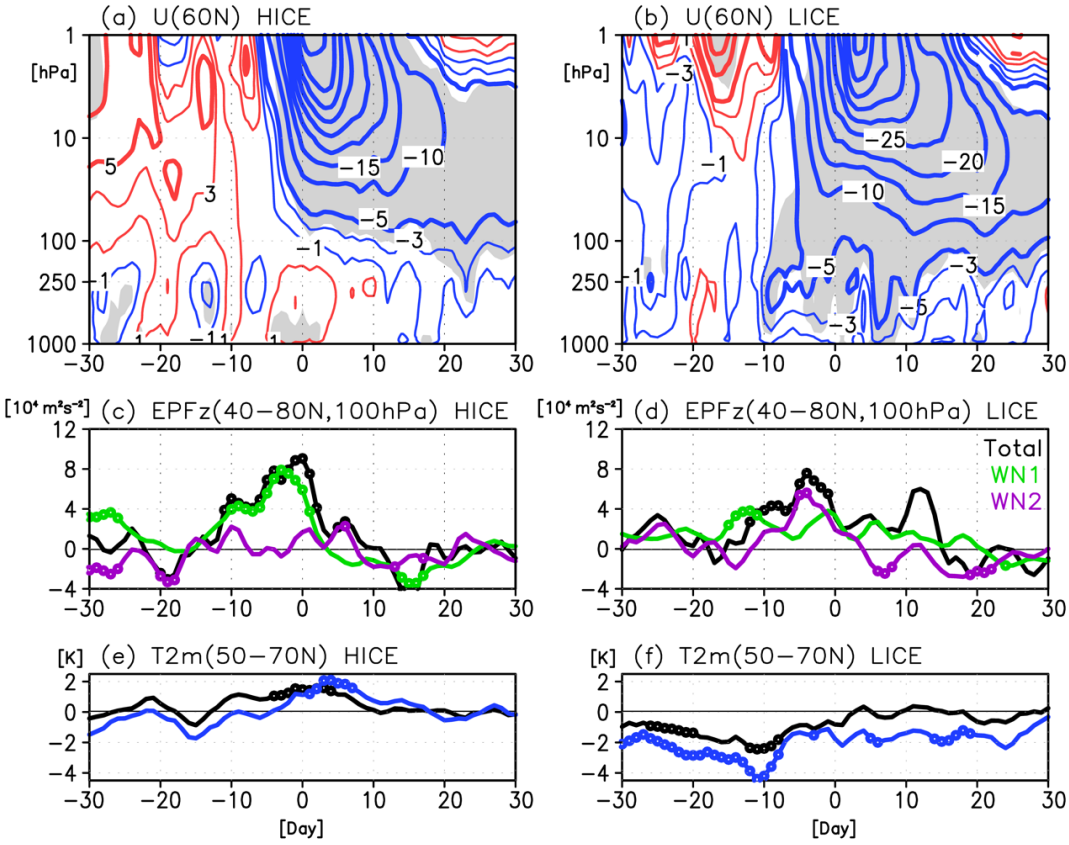

Figure 4.6 Same as Figure 4.3 but here are the results of the shorter-period analysis from 1979/1980 to 2004/2005. Anomalies represent differences from the climatological mean of the shorter period.

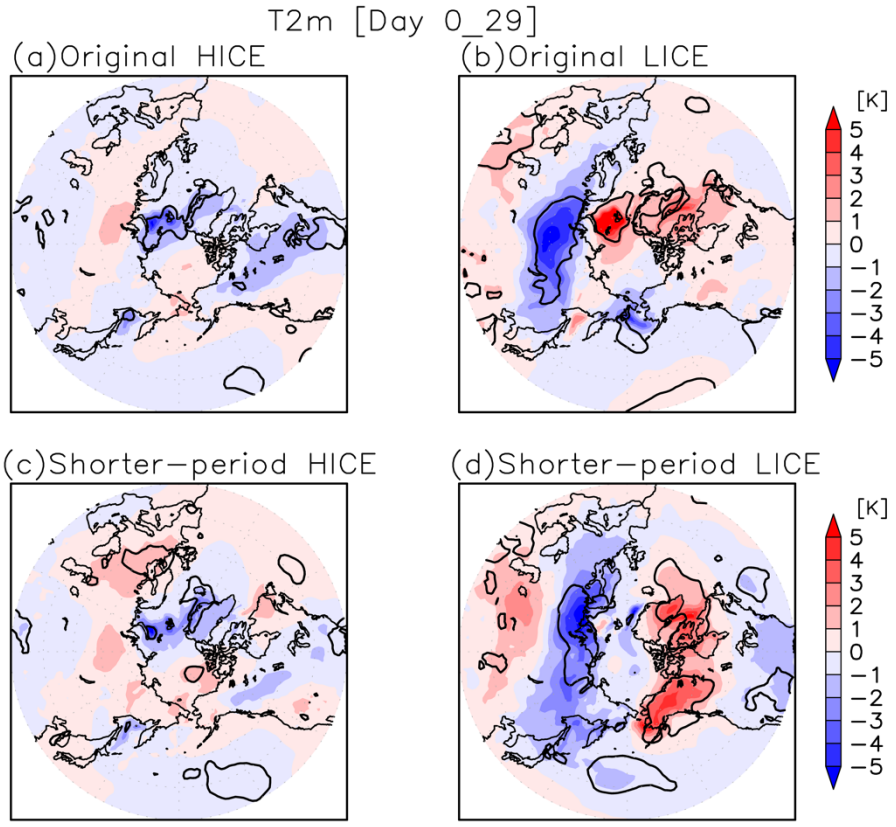

Figure 4.7 Composite anomalies in 2 m temperature (shade; m) averaged over the period from Day 0 to Day 29 (30 days) for (left) heavy-ice and (right) light-ice WPV events, based on JRA-55. Upper and lower panels are the results of the original and shorter-period analyses, respectively. Solid line indicates 95% statistical significance.

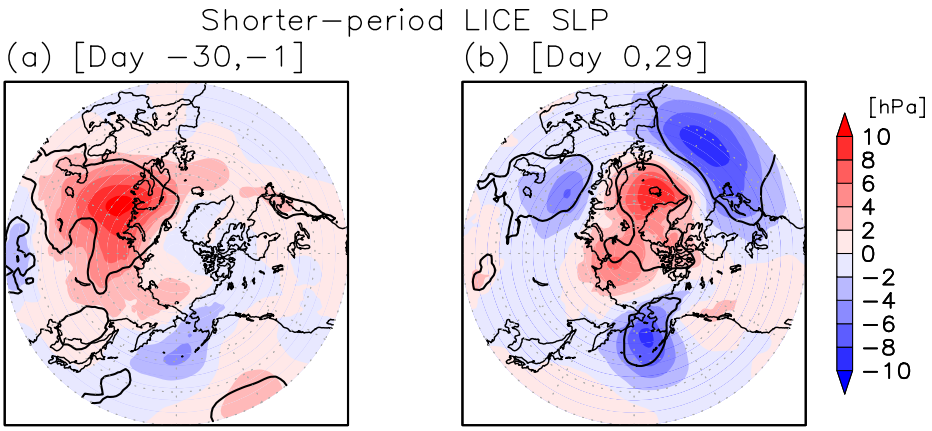

Figure 4.8 Same as in Figure 4.7d, but here the SLP anomalies (hPa) of the 30 day average (a) before Day 0 (Day –30 to Day –1) and (b) after Day 0 (Day 0 to Day 29).

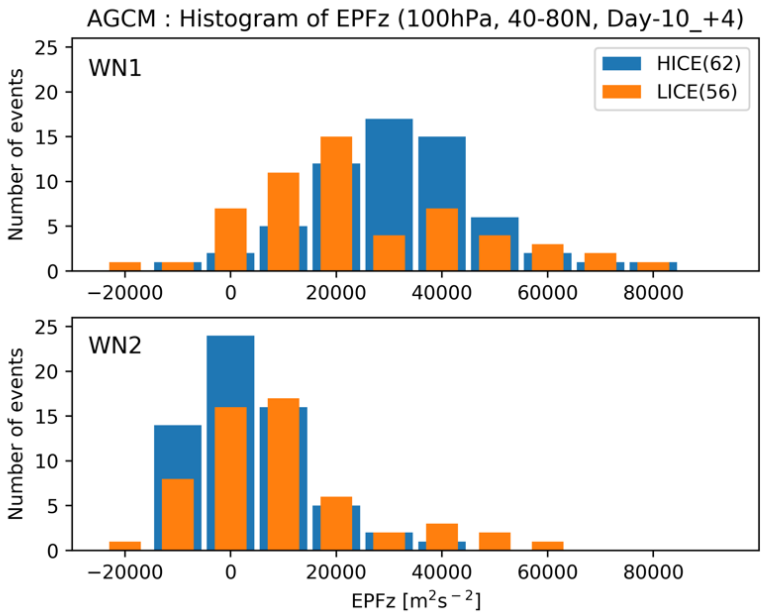

Figure 4.9 Histograms of 100 hPa vertical E–P flux anomalies averaged over 40–80°N and the 15 day mean (from Day –10 to 4) for the WPV events from the HICE (blue) and LICE (orange) experiments. Upper and lower panels show the results of WN1 and WN2 components, respectively.

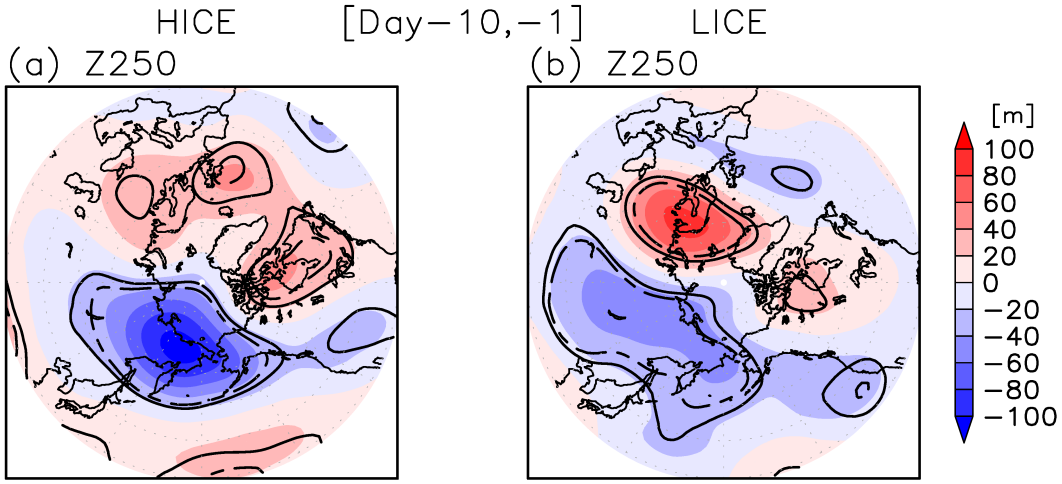

Figure 4.10 Same as Figures 4.4a and 4.4b but these correspond to results of the AFES time-slice experiments.

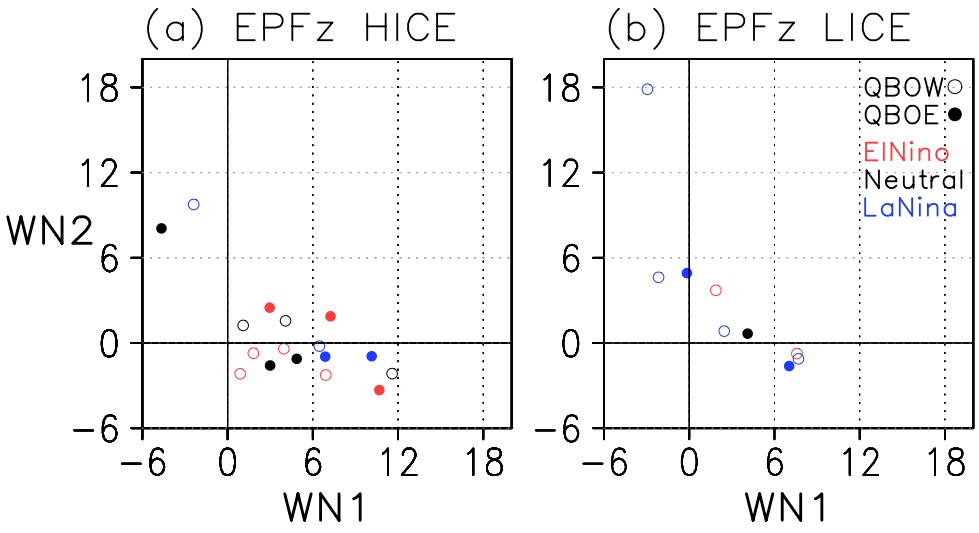

Figure 4.11 Scatter plots of vertical WN1 and WN2 E–P flux anomaly averaged 10 days (Day −10 to Day −1) and 40ºN-80ºN at 100 hPa (10^4 m^2 s^{-2}) for (a) heavy-ice and (b) light-ice WPV events based on the JRA-55 data. Events that occurred in QBO westerly and easterly winters are shown by open and filled circles, respectively. Events that occurred in El Niño, La Niña, and ENSO neutral winters are indicated by red, blue, and black circles, respectively.

Chapter 5.

Impact of Stratospheric Quasi-Biennial Oscillation on Arctic–Midlatitude Climate Linkage

5.1. Introduction

Recent studies have shown the important role of the stratospheric pathway in the Arctic–midlatitude climate linkage (Kim et al., 2014; Nakamura et al., 2016a; De and Wu, 2018). The previous chapter further indicated that the stronger vertical coupling of the WPV events modulated by the sea ice loss is the additional factor that induces the midlatitude cold anomalies.

However, the influence of sea ice loss on the Arctic–midlatitude climate linkage is still a subject of controversy. Some studies using AGCMs reported a lack of evidence regarding the impact of Arctic sea ice loss on Eurasian temperature (McCusker et al., 2016; Sun et al., 2016; Ogawa et al., 2018). It has been suggested that the impact of sea ice loss depends on background states related to global SST (Smith et al., 2017) and the phase of the AMO (Li et al., 2018). Incorporating air–sea coupling in a model is another

potential factor that changes the midlatitude temperature response to sea ice loss (Decer et al., 2016). Therefore, these complex features are important for understanding why model studies have shown divergent midlatitude temperature responses to sea ice loss (see Section 1.3 for more details).

We hypothesize that the different background condition of the stratospheric polar vortex is a potential factor that can modify the stratospheric pathway and tropospheric circulation responses to the sea ice variations. Moreover, this might be a key to the discrepancy among models because there are large differences among models in the strength and variability of the stratospheric polar vortex (e.g., Charlton-Perez et al., 2013). In particular, we address the question of the mean state dependence due to the phase of the QBO. The QBO is a phenomenon that consists of alternating westerly and easterly zonal winds in the equatorial stratosphere, which strongly modulates the interannual variation of the stratospheric polar vortex. Known as the Holton–Tan relationship, the polar vortex is weaker during the easterly phase of the QBO (i.e., QBOE) and stronger during the westerly phase of the QBO (i.e., QBOW) (Holton and Tan, 1980; Baldwin et al., 2001; Anstey and Shepherd, 2014). We examine whether a different stratospheric background state related to the QBO is important for the Arctic–midlatitude climate linkage by mainly using the JRA-55 dataset. To support the

observational results, we also analyze a result of AGCM historical simulation.

5.2. Data and Methods

JRA-55 and HadISST2 data are analyzed in the period from 1979/1980 to 2016/2017 (38 boreal winter seasons) (see also Table 2.1). The phase of the QBO is defined using the following procedure and is partially based on the previous study of Yamashita et al. (2011). First, we compute a QBO index, namely, the DJF-averaged zonal mean zonal wind at 50 hPa as averaged over 5°S to 5°N (the lower time series in Figure 5.1a). The winters are classified as QBOW or QBOE winters when the values exceed plus or minus 3 m s^{-1}, respectively. If the direction of the equatorial 50 hPa zonal wind changes during December to February, we exclude that winter from the sample set. These criteria resulted in 22 winters for the QBOW and 11 winters for the QBOE (indicated by red and blue marks, respectively, in Figure 5.1a). We also define QBO phases at 40 and 30 hPa pressure levels to test the robustness of the results. The 40 hPa definition leads to 18 winters for both QBOW and QBOE winters, and the 30 hPa definition results in 14 and 17 winters for QBOW and QBOE winters, respectively (Figure 5.1a). Note that the 50 hPa definition provides more QBOW winters than

QBOE winters. This is related to the nature of the QBO, in which westerly winds last longer at the equatorial lower stratosphere (Figure 2.3a).

We calculated the SIC time series averaged over the BKS (30°E–90°E, 65°N–85°N, shown by a green box in Figure 5.2a; hereafter this is referred to as the SIC_{BKS} index). Figure 5.1b shows the raw and detrended SIC_{BKS} index for December (see also Table 2.2). The relationships among BKS sea ice variability and atmospheric variables are examined in the following subsamples: the whole set of 38 winters (referred to as ALL), QBOW, and QBOE. Regression analysis is carried out with the atmospheric data on the normalized December SIC_{BKS} index after detrending linearly for both datasets to remove long-term climate change signals. A 38 year period is used to detrend and normalize the data to allow the comparison of the magnitudes of the regression coefficients between the 3 cases. Note that the negative trend of the SIC_{BKS} index exhibits nonlinearity. We also perform detrending of the SIC_{BKS} index by using a second-order fitting, but the regression results do not change (not shown). For the detrending of daily atmospheric data, a linear trend computed from 31-day running averaged daily data is removed from the original daily dataset. Statistical significances are evaluated by the two-sided Student's t-test for the ALL, QBOW, and QBOE subsamples.

The high-ice (HICE) and low-ice (LICE) winters are defined based on the plus or minus 0.5 standard deviation of the detrended December SIC_{BKS} index, respectively. As a measure of surface air temperature variability over central Eurasia, we use T_{CE}, which is defined as the 2 m temperature (K) averaged over the region (50°E–130°E, 40°N–65°N, as shown by an orange box in Figure 5.2a). The probability of an extreme-temperature day are examined using a threshold of plus/minus 3.1 K, which is 1 standard deviation of the detrended daily T_{CE} for the 38 year DJF period.

5.3. Results

The DJF mean 2 m temperature anomalies for the ALL winter is shown in Figure 5.2a. Similar to previous studies, negative temperature anomalies associated with low sea ice appear in the midlatitudes. Some regions, namely, eastern Eurasia, the Middle East, and the west coast of North America, show statistical significance above 95%. However, when subsampled with respect to the QBO phase, this picture changes drastically. For QBOE (Figure 5.2b), an area of negative temperature anomalies extends to all of central Eurasia, and the amplitudes of the anomalies are considerably larger than those in the ALL result. By contrast, northern central Eurasia and the east coast of

North America have positive temperature anomalies in QBOW (Figure 5.2c).

The QBO phase dependence is also seen in the scatterplot between the detrended December SIC_{BKS} and DJF mean T_{CE} indices (Figure 5.3a). When all winters are considered, no significant relationship is found between the BKS sea ice and central Eurasian temperature (r = 0.21, shown in Table 5.1). However, when restricted to the QBOE winters, this relationship becomes strong (r = 0.79) with the 99% statistical significance level. No such relationship is present for the QBOW cases (r = −0.20). Additional analysis indicates that this QBO phase dependence in the relationship between the SIC_{BKS} and T_{CE} is highly robust with respect to the choices of different QBO definitions and averaging periods for computing the SIC_{BKS} index (Table 5.1).

The QBO phase dependence is also evident on a daily time-scale (Figure 5.3b). For the QBOE winters, the frequency distribution of the detrended daily T_{CE} over the December–February period shifts to a colder state for the LICE winters than for HICE winters. By contrast, no such shift is found in the QBOW winters. The probability that central Eurasia experiences cold weather (defined as T_{CE} is below −3.1 K; see Section 5.2 for details) is higher when the sea ice conditions are low and the QBO is in the easterly phase (37.5 %) in comparison to that of the three remaining cases (Figure 5.3b).

Seeing winter-averaged geopotential height anomalies at 500 hPa that are related to the BKS sea ice loss, the QBOE result is characterized by an anticyclonic and cyclonic pair over the BKS and central Eurasia, respectively (Figure 5.2e). This dipole is known to be part of a quasi-stationary Rossby wave train that enhances surface Siberian high with cold anomalies over central Eurasia (Honda et al., 2009; Nakamura et al., 2015; Chapter 3). In the QBOE, a negative NAO-like signal also contributes to the Eurasian cold anomalies. In the QBOW (Figure 5.2f), the wave pattern over Eurasia is absent, and an opposite phase of the NAO anomaly is found. Therefore, different tropospheric circulation patterns related to sea ice loss contribute significantly to the presence or absence of Eurasian surface cold anomalies.

In the stratospheric circulation in the QBOE (Figure 5.4a), negative zonal mean zonal wind anomalies exist at 60°N in January following the strengthened vertical E–P flux at 100 hPa, and these stratospheric wind signals propagate downward to the troposphere. The positive E–P flux anomalies are consistent with the appearance of the tropospheric quasi-stationary Rossby wave pattern, which is known to be a precursor to the upward wave propagation anomaly as a response to the BKS sea ice loss (Kim et al., 2014; Hoshi et al., 2017; see Chapters 3 and 4). The stratospheric negative wind anomalies are less statistically significant; however, their downward penetrating feature

is still consistent with the negative NAO-like anomalies in the troposphere (Baldwin and Dunkerton, 2001). Therefore, this stratospheric pathway contributes to the strength and persistence of the midlatitude cold anomalies in the QBOE case. In the QBOW case (Figure 5.4b), there are no vertical E–P flux anomalies or stratospheric negative wind anomalies connecting to the troposphere.

It remains unclear why both the tropospheric and stratospheric circulation anomalies that are related to the sea ice variation differ between the two QBO phases. One possible mechanism is the influence of the stratospheric background states. The background polar vortex is stronger in the QBOW case than that in the QBOE case in early winter (Figure 5.4c), which is known as the Holton–Tan relationship (Holton and Tan, 1980; Baldwin et al., 2001; Anstey and Shepherd, 2014). When the polar vortex is too strong, there is less chance for planetary waves to propagate vertically (Charney and Drazin, 1961). This could explain the absence of the stratospheric pathway in the QBOW case (Figure 5.4b). Another possible mechanism is the difference in tropospheric circulation. However, the tropospheric background state does not differ between the QBO phases (see Figure 5.4c and Figure 5.5 for the horizontal pattern of the 500 hPa geopotential height). Further investigation is needed in future studies to achieve a better understanding of the relationship between the background state and

responses to the sea ice loss.

5.4. Discussion

The contrast in the impact of sea ice on midlatitude temperature under different QBO phases and its robustness were discussed in the previous section (Section 5.3). However, these features could be contaminated by external climate factors. If the QBO variation is related to other climate factors, the background states classified by the QBO phases might include those influences. Another possibility is that the relationship between the BKS sea ice and Eurasian temperature variation is due to other climate factors that control both the BKS sea ice and Eurasian temperature variations. Here we examine these two possibilities with a focus on the influences from the ENSO that cause global circulation anomalies in the troposphere and stratosphere. We use a DJF mean value of a monthly Niño 3.4 anomaly (referred to as the NINO3.4 index).

First, the statistical significances of the NINO3.4 index averaged for the ALL, QBOE, and QBOW cases are evaluated by the two-sided Student's t-test with a null hypothesis of no difference from zero (see the first line in Table 5.2). The results show that the mean value differs significantly (at 90% statistical significance) only in the

QBOE case defined by the 50 hPa QBO definition; the other cases exhibit no significant differences. Second, we calculate the correlation coefficients between the NINO3.4 and detrended December SIC_{BKS} indices and the NINO3.4 and detrended DJF mean T_{CE} indices for the three cases (see the second and third lines in Table 5.2, respectively). The results show that no statistically significant correlation exists at the 90% level except for the result of the QBOW case defined at 30 hPa. In this case, the T_{CE} index is correlated with the NINO3.4 index with a 95% statistical significance level. Considering that contamination from the ENSO is seen only in a few cases, we conclude that the ENSO is not a primary factor for the Arctic–midlatitude linkage and its QBO phase dependence discussed in the present chapter.

Since a limited number of winters are analyzed in the observation, the regression results may be influenced by natural atmospheric variability. Therefore, we additionally analyzed the results of a large-ensemble historical simulation conducted by AFES (see also Table 2.1). In this experiment, observed external forcings including sea ice and the QBO were prescribed (see Section 2.2 for experiment details). Since this simulation has 30 ensemble members, taking the ensemble mean reduces the natural variability, and simulated atmospheric fields likely reflect influences from prescribed external forcings.

Using the 50 hPa QBO index computed from the ensemble mean zonal winds, 12

and 15 winters are classified into the QBOE and QBOW phases, respectively (Figure 5.6). Note that fewer QBOW winters are obtained in the simulation than in the reanalysis. This can be explained by westerly winds in the equatorial lower stratosphere being slightly weaker in the simulation (Figure 2.3) due to the climatology of zonal mean zonal winds in non-nudged runs being easterly at the equatorial lower stratosphere (e.g., a DJF mean climatology at the equator and 50 hPa in the HICE run is -7.1 m s^{-1}) and the nudging intensity in the lower stratosphere being weaker (Figure 2.2). Even if the same winters were categorized as in the analysis of the JRA-55, the obtained results did not change substantially (not shown). After detrending both the ensemble averaged atmospheric data and December SIC_{BKS} index in the period from 1979/1980 to 2013/2014, regression analyses were conducted for the QBOE and QBOW cases separately as in the observation analysis.

Figure 5.7 shows regression anomalies of the DJF mean 2 m temperature and 500 hPa geopotential height for the QBOE and QBOW phases. Significant surface cold anomalies over Eurasia appear in the QBOE (Figure 5.7a). The circulation anomalies are characterized by negative AO/NAO-like anomalies and cyclonic anomalies over central Eurasia (Figure 5.7c). The stratospheric pathway, which is composed of the positive vertical E–P flux anomalies at 100 hPa, weaken polar vortexes, and downward

propagation of those signals is also seen in the QBOE results (Figure 5.8a). By contrast, those signals are absent or quite weak in the QBOW. The, results of the historical simulation support our findings that the Arctic–midlatitude linkage depends on the QBO phases.

However, it should be noted that the regression coefficients in the AGCM results are significantly smaller than those in the reanalysis. Some factors may account for the smaller amplitudes. One is the reproducibility of atmospheric responses in the AFES simulation. A standard deviation of ensemble mean and DJF-averaged detrended T_{CE} in the AFES simulation is 0.42 K, which is about one fourth of that in the JRA-55 data. This smaller year-to-year variability in the ensemble mean Siberian temperature results in smaller regression coefficients. Another possibility is that the reanalysis results partly contain influence from natural variability. Additionally, the smaller regression coefficients may result from a smaller amplitude of the simulated H–T relationship. We hypothesized that background differences of the stratospheric polar vortex related to the QBO are one of the reasons for the different Arctic–midlatitude linkage. Figure 5.8c indicates a composite difference of simulated zonal mean zonal winds at 60ºN between the QBOE and QBOW cases. Since the background polar vortex differences are smaller in the AFES simulation than in the reanalysis, it might be a possible reason. Although it

is unclear why the amplitudes of responses in the simulation are smaller, we again emphasize that the results of the regression analysis quantitatively support the observed results.

5.5. Summary

Although open questions remain and only a limited number of winters were analyzed from the observational record, this chapter indicates the difference in sea ice impact on winter midlatitude temperature under different QBO phases (Figures 5.2 and 5.3a). Tropospheric and stratospheric circulation anomalies related to sea ice variability are also different under the two QBO phases (Figures 5.2 and 5.4). Extended analysis further indicates that the obtained temperature results are not dependent on ENSO (see Table 5.2). The results were also supported by our additional correlation analyses (Table 5.1) and the AGCM historical simulation (Figures 5.7 and 5.8). Extreme-temperature days, which have a large impact on society and the economy, are also contrasted only in the QBOE winters (Figure 5.3b). The findings of this study will contribute to the improvement of midlatitude weather predictability by taking both the sea ice and QBO conditions into account.

The main focus of this study is to understand the influences of the recent Arctic sea ice loss. The future impact of Arctic sea ice loss on the atmospheric circulation under different QBO phases was investigated by Labe et al. (2019). They found that in early winter, the polar vortex weakens during QBOE and strengthens during QBOW in response to the future sea ice loss forcing. This difference in the polar vortex responses results in colder surface conditions over Eurasia during QBOE. Although their study was based on only an AGCM simulation and the focus was on the impact of future sea ice loss, the results are consistent with ours. Therefore, their results support our observation results that were obtained from a limited sample size.

Discrepancies in the atmospheric response to Arctic sea ice loss occur between observations and simulations as well as among simulations. The results of the current study suggest that the representation (or lack thereof) of the QBO and/or the basic state of the stratospheric circulation is a possible reason for such discrepancies. It has been reported that differences remain in the strength and variability of the stratospheric polar vortex of a model as compared with that of the reanalysis (e.g., Charlton-Perez et al., 2013). Furthermore, most of the AGCMs that have been used to examine the impact of sea ice in previous studies do not simulate the QBO. Considering the critical role of the stratospheric background state for the atmospheric response to sea ice loss,

improvement is needed in the stratospheric circulation component of models.

SIC_{BKS}	ALL winters	QBOE/QBOW winters, defined at		
		50 hPa	40 hPa	30 hPa
November	0.38^{**}	0.67^{**}/0.08	0.60^{***}/−0.10	0.63^{***}/0.10
December	0.21	0.79^{***}/−0.20	0.64^{***}/−0.32	0.54^{**}/−0.22
DJF	0.12	0.79^{***}/−0.30	0.54^{**}/-0.52^{**}	0.44^{*}/-0.64^{**}

Table 5.1 Correlation coefficients between the detrended SIC_{BKS} and DJF mean T_{CE} indices for ALL, QBOE, and QBOW winters. The November, December, and DJF mean SIC_{BKS} indices are used. The QBO is defined at three different levels: 50, 40, and 30 hPa. Statistically significant values at 90%, 95%, and 99% are indicated by *, **, and ***, respectively.

	ALL winters	QBOE/QBOW winters, defined at		
		50 hPa	40 hPa	30 hPa
NINO3.4 mean	0.02	−0.44*/0.15	−0.13/0.23	−0.11/0.15
NINO3.4 VS SIC_{BKS}	−0.01	0.18/−0.08	0.20/−0.17	0.21/−0.44
NINO3.4 VS T_{CE}	0.19	0.32/0.10	0.09/0.24	0.01/0.62**

Table 5.2 The NINO3.4 index averaged for ALL, QBOE, and QBOW cases (the first line). Correlation coefficients between NINO3.4 and detrended December SIC_{BKS} indices (the second line) and between NINO3.4 and detrended DJF mean T_{CE} indices (the third line) for ALL, QBOE, and QBOW winters. The QBO phase is defined at 50, 40, and 30 hPa. Statistically significant values at 90%, 95%, and 99% are indicated by *, **, and ***, respectively.

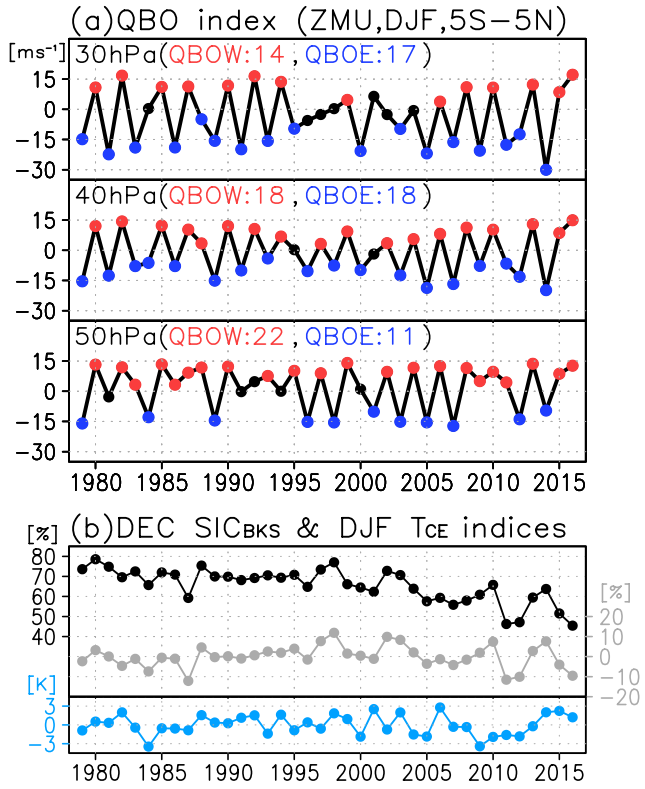

Figure 5.1 Time series from 1979/1980 to 2016/2017. (a) DJF mean and 5°S–5°N averaged zonal mean zonal wind (QBO index) at 30, 40, and 50 hPa. QBOE and QBOW winters are indicated by blue and red marks, respectively. The number of sampled winters for QBOE and QBOW are shown at the top of each plot. (b) December SIC averaged over the BKS (30°E–90°E, 65°N–85°N), SIC_{BKS} index (black), and its detrended time series (gray). A time series indicated by light blue shows detrended DJF mean 2 m temperature averaged over central Eurasia (50°E–130°E, 40°N–65°N), T_{CE} index.

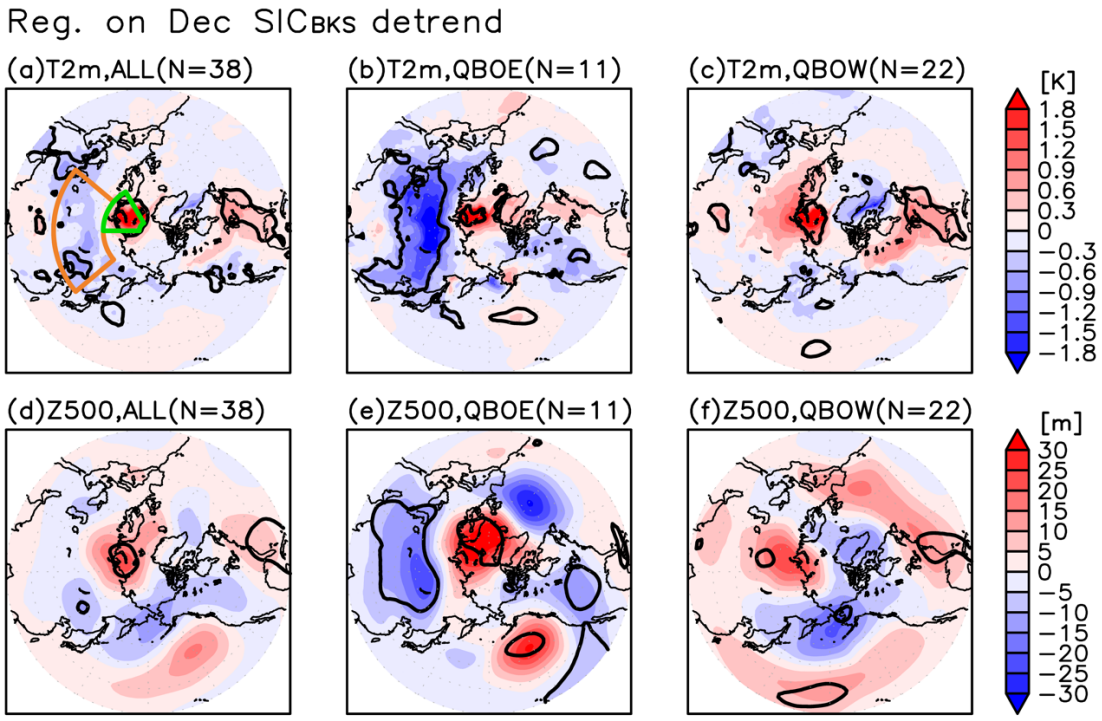

Figure 5.2 Regression coefficient of detrended DJF mean 2 m temperature (K) on normalized detrended December SIC_{BKS} index for (a) ALL, (b) QBOE, and (c) QBOW winters. The sign is reversed to reflect sea ice loss. The QBO is defined at the 50 hPa level. Contours indicate 95% statistically significant regions. (d–f) The same as that in (a–c) but for geopotential height at 500 hPa (m). The green and orange boxes in Figure 5.2a represent the regions of the BKS and central Eurasia, respectively.

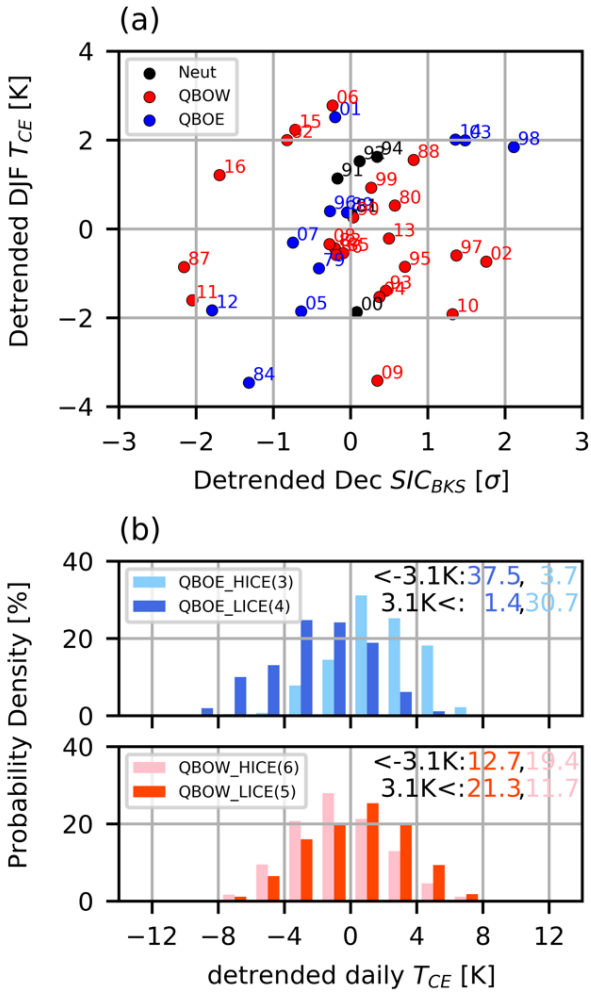

Figure 5.3 (a) Scatterplots of the detrended December SIC_{BKS} index (σ; x-axis) and the detrended DJF mean T_{CE} index (K; y-axis). The colors are used to indicate QBOE (blue), QBOW (red), and neutral (black) winters. The numbers beside the dots indicate years (e.g., 79 represents 1979/1980 winter). (b) Normalized histogram of detrended daily T_{CE} index during DJF winter (%) for the four cases. The number of winters for each case is

indicated in a legend. The probability of an extreme-temperature day, which is defined using a threshold of plus/minus 3.1 K, are listed at the top right of the plots.

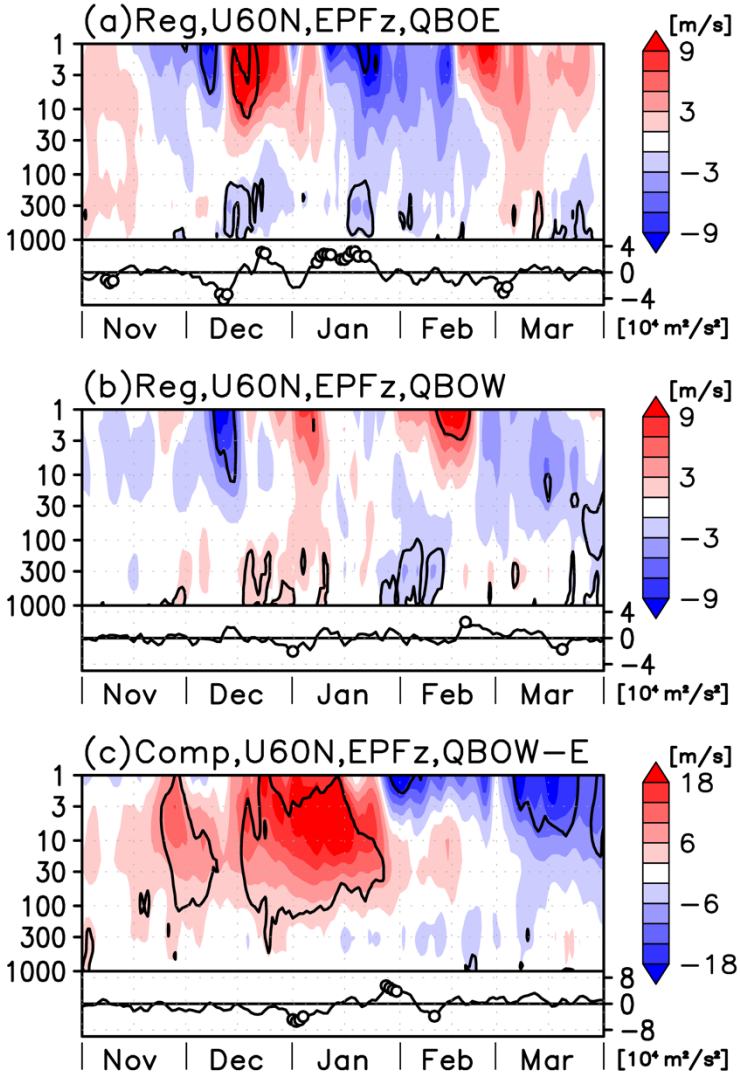

Figure 5.4 The same as that in Figures 5.2b and c, but for detrended zonal mean zonal wind at 60°N (upper, m s^{-1}) and vertical E–P flux at 100 hPa averaged over 40°N–80°N (lower, 10^4 m^2 s^{-2}), for (a) QBOE and (b) QBOW. Contours in the upper and marks in the lower indicate statistical significance at the 90% level. (c) A composite difference between QBOW and QBOE (QBOW–QBOE) for detrended zonal mean zonal wind at

60°N (upper) and vertical E–P flux at 100 hPa averaged over 40°N–80°N (lower). Contours in the upper and marks in the lower indicate statistical significance at the 95% level.

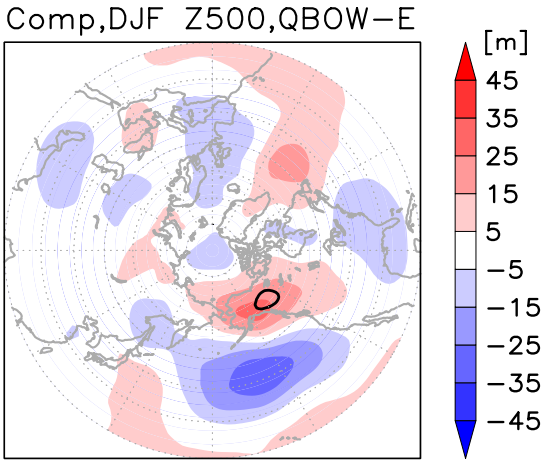

Figure 5.5 Composite difference of detrended DJF-averaged geopotential height at 500 hPa (m) between the QBOW and QBOE cases (QBOW–QBOE). Contours indicate a 95% statistical significance.

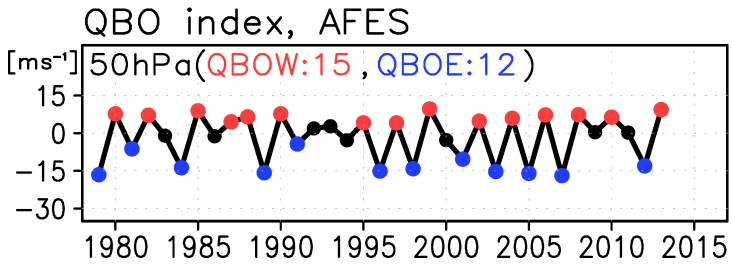

Figure 5.6 Same as in Figure 5.1a, but for the AFES historical experiment. The QBO is defined at 50 hPa.

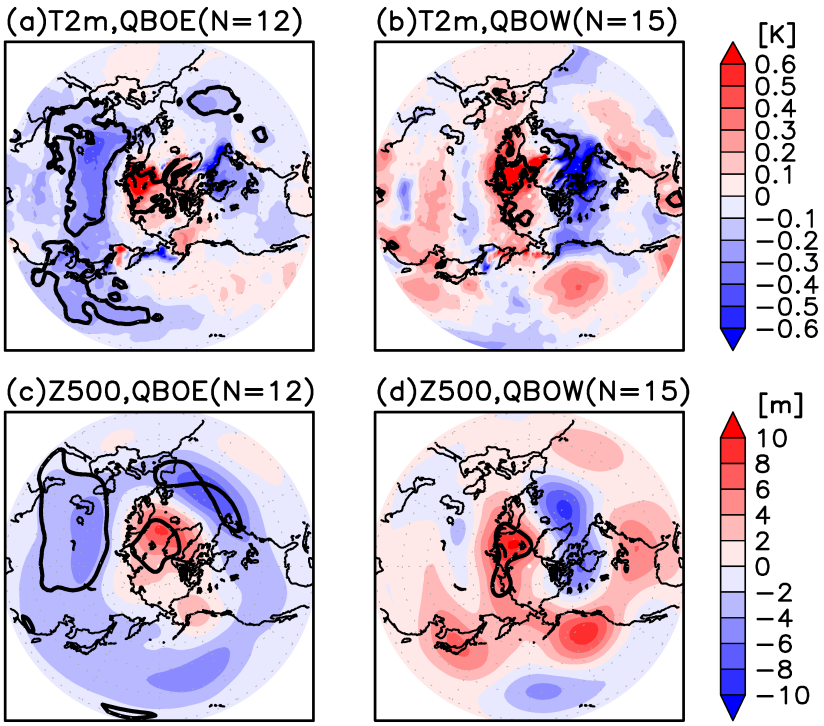

Figure 5.7 Same as in Figure 5.2, but for (a, c) QBOE and (b, d) QBOW results, based on the AFES historical experiment.

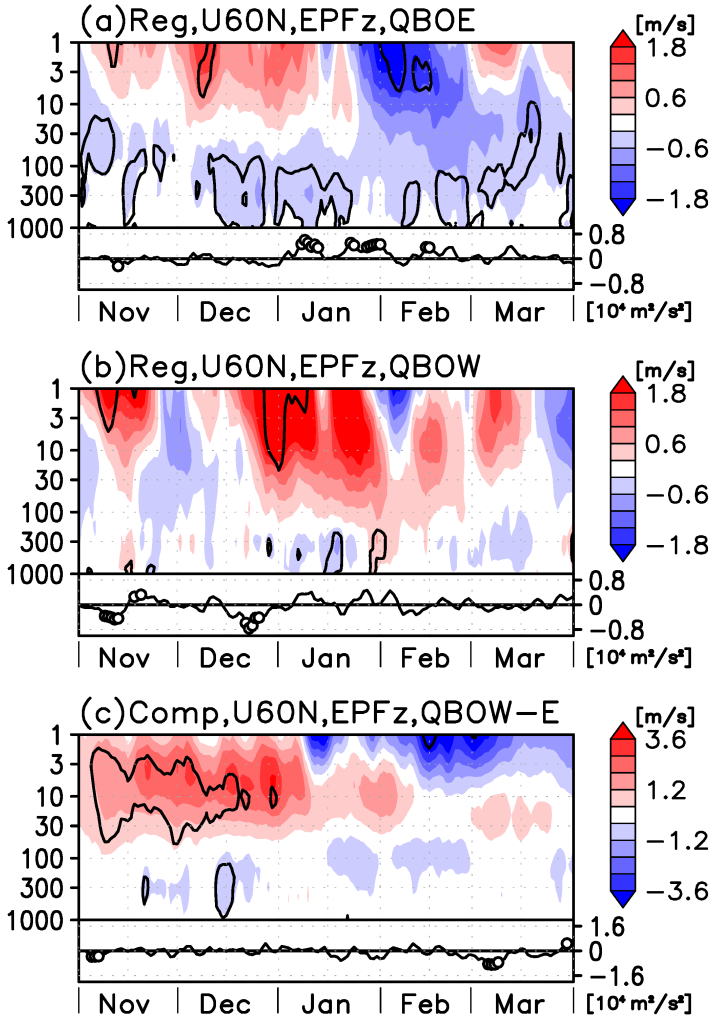

Figure 5.8 Same as in Figure 5.4, but for the results from the AFES historical experiment.

Chapter 6.

Conclusions and Discussion

The northern continents have experienced severe weather and cold winters in the recent decades. Studies have discussed the potential role of the recent significant loss of the Arctic sea ice (e.g., Honda et al., 2009; Koenigk et al., 2018; Mori et al., 2019) and the importance of the stratospheric pathway for the midlatitude colder conditions (e.g., Nakamura et al., 2016a; Wu and Smith, 2016). This thesis aimed at better understanding detailed processes of stratospheric pathways and the role of the stratosphere on the surface Arctic–midlatitude climate linkage. The three topics studied in this thesis are schematically illustrated by grey shading in Figure 6.1.

Note that SSW/WPV event is known as the extreme case of the stratospheric pathway and modulates significantly tropospheric circulation and midlatitude weather. This study, firstly, examined the spatial characteristics of the upward planetary wave propagation that drives the stratospheric pathway focusing on the mean state response to the Arctic sea ice loss. Then, the significant wave propagation that induces WPV events

and influences of the sea ice loss on it were examined. We also characterized downward influences of WPV events occurring in light-ice winters on the midlatitude surface temperature. Finally, modulations of the stratospheric pathway and the tropospheric responses to the sea ice loss due to the external factor were examined, focusing on the QBO. Details of the obtained results are described in the follows.

In Chapter 3, detailed processes of upward planetary wave propagation in the mean state induced by the recent Arctic sea ice loss were examined with a particular focus on the poleward eddy heat fluxes. The recent Arctic sea ice loss resulted in increased poleward eddy heat fluxes in the eastern and central Eurasia regions at the lower stratospheric level. Those increases in the heat fluxes arose from coupling of the climatological planetary wave field with temperature anomalies for the eastern Eurasia region and with meridional wind anomalies for the central Eurasia region. Propagation of stationary Rossby waves resulted in a dynamical link between these temperature and meridional wind anomalies with sea ice loss over the BKS. This study provided a detailed three-dimensional picture by that the recent Arctic sea ice loss modified the poleward eddy heat flux field in the lower stratosphere and subsequently affected the stratospheric wave structure.

Characteristics of the significant wave propagation during WPV events and the

contributions from the Arctic sea ice loss were examined in Chapter 4. Upward wave propagation during WPV events in heavy-ice years was dominated by the WN1 component, whereas WPV events occurring in light-ice years were characterized by stronger WN2 propagation. The WN2 propagation was caused by the stationary Rossby wave responses to the BKS sea ice loss. This result presents that under the present climate conditions, Arctic sea ice reduction acts as a factor in modulating upward propagating wave properties during WPV events.

Additionally, a stronger vertical coupling in the zonal mean zonal wind field following the onset of the WPV events was another feature of the light-ice year WPV events. In association with the prolonged easterly wind anomalies in the troposphere, negative surface air temperature anomalies also appeared in midlatitude land regions, particularly over Eurasia, for a few weeks. This result suggests that the stronger vertical coupling of the WPV events modulated by the sea ice loss is the additional factor that induces the midlatitude cold anomalies.

The important role of the stratospheric background condition related to the QBO on the stratospheric pathway and the Arctic–midlatitude climate linkage were also identified in Chapter 5. Note that the easterly and westerly phases of the QBO correspond to weaker and stronger polar vortex conditions, respectively. In the QBOE, a

strongly positive and highly significant relationship existed between the sea ice and Eurasian temperature variations. By contrast, we found no such relationship in the QBOW. Only in the QBOE, the sea ice variation was related to the stationary Rossby wave responses, stratospheric pathway, and tropospheric NAO anomalies, which caused temperature anomalies over Eurasia. Although the mechanisms of the influences of the stratospheric background remained unclear, this study provided the important knowledge of the stratospheric background state related to the QBO variation that improves our understanding of the Arctic–midlatitude climate linkage.

From the three research topics, this study indicated spatial characteristics of the upward planetary wave propagation that drives the stratospheric pathway, with focuses on the mean state and WPV responses to the sea ice loss. This study also showed the roles of the WPV events modulated by the sea ice loss and of the stratospheric QBO influence on the Arctic–midlatitude climate linkages.

In addition to the stratospheric process, processes within the troposphere have also been discussed, such as meandering of the westerly jet and modulations of storms, Rossby waves, and blocking highs (indicated by white shading in Figure 6.1). Other studies have discussed effects from the snow cover distribution over Eurasia, feedback processes through the ocean, and effects of atmospheric internal variability. However,

influences of the stratospheric processes on these tropospheric processes have not been well studied. In addition, the ozone distribution in the stratosphere and the 11-year solar cycle may modulate the stratospheric process associated with the Arctic sea ice loss. Toward a better understanding of atmospheric dynamics contributing to the Arctic–midlatitude climate linkage, we suggest that atmospheric responses to the recent Arctic sea ice loss should be comprehensively investigated in the stratosphere–troposphere coupled system.

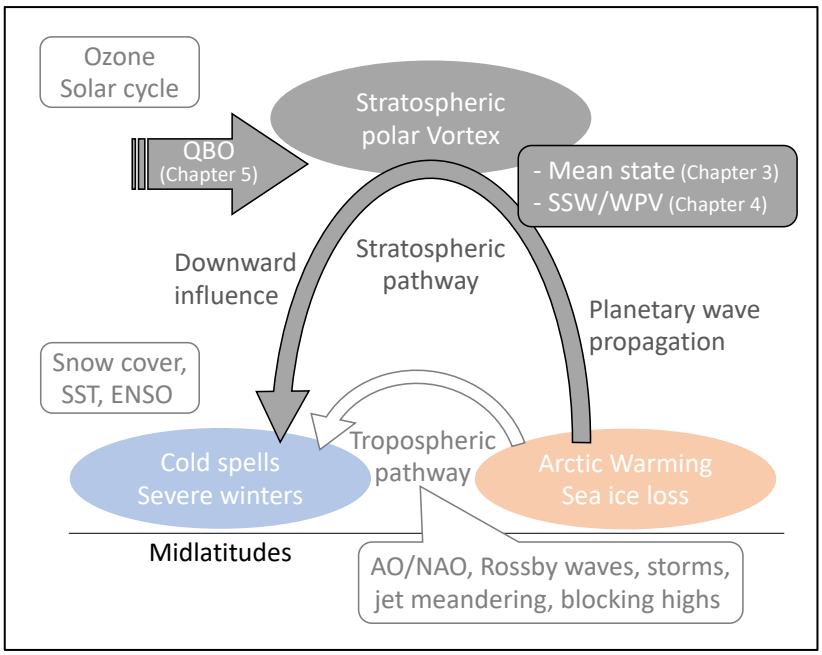

Figure 6.1 Schematic diagram of the link between Arctic climate changes and midlatitude colder conditions. Grey shading indicates topics investigated in this thesis, and white shading for phenomena that may be related to the Arctic–midlatitude linkage.

Acknowledgments

I am particularly grateful to my supervisors Prof. Jinro Ukita and Prof. Meiji Honda. They have always been willing to provide advice and guidance which has made the research in this thesis possible and enabled me to become a better scientist. Prof. Ukita has also generously supported me in attending domestic and international conferences and meetings where I could present my work and discuss it with researchers. I am also grateful to my committee members, Prof. Toru Nozawa and Prof. Katsuhisa Kawashima. I am also very grateful to Dr. Tetsu Nakamura and Prof. Koji Yamazaki for many valuable comments on my research. I had technical support from Dr. Nakamura in conducting the AFES experiments. I would also like to thank the coauthors of my research articles, Dr. Ralf Jaiser, Dr. Katsushi Iwamoto, Prof. Yasunobu Miyoshi, Dr. Klaus Dethloff, Dr. Dörthe Handorf, and Dr. Torben Koenigk. I am also grateful to Prof. Kazuaki Nishii and Prof. Yoshihiro Tachibana, who gave very helpful advice regarding my research. I am thankful to Satoru Kasuga and other students in our group for their tips and warm friendship. I had precious experiences during my stays at the University of Manitoba and University of Toronto. I am very grateful to Dr. Masayo Ogi and Prof. Paul Kushner for hosting me there. Those research visits were supported by the Early Career Scientist Fellowships for Arctic Environmental Research and the

Program for Overseas Visits by Young Researchers, respectively. I also acknowledge the Japan Society for the Promotion of Science (JSPS) Research Fellowships for Young Scientists. Finally, I wish to express my deep appreciation to my family for their loving encouragement and support.

References

Alexander, M. A., Bhatt, U. S., Walsh, J. E., Timlin, M. S., Miller, J. S., & Scott, J. D. (2004). The atmospheric response to realistic Arctic sea ice anomalies in an AGCM during winter. Journal of Climate, 17(5), 890-905.

Andrews, D. G., Leovy, C. B., & Holton, J. R. (1987). Middle atmosphere dynamics. International Geophysics Series, Academic Press.

Andrews, D. G., & McIntyre, M. E. (1976). Planetary waves in horizontal and vertical shear: The generalized Eliassen-Palm relation and the mean zonal acceleration. Journal of the Atmospheric Sciences, 33(11), 2031–2048.

Anstey, J. A., & Shepherd, T. G. (2014). High-latitude influence of the quasi-biennial oscillation. Quarterly Journal of the Royal Meteorological Society, 140(678), 1-21.

Baldwin, M. P., & Dunkerton, T. J. (1999). Propagation of the Arctic Oscillation from the stratosphere to the troposphere. Journal of Geophysical Research: Atmospheres, 104(D24), 30937-30946.

Baldwin, M. P., & Dunkerton, T. J. (2001). Stratospheric harbingers of anomalous weather regimes. Science, 294(5542), 581–584.

Baldwin, M. P., Gray, L. J., Dunkerton, T. J., Hamilton, K., Haynes, P. H., Randel, W. J., ... & Jones, D. B. A. (2001). The quasi-biennial oscillation. Reviews of Geophysics, 39(2), 179-229.

Barnes, E. A. (2013). Revisiting the evidence linking Arctic amplification to extreme weather in midlatitudes. Geophysical Research Letters, 40(17), 4734-4739.

Barnes, E. A., & Screen, J. A. (2015). The impact of Arctic warming on the midlatitude jet-stream: Can it? Has it? Will it?. Wiley Interdisciplinary Reviews: Climate Change, 6(3), 277-286.

Barriopedro, D., & Calvo, N. (2014). On the Relationship between ENSO, Stratospheric Sudden Warmings, and Blocking. Journal of Climate, 27(12), 4704–4720.

Blackport, R., & Kushner, P. J. (2016). The transient and equilibrium climate response to rapid summertime sea ice loss in CCSM4. Journal of Climate, 29(2), 401-417.

Blackport, R., & Kushner, P. J. (2017). Isolating the atmospheric circulation response to Arctic sea ice loss in the coupled climate system. Journal of Climate, 30(6), 2163-2185.

Boville, B. A. (1984). The influence of the polar night jet on the tropospheric circulation in a GCM. Journal of the Atmospheric Sciences, 41(7), 1132-1142.

Boville, B. A., & Cheng, X. (1988). Upper boundary effects in a general circulation model. Journal of the Atmospheric Sciences, 45(18), 2591-2606.

Butler, A.H., Seidel, D.J., Hardiman, S.C., Butchart, N., Birner, T., & Match, A. (2015). Defining Sudden Stratospheric Warmings. Bulletin of the American Meteorological Society, 96, 1913–1928.

Calvo, N., Giorgetta, M. A., Garcia-Herrera, R., & Manzini, E. (2009). Nonlinearity of the combined warm ENSO and QBO effects on the Northern Hemisphere polar vortex in MAECHAM5 simulations. Journal of Geophysical Research: Atmospheres, 114(D13), D13109.

Cassano, E. N., Cassano, J. J., Higgins, M. E., & Serreze, M. C. (2014). Atmospheric impacts of an Arctic sea ice minimum as seen in the Community Atmosphere Model. International Journal of Climatology, 34(3), 766-779.

Castanheira, J. M., & Barriopedro, D. (2010). Dynamical connection between tropospheric blockings and stratospheric polar vortex. Geophysical Research Letters, 37(13), L13809.

Charlton, A. J., & Polvani, L. M. (2007). A new look at stratospheric sudden warmings. Part I: Climatology and modeling benchmarks. Journal of Climate, 20(3), 449–

469.

Charlton-Perez, A. J., Baldwin, M. P., Birner, T., Black, R. X., Butler, A. H., Calvo, N., ... & Kim, J. (2013). On the lack of stratospheric dynamical variability in low-top versions of the CMIP5 models. Journal of Geophysical Research: Atmospheres, 118(6), 2494-2505.

Charney, J. G., & Drazin, P. G. (1961). Propagation of planetary-scale disturbances from the lower into the upper atmosphere. Journal of Geophysical Research, 66(1), 83–109.

Cohen, J., Barlow, M., Kushner, P. J., & Saito, K. (2007). Stratosphere–troposphere coupling and links with Eurasian land surface variability. Journal of Climate, 20(21), 5335-5343.

Cohen, J., Furtado, J. C., Jones, J., Barlow, M., Whittleston, D., & Entekhabi, D. (2014). Linking Siberian snow cover to precursors of stratospheric variability. Journal of Climate, 27(14), 5422-5432.

Cohen, J., Screen, J. A., Furtado, J. C., Barlow, M., Whittleston, D., Coumou, D., & Jones, J. (2014). Recent Arctic amplification and extreme mid-latitude weather. Nature Geoscience, 7(9), 627–637.

Crasemann, B., Handorf, D., Jaiser, R., Dethloff, K., Nakamura, T., Ukita, J., & Yamazaki, K. (2017). Can preferred atmospheric circulation patterns over the North-Atlantic-Eurasian region be associated with arctic sea ice loss?. Polar Science, 14, 9-20.

De, B., & Wu, Y. (2019). Robustness of the stratospheric pathway in linking the Barents-Kara Sea sea ice variability to the mid-latitude circulation in CMIP5 models. Climate Dynamics, 53(1-2), 193-207.

Dee, D. P., Uppala, S. M., Simmons, A. J., Berrisford, P., Poli, P., Kobayashi, S., ... & Bechtold, P. (2011). The ERA-Interim reanalysis: Configuration and performance of the data assimilation system. Quarterly Journal of the Royal Meteorological Society, 137(656), 553-597.

Deser, C., Magnusdottir, G., Saravanan, R., & Phillips, A. (2004). The effects of North Atlantic SST and sea ice anomalies on the winter circulation in CCM3. Part II: Direct and indirect components of the response. Journal of Climate, 17(5), 877-889.

Deser, C., Sun, L., Tomas, R. A., & Screen, J. (2016). Does ocean coupling matter for the northern extratropical response to projected Arctic sea ice loss?. Geophysical

Research Letters, 43(5), 2149-2157.

Deser, C., Tomas, R. A., & Peng, S. (2007). The transient atmospheric circulation response to North Atlantic SST and sea ice anomalies. Journal of Climate, 20(18), 4751-4767.

Enomoto, T., Kuwano-Yoshida, A., Komori, N., & Ohfuchi, W. (2008). Description of AFES 2: Improvements for high-resolution and coupled simulations. In High Resolution Numerical Modelling of the Atmosphere and Ocean (pp. 77-97). Springer, New York, NY.

Fletcher, C. G., Hardiman, S. C., Kushner, P. J., & Cohen, J. (2009). The dynamical response to snow cover perturbations in a large ensemble of atmospheric GCM integrations. Journal of Climate, 22(5), 1208-1222.

Fletcher, C. G., & Kushner, P. J. (2011). The role of linear interference in the annular mode response to tropical SST forcing. Journal of Climate, 24(3), 778-794.

Francis, J. A. (2017). Why are Arctic linkages to extreme weather still up in the air?. Bulletin of the American Meteorological Society, 98(12), 2551-2557.

Francis, J. A., Chan, W., Leathers, D. J., Miller, J. R., & Veron, D. E. (2009). Winter Northern Hemisphere weather patterns remember summer Arctic sea-ice extent.

Geophysical Research Letters, 36(7), L07503.

Francis, J. A., & Vavrus, S. J. (2012). Evidence linking Arctic amplification to extreme weather in mid-latitudes. Geophysical Research Letters, 39(6), L06801.

Free, M., & Seidel, D. J. (2009). Observed El Niño–Southern Oscillation temperature signal in the stratosphere. Journal of Geophysical Research: Atmospheres, 114(D23), D23108.

García-Serrano, J., Frankignoul, C., Gastineau, G., & de la Cámara, A. (2015). On the predictability of the winter Euro-Atlantic climate: Lagged influence of autumn Arctic sea ice. Journal of Climate, 28(13), 5195–5216.

Garfinkel, C. I., Butler, A. H., Waugh, D. W., Hurwitz, M. M., & Polvani, L. M. (2012). Why might stratospheric sudden warmings occur with similar frequency in El Niño and La Niña winters?. Journal of Geophysical Research: Atmospheres, 117(D19), D19106.

Garfinkel, C. I., Hartmann, D. L., & Sassi, F. (2010). Tropospheric precursors of anomalous Northern Hemisphere stratospheric polar vortices. Journal of Climate, 23(12), 3282-3299.

Garfinkel, C. I., Son, S.-W., Song, K., Aquila, V., & Oman, L. D. (2017). Stratospheric

variability contributed to and sustained the recent hiatus in Eurasian winter warming. Geophysical Research Letters, 44(1), 374–382.

Gong, T., Feldstein, S., & Lee, S. (2017). The role of downward infrared radiation in the recent Arctic winter warming trend. Journal of Climate, 30(13), 4937-4949.

Harada, Y., Kamahori, H., Kobayashi, C., Endo, H., Kobayashi, S., Ota, Y., ... & Takahashi, K. (2016). The JRA-55 Reanalysis: Representation of atmospheric circulation and climate variability. Journal of the Meteorological Society of Japan. Ser. II, 94(3), 269-302.

Holton, J. R., & Hakim, G. J. (2013). An introduction to dynamic meteorology. Waltham, MA.

Holton, J. R., & Tan, H. C. (1980). The influence of the equatorial quasi-biennial oscillation on the global circulation at 50 mb. Journal of the Atmospheric Sciences, 37(10), 2200-2208.

Holton, J. R., & Tan, H. C. (1982). The quasi-biennial oscillation in the Northern Hemisphere lower stratosphere. Journal of the Meteorological Society of Japan. Ser. II, 60(1), 140-148.

Honda, M., Inoue, J., & Yamane, S. (2009). Influence of low Arctic sea-ice minima on

anomalously cold Eurasian winters. Geophysical Research Letters, 36(8), L08707.

Honda, M., Yamazaki, K., Nakamura, H., & Takeuchi, K. (1999). Dynamic and thermodynamic characteristics of atmospheric response to anomalous sea-ice extent in the Sea of Okhotsk. Journal of Climate, 12(12), 3347-3358.

Hopsch, S., J. Cohen, & K. Dethloff (2012). Analysis of a link between fall Arctic sea ice concentration and atmospheric patterns in the following winter. Tellus A, 64, 18624,

Hoshi, K., Ukita, J., Honda, M., Iwamoto, K., Nakamura, T., Yamazaki, K., Dethloff, K., Jaiser, R., & Handorf, D. (2017). Poleward eddy heat flux anomalies associated with recent Arctic sea ice loss. Geophysical Research Letters, 44(1), 446–454.

Hoshi, K., Ukita, J., Honda, M., Nakamura, T., Yamazaki, K., Miyoshi, Y., & Jaiser, R. (2019a). Weak stratospheric polar vortex events modulated by the Arctic sea-ice loss. Journal of Geophysical Research: Atmospheres, 124(2), 858-869.

Hoshi, K., Ukita, J., Honda, M., Nakamura, T., Yamazaki, K., & Miyoshi, Y. (2019b). Characterizing stratosphere-troposphere coupling during weak polar vortex events in low Arctic sea ice years. Kaiyo Monthly, 579, 89–96. (in Japanese)

Hoskins, B. J., James, I. N., & White, G. H. (1983). The shape, propagation and mean-flow interaction of large-scale weather systems. Journal of the Atmospheric Sciences, 40(7), 1595-1612.

Hurrell, J. W., Hack, J. J., Shea, D., Caron, J. M., & Rosinski, J. (2008). A new sea surface temperature and sea ice boundary dataset for the Community Atmosphere Model. Journal of Climate, 21(19), 5145-5153.

Inoue, J., Hori, M. E., & Takaya, K. (2012). The role of Barents Sea ice in the wintertime cyclone track and emergence of a warm-Arctic cold-Siberian anomaly. Journal of Climate, 25(7), 2561-2568.

Jaiser, R., Dethloff, K., & Handorf, D. (2013). Stratospheric response to Arctic sea ice retreat and associated planetary wave propagation changes. Tellus A: Dynamic Meteorology and Oceanography, 65(1), 19375.

Jaiser, R., Dethloff, K., Handorf, D., Rinke, A., & Cohen, J. (2012). Impact of sea ice cover changes on the Northern Hemisphere atmospheric winter circulation. Tellus A: Dynamic Meteorology and Oceanography, 64(1), 11595.

Jaiser, R., Nakamura, T., Handorf, D., Dethloff, K., Ukita, J., & Yamazaki, K. (2016). Atmospheric autumn and winter response to Arctic sea ice changes in reanalysis

data and model simulations. Journal of Geophysical Research: Atmospheres, 121(13), 7564–7577.

Johnson, N. C., Xie, S. P., Kosaka, Y., & Li, X. (2018). Increasing occurrence of cold and warm extremes during the recent global warming slowdown. Nature Communications, 9(1), 1724.

Kay, J. E., & L'Ecuyer, T. (2013). Observational constraints on Arctic Ocean clouds and radiative fluxes during the early 21st century. Journal of Geophysical Research: Atmospheres, 118(13), 7219-7236.

Karpechko, A. Y., Charlton-Perez, A., Balmaseda, M., Tyrrell, N., & Vitart, F. (2018). Predicting sudden stratospheric warming 2018 and its climate impacts with a multimodel ensemble. Geophysical Research Letters, 45(24), 13-538.

Kidston, J., A. A. Scaife, C. Hardiman, D. M. Mitchell, N. Butchart, M. P. Baldwin, and L. J. Gray (2015). Stratospheric influence on tropospheric jet streams, storm tracks and surface weather. Nature Geoscience, 8, 433–440.

Kim, B.-M., Son, S.-W., Min, S.-K., Jeong, J.-H., Kim, S.-J., Zhang, X., Shim, T., & Yoon, H.-J. (2014). Weakening of the stratospheric polar vortex by Arctic sea-ice loss. Nature Communications, 5, 4646.

King, P., M., Hell, M., & Keenlyside, N. (2016). Investigation of the atmospheric mechanisms related to the autumn sea ice and winter circulation link in the Northern Hemisphere. Climate Dynamics, 46(3-4), 1185.

Kinoshita, T., & Sato, K. (2013a). A formulation of three-dimensional residual mean flow applicable both to inertia–gravity waves and to Rossby waves. Journal of the Atmospheric Sciences, 70(6), 1577-1602.

Kinoshita, T., & Sato, K. (2013b). A formulation of unified three-dimensional wave activity flux of inertia–gravity waves and Rossby waves. Journal of the Atmospheric Sciences, 70(6), 1603-1615.

Kobayashi, S., Ota, Y., Harada, Y., Ebita, A., Moriyama, M., Onoda, H., Onogi, K., Kamahori, H., Kobayashi, C., Endo, H., Miyaoka, K., & Takahashi, K. (2015). The JRA-55 Reanalysis: general specifications and basic characteristics. Journal of the Meteorological Society of Japan. Ser. II., 93(1), 5–48.

Kodera, K., Chiba, M., & Shibata, K. (1991). A general circulation model study of the solar and QBO modulation of the stratospheric circulation during the Northern Hemisphere winter. Geophysical Research Letters, 18(7), 1209-1212.

Kodera, K., & Kuroda, Y. (2002). Dynamical response to the solar cycle. Journal of

Geophysical Research: Atmospheres, 107(D24), ACL-5.

Koenigk, T., Gao, Y., Gastineau, G., Keenlyside, N., Nakamura, T., Ogawa, F., ... & Wang, T. (2019). Impact of Arctic sea ice variations on winter temperature anomalies in northern hemispheric land areas. Climate Dynamics, 52(5-6), 3111-3137.

Kretschmer, M., Coumou, D., Agel, L., Barlow, M., Tziperman, E., & Cohen, J. (2018). More-persistent weak stratospheric polar vortex states linked to cold extremes. Bulletin of the American Meteorological Society, 99(1), 49-60.

Kryjov, V. N., & Park, C. K. (2007). Solar modulation of the El-Niño/Southern Oscillation impact on the Northern Hemisphere annular mode. Geophysical Research Letters, 34(10), L10701.

Kug, J. S., Jeong, J. H., Jang, Y. S., Kim, B. M., Folland, C. K., Min, S. K., & Son, S. W. (2015). Two distinct influences of Arctic warming on cold winters over North America and East Asia. Nature Geoscience, 8(10), 759.

Kuroda, Y., & Kodera, K. (2002). Effect of solar activity on the polar-night jet oscillation in the Northern and Southern Hemisphere winter. Journal of the Meteorological Society of Japan. Ser. II, 80(4B), 973-984.

Kuwano‐Yoshida, A., Enomoto, T., & Ohfuchi, W. (2010). An improved PDF cloud scheme for climate simulations. Quarterly Journal of the Royal Meteorological Society, 136(651), 1583-1597.

Labe, Z., Peings, Y., & Magnusdottir, G. (2019). The effect of QBO phase on the atmospheric response to projected Arctic sea ice loss in early winter. Geophysical Research Letters, 46.

Labitzke, K. (1981). The amplification of height wave 1 in January 1979: A characteristic precondition for the major warming in February. Monthly Weather Review, 109(5), 983-989.

Labitzke, K. (1982). On the interannual variability of the middle stratosphere during the northern winters. Journal of the Meteorological Society of Japan. Ser. II., 60(1), 124–139.

Lang, A., Yang, S., & Kaas, E. (2017). Sea ice thickness and recent Arctic warming. Geophysical Research Letters, 44(1), 409-418.

Lau, N. C., & Nath, M. J. (1991). Variability of the baroclinic and barotropic transient eddy forcing associated with monthly changes in the midlatitude storm tracks. Journal of the Atmospheric Sciences, 48(24), 2589-2613.

Li, Q., Graf, H. F., & Giorgetta, M. A. (2007). Stationary planetary wave propagation in Northern Hemisphere winter? Climatological analysis of the refractive index. Atmospheric Chemistry and Physics, 7(1), 183-200.

Li, F., Orsolini, Y. J., Wang, H., Gao, Y., & He, S. (2018). Atlantic Multidecadal Oscillation modulates the impacts of Arctic sea ice decline. Geophysical Research Letters, 45(5), 2497-2506.

Limpasuvan, V., & Hartmann, D. L. (2000). Wave-maintained annular modes of climate variability. Journal of Climate, 13(24), 4414-4429.

Limpasuvan, V., Thompson, D. W. J., & Hartmann, D. L. (2004), The life cycle of the Northern Hemisphere sudden stratospheric warmings, Journal of Climate, 17(13), 2584–2596.

Liu, J., Curry, J. A., Wang, H., Song, M., & Horton, R. M. (2012). Impact of declining Arctic sea ice on winter snowfall. Proceedings of the National Academy of Sciences, 109(11), 4074-4079.

Magnusdottir, G., Deser, C., & Saravanan, R. (2004). The effects of North Atlantic SST and sea ice anomalies on the winter circulation in CCM3. Part I: Main features and storm track characteristics of the response. Journal of Climate, 17(5),

857-876.

Manzini, E., Giorgetta, M. A., Esch, M., Kornblueh, L., & Roeckner, E. (2006). The influence of sea surface temperatures on the northern winter stratosphere: Ensemble simulations with the MAECHAM5 model. Journal of Climate, 19(16), 3863-3881.

Martius, O., Polvani, L. M., & Davies, H. C. (2009). Blocking precursors to stratospheric sudden warming events. Geophysical Research Letters, 36(14), L14806.

Matsuno, T. (1971). A dynamical model of the stratospheric sudden warming. Journal of the Atmospheric Sciences, 28(8), 1479–1494.

Maycock, A. C., & Hitchcock, P. (2015). Do split and displacement sudden stratospheric warmings have different annular mode signatures?. Geophysical Research Letters, 42(24), 10-943.

Maykut, G. A. (1982). Large-scale heat exchange and ice production in the central Arctic. Journal of Geophysical Research: Oceans, 87(C10), 7971-7984.

McCusker, K. E., Fyfe, J. C., & Sigmond, M. (2016). Twenty-five winters of unexpected Eurasian cooling unlikely due to Arctic sea-ice loss. Nature

Geoscience, 9(11), 838.

McKenna, C. M., Bracegirdle, T. J., Shuckburgh, E. F., Haynes, P. H., & Joshi, M. M. (2018). Arctic sea ice loss in different regions leads to contrasting Northern Hemisphere impacts. Geophysical Research Letters, 45(2), 945-954.

Mitchell, D. M., Gray, L. J., Anstey, J., Baldwin, M. P., & Charlton-Perez, A. J. (2013). The influence of stratospheric vortex displacements and splits on surface climate. Journal of Climate, 26(8), 2668–2682.

Mori, M., Watanabe, M., Shiogama, H., Inoue, J., & Kimoto, M. (2014). Robust Arctic sea-ice influence on the frequent Eurasian cold winters in past decades. Nature Geoscience, 7(12), 869.

Mori, M., Kosaka, Y., Watanabe, M., Nakamura, H., & Kimoto, M. (2019). A reconciled estimate of the influence of Arctic sea-ice loss on recent Eurasian cooling. Nature Climate Change, 9(2), 123.

Naito, Y., & Hirota, I. (1997). Interannual variability of the northern winter stratospheric circulation related to the QBO and the solar cycle. Journal of the Meteorological Society of Japan. Ser. II, 75(4), 925-937.

Nakagawa, K. I., & Yamazaki, K. (2006). What kind of stratospheric sudden warming

propagates to the troposphere?. Geophysical Research Letters, 33(4), L04801.

Nakamura, T., Yamazaki, K., Honda, M., Ukita, J., Jaiser, R., Handorf, D., & Dethloff, K. (2016b). On the atmospheric response experiment to a Blue Arctic Ocean. Geophysical research letters, 43(19), 10-394.

Nakamura, T., Yamazaki, K., Iwamoto, K., Honda, M., Miyoshi, Y., Ogawa, Y., & Ukita, J. (2015). A negative phase shift of the winter AO/NAO due to the recent Arctic sea-ice reduction in late autumn. Journal of Geophysical Research: Atmospheres, 120(8), 3209–3227.

Nakamura, T., Yamazaki, K., Iwamoto, K., Honda, M., Miyoshi, Y., Ogawa, Y., Tomikawa, Y., & Ukita, J. (2016a). The stratospheric pathway for Arctic impacts on midlatitude climate. Geophysical Research Letters, 43(7), 3494–3501.

Nishii, K., Nakamura, H., & Miyasaka, T. (2009). Modulations in the planetary wave field induced by upward-propagating Rossby wave packets prior to stratospheric sudden warming events: A case-study. Quarterly Journal of the Royal Meteorological Society, 135(638), 39-52.

Nishii, K., Nakamura, H., & Orsolini, Y. J. (2011). Geographical dependence observed in blocking high influence on the stratospheric variability through enhancement

and suppression of upward planetary-wave propagation. Journal of Climate, 24(24), 6408–6423.

Ogawa, F., Keenlyside, N., Gao, Y., Koenigk, T., Yang, S., Suo, L., ... & Omrani, N. E. (2018). Evaluating impacts of recent Arctic sea ice loss on the northern hemisphere winter climate change. Geophysical Research Letters, 45(7), 3255-3263.

Ohfuchi, W., H. Nakamura, M. K. Yoshioka, T. Enomoto, K. Takaya, X. Peng, S. Yamane, T. Nishimura, Y. Kurihara, and K. Ninomiya (2004). 10-km mesh meso-scale resolving simulations of the global atmosphere on the Earth Simulator—Preliminary outcomes of AFES (AGCM for the Earth Simulator). Journal of the Earth Simulator, 1, 8–34.

Onogi, K., Tsutsui, J., Koide, H., Sakamoto, M., Kobayashi, S., Hatsushika, H., ... & Kadokura, S. (2007). The JRA-25 reanalysis. Journal of the Meteorological Society of Japan. Ser. II, 85(3), 369-432.

Orsolini, Y. J., Senan, R., Benestad, R. E., & Melsom, A. (2012). Autumn atmospheric response to the 2007 low Arctic sea ice extent in coupled ocean–atmosphere hindcasts. Climate Dynamics, 38(11-12), 2437-2448.

Overland, J. E., Dethloff, K., Francis, J. A., Hall, R. J., Hanna, E., Kim, S. J., ... & Vihma, T. (2016). Nonlinear response of mid-latitude weather to the changing Arctic. Nature Climate Change, 6(11), 992.

Overland, J. E., & Wang, M. (2010). Large-scale atmospheric circulation changes are associated with the recent loss of Arctic sea ice. Tellus A, 62(1), 1-9.

Overland, J. E., Wood, K. R., & Wang, M. (2011). Warm Arctic–cold continents: climate impacts of the newly open Arctic Sea. Polar Research, 30(1), 15787.

Palmeiro, F. M., Barriopedro, D., García-Herrera, R., & Calvo, N. (2015). Comparing sudden stratospheric warming definitions in reanalysis data. Journal of Climate, 28(17), 6823–6840.

Pedersen, R. A., Cvijanovic, I., Langen, P. L., & Vinther, B. M. (2016). The impact of regional Arctic sea ice loss on atmospheric circulation and the NAO. Journal of Climate, 29(2), 889-902.

Peings, Y., Douville, H., Colin, J., Martin, D. S., & Magnusdottir, G. (2017). Snow–(N)AO teleconnection and its modulation by the Quasi-Biennial Oscillation. Journal of Climate, 30(24), 10211-10235.

Peings, Y., & Magnusdottir, G. (2014). Response of the wintertime Northern

Hemisphere atmospheric circulation to current and projected Arctic sea ice decline: A numerical study with CAM5. Journal of Climate, 27(1), 244-264.

Peings, Y., Saint-Martin, D., & Douville, H. (2012). A numerical sensitivity study of the influence of Siberian snow on the northern annular mode. Journal of Climate, 25(2), 592-607.

Petoukhov, V., & Semenov, V. A. (2010). A link between reduced Barents-Kara sea ice and cold winter extremes over northern continents. Journal of Geophysical Research: Atmospheres, 115(D21), D21111.

Petrie, R. E., Shaffrey, L. C., & Sutton, R. T. (2015). Atmospheric impact of Arctic sea ice loss in a coupled ocean–atmosphere simulation. Journal of Climate, 28(24), 9606-9622.

Plumb, R. A. (1985). On the three-dimensional propagation of stationary waves. Journal of the Atmospheric Sciences, 42(3), 217–229.

Plumb, R. A. (1986). Three-dimensional propagation of transient quasi-geostrophic eddies and its relationship with the eddy forcing of the time—mean flow. Journal of the Atmospheric Sciences, 43(16), 1657-1678.

Polvani, L. M., & Waugh, D. W. (2004). Upward wave activity flux as a precursor to

extreme stratospheric events and subsequent anomalous surface weather regimes. Journal of Climate, 17(18), 3548–3554.

Previdi, M., & Polvani, L. M. (2014). Climate system response to stratospheric ozone depletion and recovery. Quarterly Journal of the Royal Meteorological Society, 140(685), 2401-2419.

Quiroz, R. S. (1986). The association of stratospheric warmings with tropospheric blocking. Journal of Geophysical Research: Atmospheres, 91(D4), 5277–5285.

Randel, W. J., Shine, K. P., Austin, J., Barnett, J., Claud, C., Gillett, N. P., ... & Mears, C. (2009). An update of observed stratospheric temperature trends. Journal of Geophysical Research: Atmospheres, 114(D2), D02107.

Rayner, N. A. A., Parker, D. E., Horton, E. B., Folland, C. K., Alexander, L. V., Rowell, D. P., ... & Kaplan, A. (2003). Global analyses of sea surface temperature, sea ice, and night marine air temperature since the late nineteenth century. Journal of Geophysical Research: Atmospheres, 108(D14), 4407.

Renfrew, I. A., Moore, G. K., Guest, P. S., & Bumke, K. (2002). A comparison of surface layer and surface turbulent flux observations over the Labrador Sea with ECMWF analyses and NCEP reanalyses. Journal of Physical Oceanography,

32(2), 383-400.

Richter, J. H., Matthes, K., Calvo, N., & Gray, L. J. (2011). Influence of the quasi-biennial oscillation and El Niño-Southern Oscillation on the frequency of sudden stratospheric warmings. Journal of Geophysical Research: Atmospheres, 116(D20).

Rinke, A., Dethloff, K., Dorn, W., Handorf, D., & Moore, J. C. (2013). Simulated Arctic atmospheric feedbacks associated with late summer sea ice anomalies. Journal of Geophysical Research: Atmospheres, 118(14), 7698-7714.

Romanowsky, E., Handorf, D., Jaiser, R., Wohltmann, I., Dorn, W., Ukita, J., ... & Rex, M. (2019). The role of stratospheric ozone for Arctic-midlatitude linkages. Scientific Reports, 9(1), 7962.

Sassi, F., Garcia, R. R., Marsh, D., & Hoppel, K. W. (2010). The role of the middle atmosphere in simulations of the troposphere during Northern Hemisphere winter: Differences between high-and low-top models. Journal of the Atmospheric Sciences, 67(9), 3048-3064.

Schlesinger, M. E., & Ramankutty, N. (1994). An oscillation in the global climate system of period 65–70 years. Nature, 367(6465), 723.

Schoeberl, M. R. (1978). Stratospheric warmings: Observations and theory. Reviews of Geophysics, 16(4), 521-538.

Screen, J. A. (2017a). The missing Northern European winter cooling response to Arctic sea ice loss. Nature Communications, 8, 14603.

Screen, J. A. (2017b). Simulated atmospheric response to regional and pan-Arctic sea ice loss. Journal of Climate, 30(11), 3945-3962.

Screen, J. A., Deser, C., Smith, D. M., Zhang, X., Blackport, R., Kushner, P. J., ... & Sun, L. (2018). Consistency and discrepancy in the atmospheric response to Arctic sea-ice loss across climate models. Nature Geoscience, 11(3), 155.

Screen, J. A., Deser, C., Simmonds, I., & Tomas, R. (2014). Atmospheric impacts of Arctic sea-ice loss, 1979–2009: Separating forced change from atmospheric internal variability. Climate Dynamics, 43(1-2), 333-344.

Screen, J. A., & Simmonds, I. (2010). The central role of diminishing sea ice in recent Arctic temperature amplification. Nature, 464(7293), 1334.

Screen, J. A., Simmonds, I., Deser, C., & Tomas, R. (2013). The atmospheric response to three decades of observed Arctic sea ice loss. Journal of Climate, 26(4), 1230-1248.

Seierstad, I. A., & Bader, J. (2009). Impact of a projected future Arctic sea ice reduction on extratropical storminess and the NAO. Climate Dynamics, 33(7-8), 937.

Shaw, T. A., & Perlwitz, J. (2010). The impact of stratospheric model configuration on planetary-scale waves in Northern Hemisphere winter. Journal of Climate, 23(12), 3369-3389.

Shindell, D., & Faluvegi, G. (2009). Climate response to regional radiative forcing during the twentieth century. Nature Geoscience, 2(4), 294.

Sigmond, M., Scinocca, J. F., Kharin, V. V., & Shepherd, T. G. (2013). Enhanced seasonal forecast skill following stratospheric sudden warmings. Nature Geoscience, 6(2), 98.

Singarayer, J. S., Bamber, J. L., & Valdes, P. J. (2006). Twenty-first-century climate impacts from a declining Arctic sea ice cover. Journal of Climate, 19(7), 1109-1125.

Smith, D. M., Dunstone, N. J., Scaife, A. A., Fiedler, E. K., Copsey, D., & Hardiman, S. C. (2017). Atmospheric response to Arctic and Antarctic sea ice: The importance of ocean–atmosphere coupling and the background state. Journal of Climate, 30(12), 4547-4565.

Smith, K. L., & Kushner, P. J. (2012). Linear interference and the initiation of extratropical stratosphere-troposphere interactions. Journal of Geophysical Research: Atmospheres, 117(D13), D13107.

Song, K., & Son, S. W. (2018). Revisiting the ENSO–SSW relationship. Journal of Climate, 31(6), 2133-2143.

Strey, S. T., Chapman, W. L., & Walsh, J. E. (2010). The 2007 sea ice minimum: Impacts on the Northern Hemisphere atmosphere in late autumn and early winter. Journal of Geophysical Research: Atmospheres, 115(D23), D23103.

Sun, L., Deser, C., Polvani, L., & Tomas, R. (2014). Influence of projected Arctic sea ice loss on polar stratospheric ozone and circulation in spring. Environmental Research Letters, 9(8), 084016.

Sun, L., Deser, C., & Tomas, R. A. (2015). Mechanisms of stratospheric and tropospheric circulation response to projected Arctic sea ice loss. Journal of Climate, 28(19), 7824–7845.

Sun, L., Perlwitz, J., & Hoerling, M. (2016). What caused the recent “Warm Arctic, Cold Continents” trend pattern in winter temperatures?. Geophysical Research Letters, 43(10), 5345-5352.

Taguchi, M. (2015). Changes in frequency of major stratospheric sudden warmings with El Niño/Southern Oscillation and Quasi-Biennial Oscillation. Journal of the Meteorological Society of Japan. Ser. II, 93(1), 99-115.

Taguchi, M., & Hartmann, D. L. (2006). Increased occurrence of stratospheric sudden warmings during El Niño as simulated by WACCM. Journal of Climate, 19(3), 324–332.

Takaya, K., & Nakamura, H. (1997). A formulation of a wave-activity flux for stationary Rossby waves on a zonally varying basic flow. Geophysical Research Letters, 24(23), 2985-2988.

Takaya, K., & Nakamura, H. (2001). A formulation of a phase-independent wave-activity flux for stationary and migratory quasigeostrophic eddies on a zonally varying basic flow. Journal of the Atmospheric Sciences, 58(6), 608-627.

Taylor, K. E., Stouffer, R. J., & Meehl, G. A. (2012). An overview of CMIP5 and the experiment design. Bulletin of the American Meteorological Society, 93(4), 485-498.

Thompson, D. W., Baldwin, M. P., & Wallace, J. M. (2002). Stratospheric connection to Northern Hemisphere wintertime weather: Implications for prediction. Journal of

Climate, 15(12), 1421-1428.

Thompson, D. W., & Wallace, J. M. (1998). The Arctic Oscillation signature in the wintertime geopotential height and temperature fields. Geophysical Research Letters, 25(9), 1297-1300.

Thompson, D. W., & Wallace, J. M. (2000). Annular modes in the extratropical circulation. Part I: Month-to-month variability. Journal of Climate, 13(5), 1000-1016.

Titchner, H. A., & Rayner, N. A. (2014). The Met Office Hadley Centre sea ice and sea surface temperature data set, version 2: 1. Sea ice concentrations. Journal of Geophysical Research. Atmospheres, 119(6), 2864–2889.

Trenberth, K. E. (1986). An assessment of the impact of transient eddies on the zonal flow during a blocking episode using localized Eliassen-Palm flux diagnostics. Journal of the Atmospheric Sciences, 43(19), 2070-2087.

Tripathi, O. P., Charlton-Perez, A., Sigmond, M., & Vitart, F. (2015). Enhanced long-range forecast skill in boreal winter following stratospheric strong vortex conditions. Environmental Research Letters, 10, 104007.

van Loon, H., & Rogers, J. C. (1978). The seesaw in winter temperatures between

Greenland and northern Europe. Part I: General description. Monthly Weather Review, 106(3), 296-310.

Vavrus, S. J. (2018). The influence of Arctic amplification on mid-latitude weather and climate. Current Climate Change Reports, 4(3), 238-249.

Vihma, T. (2014). Effects of Arctic sea ice decline on weather and climate: A review. Surveys in Geophysics, 35(5), 1175-1214.

Walker, S. G. T., & Bliss, E. W. (1928). World weather, III. Edward Stanford.

Wallace, J. M., & Gutzler, D. S. (1981). Teleconnections in the geopotential height field during the Northern Hemisphere winter. Monthly Weather Review, 109(4), 784-812.

Walsh, J. E. (2014). Intensified warming of the Arctic: Causes and impacts on middle latitudes. Global and Planetary Change, 117, 52-63.

Wei, K., Chen, W., & Huang, R. (2007). Association of tropical Pacific sea surface temperatures with the stratospheric Holton-Tan Oscillation in the Northern Hemisphere winter. Geophysical Research Letters, 34(16), L16814.

Woollings, T., Charlton-Perez, A., Ineson, S., Marshall, A. G., & Masato, G. (2010).

Associations between stratospheric variability and tropospheric blocking. Journal of Geophysical Research: Atmospheres, 115(D6), D06108.

Wu, Y., & Smith, K. L. (2016). Response of Northern Hemisphere midlatitude circulation to Arctic amplification in a simple atmospheric general circulation model. Journal of Climate, 29(6), 2041-2058.

Yamashita, Y., Akiyoshi, H., & Takahashi, M. (2011). Dynamical response in the Northern Hemisphere midlatitude and high-latitude winter to the QBO simulated by CCSR/NIES CCM. Journal of Geophysical Research: Atmospheres, 116(D6), D06118.

Yang, X. Y., Yuan, X., & Ting, M. (2016). Dynamical link between the Barents–Kara Sea ice and the Arctic oscillation. Journal of Climate, 29(14), 5103-5122.

Zhang, P., Wu, Y., & Smith, K. L. (2018a). Prolonged effect of the stratospheric pathway in linking Barents–Kara Sea sea ice variability to the midlatitude circulation in a simplified model. Climate Dynamics, 50(1-2), 527-539.

Zhang, P., Wu, Y., Simpson, I. R., Smith, K. L., Zhang, X., De, B., & Callaghan, P. (2018b). A stratospheric pathway linking a colder Siberia to Barents-Kara Sea sea ice loss. Science Advances, 4(7), eaat6025.

Zhang, X., He, J., Zhang, J., Polyakov, I., Gerdes, R., Inoue, J., & Wu, P. (2013). Enhanced poleward moisture transport and amplified northern high-latitude wetting trend. Nature Climate Change, 3(1), 47.